Examining the Bombardment Record of the Saturnian Satellites

Through Impact Crater Analysis

by

Sierra Nichole Ferguson

A Dissertation Presented in Partial Fulfillment
of the Requirements for the Degree
Doctor of Philosophy

Approved June 2021 by the
Graduate Supervisory Committee:

Alyssa Rhoden, Co-Chair
Steven Desch, Co-Chair
Maitrayee Bose
Mark Robinson
David Williams

ARIZONA STATE UNIVERSITY

August 2021

ABSTRACT

The central question of my dissertation is "How old are the inner moons of Saturn?" This question is of critical importance for the refinement of how solar systems and giant planet systems form and evolve. One of the most direct ways to test the ages of a planet's surface is through the use of impact craters. Here I utilize images from the Cassini Imaging Science Subsystem (ISS) to count the craters on the mid-sized moons of Saturn, Tethys and Dione. I present a statistical analysis of the craters and the likely impactor sources that crated these craters. On Tethys I find that the impact craters can be explained by a planetocentric source that is local to the Saturnian system and is not found elsewhere in the outer planets. I also find that the majority of mapped regions are likely close in age. On Dione, I have mapped four areas at a regional-scale resolution (~ 200 m/ pix) and have found that resurfacing has greatly affected the small crater population and that the overall size-frequency distribution of craters is most representative of a planetocentric source unique to Saturn. Elliptical craters provide another means of assessing the bombardment environment around Saturn, as they record the primary direction of the object that created the crater upon impact on the surface. I have mapped these craters on Tethys and Dione, to analyze the global distributions of these craters and their orientations. Across both satellites, I find that in the equatorial regions between 30° N and 30°S in latitude, the orientations of the elliptical craters are consistent with an East/West orientation for their direction, which also is suggestive of a local planetocentric source. Throughout the main three studies presented in this dissertation I

find that the main impactor source is a planetocentric source that is unique to Saturn and is not seen on the moons of the other giant planets.

DEDICATION

To all the young girls out there who've been told you aren't smart enough to like science or that you'll never be able to learn math,

I was once in that same position and now I'm here. Finishing a degree at one point I had thought impossible. All it takes is a couple people to see your potential and help you see it. You are smart enough and you can learn and understand that tough math course.

-Ad Astra

--and

To my Mother,

Your love and support throughout this entire process has meant the world to me. Even when I didn't always believe in myself, you have always believed in me and worked to help me see what I could be. From a young age you've always supported me and sought to make sure I had help when I needed it. In the face of all the self-doubt I've had, you've been my rock. Always there to listen and offer advice. I love you so much.

ACKNOWLEDGMENTS

Obtaining a Ph.D. is something I once thought was outside the realm of possibility for me and now I find myself achieving this seemingly impossible goal. No dissertation can be completed alone and I wouldn't be here today without the large support system that I've cultivated over the last five years at ASU and around the country. As 2020 showed, this support system was crucial to completing this degree. First and foremost, I want to thank my graduate advisors Alyssa Rhoden and Steve Desch. Alyssa, there are so many things I can say about how your mentorship and advising has made me a better scientist, your continual words of encouragement and support have meant the world to me and I thank you for helping me see how great a scientist I actually am. Steve, you brought me into your research group with such open arms and an eagerness to learn more about what I was working on. You've helped me understand how to best communicate my science and how to critically question all the papers I read. Together, you've both helped me become the scientist I am today.

To my committee members Mark Robinson, David Williams, and Maitrayee Bose, thank you for being there and letting me bounce ideas off you, for having confidence in my abilities as a scientist, and providing your unique insights on my projects.

I also want to acknowledge all of the phenomenal women in planetary science who have taken me under their wings and taught me so much of what I know today: Lynnae Quick, Lori Glaze, Louise Prockter, Emily Martin, Michelle Kirchoff, Angela Stickle, Ingrid Dauber, and Julie Rathbun. To Nadine Barlow who started me on this path of being a planetary scientist. I learned so much from you, not just in classes, but in the

research I did as well. I miss you and I hope I'm making you proud. Margaret Landis, Adeene Denton, Sondy Springmann, Maria Steinrueck; You've all been incredible rocks throughout this last year and I know without a doubt, your friendship helped me make it through 2020. From chatting about craters, postdoc apps/proposals, and cats, your support and encouragement mean the world to me. I know you'll all continue to do amazing things in your careers.

To my ASU found family in Lena Heffern, Alex Pye, Zee Wilson, Ashley Herbst, Kyle Mohr, Vishaal Singh, Lucia Perez, Jessica Noviello, Zack Torrano, Soumya Ray, Chuhong Mai, and Genevive Studer-Ellis (and many others!); Your friendship has enriched so much of my graduate experience and I can't wait to see where our journeys take us next. To the SESE administrative staff: Becca Dial and Juana Garcia for helping me navigate the ASU administration. Your support has been so critical and appreciated!

I want to thank my family and friends for all of their support during my academic career so far. To my forever roommate and older sister I never had: Alyssa Sherry. Your friendship and sisterhood has been incredible over the last 5 years. There's no one else I'd rather have spent 2020 stuck in an apartment with. From our Star Wars to Marvel marathons and all the trips out to California, thanks for helping me stay calm and navigate the waters of grad school. To my writing group, thank you for your incredible friendship, love of pineapples, and always encouraging me when I struggled to write.

I'd like to acknowledge financial support I received for this degree from: NASA Cassini Data Analysis Program (CDAP) award NNX16AI42G to Alyssa Rhoden, and NASA Future Investigators in Earth and Space Science and Technology (FINESST) award 80NSSC19K1532 to Sierra Ferguson and Steve Desch.

TABLE OF CONTENTS

Page

CHAPTER Page

CHAPTER Page

LIST OF TABLES

LIST OF FIGURES

Figure Page

CHAPTER 1

INTRODUCTION

1.1 Overview of the Saturn System

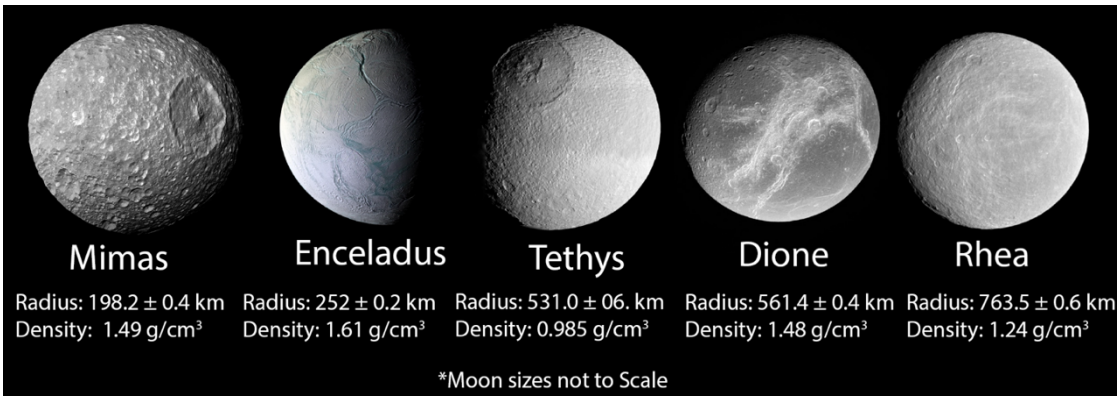

Figure 1.1: Overview of the mid-sized icy moons of Saturn (MIM's) and their physical characteristics. Moons are not scaled to one another. Image Credit: NASA/JPL/SSI

The Saturnian system is host to a highly diverse population of rings and moons, with wide ranges of surface activity, no clear gradient in composition and size between the satellites, co-orbital satellites around some moons, and a large ring system with moonlets embedded within. A comparison of Saturn and Jupiter (Peale et al., 1999; Castillo-Rogez et al., 2018) reveals two vastly different systems. Jupiter's moons follow a clear compositional gradient with silicate fractions decreasing with distance from Jupiter, where the sizes of the moons increase with distance, a small ring system is present, and the larger inner moons Io and Europa are active. This contrasts with the Saturn system, where Enceladus is the only presently active satellite of the mid-sized inner moons despite being smaller than both Io and Europa. NASA's *Cassini-Huygens* mission performed long-term reconnaissance of the system and observed the plumes of Enceladus (Spencer et al., 2006), methane lakes on Titan, seasonal storms in Saturn's atmosphere, and examined the complex geology of the mid-sized icy moons (MIMs)

Mimas, Enceladus, Tethys, Dione, and Rhea (Figure 1.1). With the data collected by the *Cassini* mission, more questions were posed about the evolution of the system as a whole than the mission could answer during the extended mission phases.

One of these questions is "How old are the mid-sized moons of Saturn?" This question was re-posed by Ćuk et al., 2016 where they argued for a lower limit on the moons' ages of ~100 Myr. Saturn's rings and satellites are closely coupled to one another, such that determining the age and formation/evolution scenario for one would greatly assist in solving how the other formed. *Cassini's* Grand Finale orbits flew the spacecraft between the rings and the planet, allowing a more precise measurement of the mass of the rings, finding a value of $1.54 \pm 0.49 \times 10^{19}$ kg (Iess et al., 2019). Iess et al., 2019 examined the mass and brightness of the rings and concluded that the seemingly pristine nature of the ice in the rings demands an age of ~100 Myr. Rebuttals to this work then argued that this young age for the rings was not fully correct, as there are other ways that the rings could appear young. In addition, questions were raised about how to form an extensive ring system in such a recent epoch of Solar System history (Crida et al., 2019). Debate is still ongoing within the literature as to the actual age of the ring system, so the estimates place it anywhere between 4.5 Gyr (age of the Solar System) and 100 Myr. Further examination of the inner satellites in the system should provide more constraints on how the ring system evolved.

Enceladus is well known for the plumes emanating from its south polar terrain (Spencer et al., 2008), but it also has an unusual distribution of older tectonized terrains as well as heavily cratered regions (Crow-Willard and Pappalardo, 2015). Although the highest heat flows are correlated with the active plume region (Spencer et al, 2006), even

craters well outside the SPT are highly relaxed, indicating past high heat flows (Bland et al., 2012). In contrast, its neighbor Mimas is dominated by craters, including the large Herschel impact basin (D = 139 km), has very few tectonic features (Schenk et al., 2018) and is not currently active and may not have ever been. Current research has focused on examining why Enceladus is active while Mimas is not, and if Mimas could ever have sustained a subsurface ocean (Rhoden et al., 2017).

Dione and Tethys are similar in size (560 km vs. 530 km radius) but have wildly different surface features and crater densities. Tethys is primarily dominated by impact cratering, particularly the Odysseus impact basin (D ≈ 400 km) whereas its surface is minimally tectonized with the exception of the large canyon system named Ithaca Chasma (Geise et al., 2007). Dione represents a surface that has been heavily modified by tectonics throughout the wispy terrain on the trailing hemisphere and across other ancient portions of the surface, while still being heavily impacted by cratering processes. Dione is also thought to have had an ocean at some point in its history and may represent another member of the "ocean worlds" family (Beuthe et al., 2016), but is not currently active like its neighbor Enceladus. Dione and Tethys also both have co-orbital satellites (Telesto and Calypso for Tethys, and Helene and Polydeuces for Dione) orbiting in the L4 and L5 Lagrange points of their orbits, whereas none of the other satellites in the system have these trojan moons. Rhea, is the furthest mid-sized moon from Saturn, and has a surface that has been modified extensively by impact craters and has less tectonic modification than either Tethys or Dione.

Dynamically complex orbital resonances and unusual variability in compositions between moons have led people to question just how and when these inner moons could

have formed. Ćuk et al., 2016 simulated a wide range of orbital parameters to model the dynamical evolution of the satellites. From their models, they predicted that some of these moons could be as young as 100 Myr. Based on the examination of possible resonances between the moons, the team found that Tethys and Dione had not previously passed through their predicted 3:2 mean motion resonance crossing, which would otherwise excite the inclinations of the two moons (Ćuk et al., 2016). While this isn't observed in the current system configuration, the authors suggest that either the tidal evolution of Tethys and Dione has been slow or that the mid-sized moons of Saturn are significantly younger than the Solar System (Ćuk et al., 2016). While the 3:2 resonance between Tethys and Dione likely hasn't happened, the 5:3 resonance crossing between Dione and Rhea likely occurred and — in combination with a different Tethys/Dione resonance—explains the current inclinations of Tethys and Rhea.

1.2 Formation Mechanisms of the Mid-Sized Moons

Currently, many researchers are working to explain how this satellite system formed and evolved, but there has yet to be a comprehensive and conclusive hypothesis for their formation. Several formation scenarios have been proposed for the mid-sized satellites: 1) formation in the Saturnian sub-nebula (Canup & Ward 2006, Sasaki et al., 2010, Peale & Canup 2015), 2) formation from Saturn's rings (Canup 2010, Charnoz et al., 2011, Crida & Charnoz 2012), and 3) formation from re-accretion of the debris generated by a giant impact onto a large proto-moon (Asphaug & Reufer 2013). If the moons formed out of the Saturnian sub-nebula, gas and entrained particles would have combined together and started accreting into planetesimals and eventually one of the mid-

sized moons (Canup & Ward 2006, Castillo-Rogez et al., 2018). According to this model, the moons should show a gradient in the densities of the satellites, which is in contrast to the widely varying densities of the satellite system (Castillo-Rogez et al., 2018).

In the second scenario, material needed for a moon to form from the rings would likely result from either an impact or a large object entering the Roche limit of Saturn and being disrupted (Cameron & Ward 1976, Canup 2010). One possibility for the source of the material that made the moons in this scenario is a Titan-sized, differentiated object which then broke up (Canup 2010,. Charnoz et al., 2011). Over time, the icy leftover material from this protosatellite would spread out through the system and accrete into the moons we know today and the silicate material falls onto Saturn itself (Canup 2010). In the model of Charnoz et al., 2011, they solve the silicate problem by having leftover silicate fragments gradually accrete ice around them in a larger initial ring. These proto-satellites, once massive enough would then migrate out of the rings and into their current orbital locations (Charnoz et al., 2011). Inherent in both of these models are difficulties in reproducing the exact composition differences and a remaining question about the ability of moons formed outside the Roche radius to migrate out fast enough to reproduce the correct satellite spacing (Peale & Canup 2015). An additional model combines the ring formation with formation from the Saturn sub-nebula. In this model, Mimas, Enceladus, and Tethys all form from the rings, whereas Dione and Rhea form out of the sub-nebula (Salmon & Canup 2017).

One issue present within all of these models is replicating the observed rock component compared to the ice. If the moons form from the rings, which show little signs of non-ice material, the moons that formed from that ring would need an additional

source for their rocky interiors (Castillo-Rogez et al., 2018). One solution proposed (Salmon & Canup 2017) is that the rocky component could have been supplied by impacts that occurred during the late heavy bombardment; but that doesn't explain the rock-to-ice ratios of Dione and Rhea, which they advocate formed out of the sub-nebula. Accretion of all mid-sized satellites from the sub-nebula would also likely require an additional rocky source to explain the rock-to-ice ratios. Asphaug & Reufer 2013 suggest that the mid-sized moons form from the debris of a giant impact between two larger objects that merged to form Titan. This model has the issue of not tracking how the system would further evolve from that point and what it means for the heat budgets of the resulting satellites (Castillo-Rogez et al., 2018).

One additional approach to modeling the formation of the mid-sized satellites comes from modeling both the thermal and orbital evolution of the satellites together in one model (Neveu & Rhoden 2019). This approach allows for a variation in the tidal dissipation factor/quality factor (Q) within Saturn, which has been suggested by Lainey et al,. 2017 to vary for moons across the system. Here Q represents how the moons respond to the tides exerted on them by Saturn during their orbits. Assuming the moons formed from the rings, models simultaneously evolving the interior and orbital parameters of the satellites show that Rhea should be a primordial satellite (age ~4.5 Gyr), Mimas should be relatively young (~0.1-1 Gyr), and the remaining moons are more likely to be older; all have or had an ocean at one point in their history (Neveu & Rhoden 2019). A challenge with all of these models is finding observational data with which to verify or refute the models. Independent estimates of surface age, heat flow, and other characteristics that would arise from particular thermal-orbital histories are of high value

in identifying the right model or conditions that gave rise to the Saturnian satellite system.

1.3 Impact Craters and their Role in Surface Age Analysis

One approach to dating a planetary surface is through impact crater analysis. Impact cratering is a fundamental planetary process that dominates most landscapes in the Solar System. Numerous studies have been carried out on the craters of the Moon and Mars that have used stratigraphic relationships, radiometrically dating of returned samples, and comparisons to known impactor source populations, to determine model ages for various terrain units. When looking at surfaces of the outer planet satellites, although we can still utilize crater counts and the stratigraphic relationships in the surface geology, the lack of returned samples precludes our ability to determine absolute ages. Applying the inner solar system impactor chronologies to the outer planet cratering record yields large uncertainties and does not properly represent the true population of impactors that have hit both types of bodies. Of note, impact crater analysis also can include information about the interior morphologies when present (i.e., floor modification, or presence of a central peak/pit); however, it is unclear how these morphologies may be affected by an ocean underneath a pre-existing ice shell.

Additionally, polygonal crater morphologies can help us to discern how fractured the subsurface can be. Polygonal craters are those that are formed from when an impactor hits a target that has pre-existing fractures in its subsurface (Shoemaker et al., 1963, Ohman et al., 2010, Beddingfield et al., 2016), yielding a crater rim comprised of several straight rim segments rather than the typically circular rim (Figure 1.2, Meteor Crater).

Polygonal craters have been located across the inner planets (Ohman et al., 2010) Ceres, and the Saturnian satellites (Beddingfield et al., 2016) to name a few.

Each of these worlds has surfaces that have been modified due to tectonic processes, which directly influences the formation of the polygonal crater. After the bolide collides with the surface, energy is released into the target, which drives the excavation stage of crater formation (Melosh 1989). With polygonal craters, that impact energy is still directed into the target, but utilizes pre-existing zones of weakness in the fractures to excavate the crater in the models described by (Öhman et al., 2006; 2008; 2009; 2010). These models predict that the fractures are parallel to the azimuths of the straight rim segments.

Figure 1.2: Meteor Crater, located between Flagstaff and Winslow in northern Arizona. Meteor Crater represents a terrestrial example of a polygonal impact crater. Meteor crater overlies pre-existing faults in the surrounding rock. Image credit: NASA Earth Observatory.

Elliptical craters (Fig. 1.3) are an additional unique morphology that can arise when a bolide impacts a target at a shallow impact angle (~15-30°) (Gault & Wedekind 1978, Bottke et al., 2000, Elbeshausen et al., 2013). Ellipticity and crater size are both influenced by the impact angle and the target material (Elbeshausen et al., 2013). Ellipticity is defined as

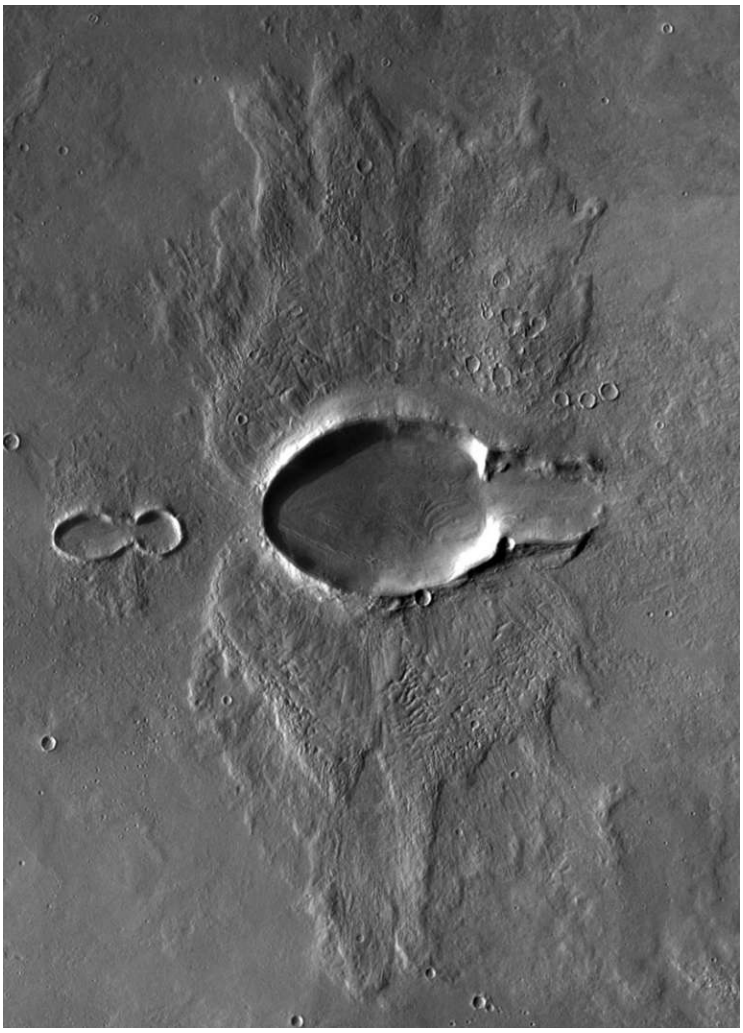

Figure 1.3 Example elliptical crater on Mars. Image Credit: NASA/JPL/UA – Emily Lakdawalla

the ratio of the major axis divided by the minor axis (i.e., Bottke et al., 2000). Craters appear more elliptical when they are formed from shallower impact angles (Elbeshausen et al., 2013). Further modeling from Elbeshausen et al., 2013 showed that elliptical craters are formed by "shock-induced excavation" which is analogous to the formation process for circular craters. As the impact angle decreases, the transition to elliptical from circular craters is very dependent on the momentum of the impact (Elbeshausen et al., 2013). Increasingly oblique impacts have elongated non-symmetric shock fronts, which suggests the energy transfer occurs along the projectiles' path (Elbeshausen et al., 2013). Energy is then deposited at different depths in the forming crater and is transferred at varying efficiencies (Elbeshausen et al., 2013). The critical angle which is represented as the largest angle an elliptical crater can form at (Collins et al., 2011 & Elbeshausen et al., 2013) is heavily dependent on the cratering efficiency

(ratio of crater diameter to impactor diameter, Holsapple et al., 1993). In contrast to circular crater formation, where the impact angles are head-on (~ 45°- 90°, Melosh 1989). This difference in impact angle is the dominant factor in determining the final crater shape as this affects the energy transfer in the target. A head on collision would transfer the energy symmetrically around the bollide, whereas the oblique impact pushes the energy out in an asymmetric fashion affecting the compression and excavation of the surface material (Elbeshausen et al., 2013).

1.4 Impact Cratering in the Inner Solar System

In order to utilize the observed impact craters for age-dating a surface, an understanding of the impactor populations is necessary. Examinations of impact craters on the Moon and Mars have provided glimpses into dominant impact sources and age relations within the Inner Solar System. Utilizing the radiometric age dates of Luna and Apollo samples, combined with the crater counts of areas on the Moon, Neukum et al., 2001 were able to derive a Lunar Chronology curve that combined knowledge of the source impactors as well as the ages of these returned samples. Within this chronology, there are still no calibrated dates available between 1 Gyr and 3 Gyr ago (Stöffler and Ryder, 2001; Hiesinger et al., 2012). It's assumed that the cratering rate remained constant over this time frame, which may reflect nature, but limited data points preclude a definitive conclusion (Hiesinger et al., 2012). The chronology and production function generated for the Moon have also been applied to Mars (Ivanov 2001) where they have been used to obtain absolute ages for geologic units of interest. On Mars, recent work has been done do compute the current impact rate on the planet. Dauber et al., 2013 determined that the current impact rate on Mars is much lower for meter-sized craters

than the kilometer-sized craters. The impact rate at the meter scale on Mars is also a lower rate (Dauber et al., 2013) when compared to the other dominant production functions used for the inner solar system chronologies (Neukum et al., 2001 and Hartman, 2005). Across these two planetary bodies, a combination of Main-Belt Asteroids and near-Earth objects are responsible for the majority of craters on the surface (Neukum et al., 2001; Strom et al., 2005; Hartman 2005)

Researchers have utilized data from the Dawn mission at Ceres (Russell et al., 2016) to examine the impact crater populations on the surface to derive information about the dynamical environment around Ceres (Hiesinger et al., 2016; Marchi et al., 2016; Landis et al., 2019). These impact crater size-frequency distributions were then compared to production functions derived from the current Main Belt Asteroid population and one derived from Lunar impact craters and returned samples from the Apollo and Luna Missions (Hiesinger et al., 2016). While both production models have strengths and weaknesses, the Asteroid model is more favored as the main source for craters at Ceres due to Ceres' location in the main belt and the impact crater distribution on the surface. Additional studies (i.e., Strom et al., 2018 & Landis et al., 2019) also argue in favor for the usage of the asteroid derived model for use in examining the expected crater populations on Ceres. The asteroid belt production function also works best for Ceres, as it does not require more pure water ice in the subsurface than what is currently predicted for Ceres (Landis et al., 2019). Additionally, Ceres lacks a population of large (D > 280 km) impact basins based on the production functions and could have migrated inwards to the asteroid from the outer solar system; but Marchi et al., 2016 conclude that this is unlikely and that this lack of large craters on Ceres is due to other endogenic processes

occurring within the interior of Ceres. For Ceres' location in the Main Belt and other belt asteroids, this asteroid derived model makes the most sense to use to examine the cratering records as it best records the collisional evolution in that area of the Solar System. Due to its specificity to the Main Belt impactor sources, it is not applicable to the surfaces of the Saturnian satellites.

1.5 Impact Cratering in the Outer Solar System and Attempts at Age Dating

Within the outer planets, moons were predominantly impacted by either heliocentric (sun-orbiting) or planetocentric (planet-orbiting) debris. Zahnle et al., 2003 described two production functions for the impactor sources responsible for the bombardment of these satellites, termed Case A and Case B. Case A includes heliocentric sources as recorded by population of Jupiter family comets (JFC's), the observed craters on Europa, and observed cometary impacts onto Jupiter like the Shoemaker-Levy 9 impact. Case B is derived from the crater population on Triton. Impact craters on Pluto and Charon appear to match more closely the Case A scenario, at least for diameters < 10 km (Singer et al., 2019). Neither Case A nor Case B explicitly include a planetocentric source population of impactors and are both built off heliocentric impactor fluxes

Inside the Saturn system, there is no single dominant impactor population observed in the cratering record (Kirchoff & Schenk, 2010, 2015; Ferguson et al., 2020), suggesting that the bombardment environment is highly complex, with a mix of impactor sources ranging from varying amounts of planetocentric and heliocentric debris as responsible for the cratering of these inner satellites. The Case A and Case B models are just two possible scenarios of the bombardment environments of the giant planets and are

not fully representative of the bombardment history of the Outer Solar System. They are both heliocentric in origin, which should be observable in the crater record: one way to quantify the extent of a heliocentric impactor source in the cratering record is to identify an asymmetry in the cratering such that the leading hemisphere has a higher crater density than the trailing hemisphere (Shoemaker & Wolfe 1981; Horedt & Neukum 1984A, B; Zahnle et al., 1998, 2001; Hirata 2016). Examinations of the cratering records on the Saturnian moons have not found this asymmetry to be present in the system, which implies that the dominant source of debris creating the craters is planetocentric in origin, rather than heliocentric. Out of the two main production functions, neither Case A nor Case B explicitly include a planetocentric source population of impactors and are both built off heliocentric impactor fluxes (Zahnle et al., 2003). Rather, deviations between observed crater populations and the production functions are often attributed to planetocentric material. Until the timing and impact characteristics of planetocentric material can be constrained, it will be almost impossible to determine robust surface ages for the Saturnian moons.

Alternative constraints on the sources of impactors come from spectroscopy of craters. Recent studies have utilized the *Cassini* Visual and Infrared Mapping Spectrometer (VIMS) and Imaging Science Subsystem (ISS) data to examine the ratios between crystalline and amorphous ice in and around impact craters on Rhea and Dione as a proxy for their surface age (Dalle Ore et al., 2015; López-Oquendo et al., 2019; Rivera-Valentiń et al., 2020). During the impact crater formation process, the immediate aftermath of the crater would leave behind a melt pocket which would re-solidify to crystalline ice (Dalle Ore et al., 2015). Over time the crater is then exposed to ion

bombardment from particles within the system which changes the ice from a crystalline phase to an amorphous phase (Dalle Ore et al., 2015). In particular they have examined the 1.65 μm and 2 μm water ice bands to compute the ratios of crystalline to amorphous ice (Dalle Ore et al., 2015; López-Oquendo et al., 2019; Rivera-Valentiń et al., 2020). For a synchronously rotating moon in the Saturn system, this method works the best on the trailing hemisphere, as that is the hemisphere that is more frequently being bombarded by the charged particles in the system (Dalle Ore et al., 2015; Rivera-Valentiń et al., 2020). Examination of two craters on Rhea (Inktomi and Obatala) found that Inktomi on the leading hemisphere appears to be more sheltered from the particle collisions, as it has a more pristine distribution of crystalline and amorphous water ice. (Dalle Ore et al., 2015). In contrast, Obatala (located on the trailing hemisphere) was dated to have an exposure age of ~ 450 +110/-130 Myr. Further exposure age dating on Dione (López-Oquendo et al., 2019; Rivera-Valentiń et al., 2020) has also yielded older ages (~ 2- 1.4 Gyr) for some of their dated terrains, further lending credence to an older age of the satellites. Additionally, best-fit derived cratering rates by (Rivera-Valentiń et al., 2020) would actually yield a higher cratering rate than what is fitted by the Zahnle et al., 2003 Case B scenario, but Case B does fit their data within error.

1.6 Dissertation Overview

Throughout this dissertation, I examine the impact crater distributions and their morphologies as a means to further characterize the impactor sources responsible for the craters on Tethys and Dione. Robust characterizations of the myriad potential impactor sources is critical to refining the surface age estimates of the inner Saturnian moons. With a more complete categorization of the impactor size-frequency distributions at play in the

system, the errors associated with the age estimates can be narrowed down and more progress can be made on determining the timeline for how these moons formed and evolved. In particular, I ask the following questions: 1) Which mechanism for formation of the moons is consistent with their cratering record? 2) How old are the mid-sized moons of Saturn? and 3) How much has the cratering record been shaped by different processes? These questions are too broad in scope, demanding multiple interdisciplinary investigations, to fully answer even in the course of a dissertation; but this dissertation demonstrates significant progress toward answering them.

Ascertaining the ages of these moons is central to answering several key questions posed by the Planetary Science Decadal Survey (National Research Council Committee on the Planetary Science Decadal Survey 2011, NRC 2011) where they asked: 1) How did the giant planets and their satellite systems accrete, and is there evidence that they migrated to new orbital positions? 2) How have the myriad chemical and physical processes that shaped the solar system operated, interacted, and evolved over time? 3) What is the diversity of geologic activity (of the outer planet satellites) and how has it changed over time? Saturn and its moons represent an ideal location to answer these questions, due to the diversity of properties across the planet and the satellites.

As planetary scientists, we often play the role of historian by piecing together what happened in our Solar System billions of years ago, all the way up to the recent past. Within this dissertation, I examine the bombardment histories of Tethys and Dione to examine how the impactor sources have changed, how old the moons could be, and how they formed. Chapters 2 and 3 focus on the regional-scale mapping of impact craters on Tethys and Dione, provide comparisons between their distributions and the

predicted production functions, and examine the local geology. In chapter 4, I present global-scale surveys of elliptical craters, use their orientations to inform our assumptions of the impactor flux at Tethys and Dione, and examine what the elliptical craters can reveal about the ages of the satellites. Chapter 5 presents an examination of these results in a broader context of determining the ages of the system and where these results fit with the rest of the outer planets.

CHAPTER 2

SMALL IMPACT CRATER POPULATIONS ON SATURN'S MOON TETHYS AND IMPLICATIONS FOR SOURCE IMPACTORS IN THE SYSTEM

This chapter is reproduced from the Journal of Geophysical Research: Planets, where it was published in August 2020, with permission from the following co-authors: A.R. Rhoden and M.R. Kirchoff

Abstract

Current estimates place the ages of the inner Saturnian satellites (Mimas, Enceladus, Tethys, Dione, and Rhea) between 4.5 Gyr and 100 Myr. These estimates are based on impact crater measurements and dynamical simulations, both of which have uncertainties. Models of satellite evolution are inherently simplified and rely on uncertain or unknown parameters, which are often difficult to verify, whereas the interpretations of crater densities depend on the source populations of impactors, which are not constrained well in the outer Solar System. We investigate the cratering history of Tethys, mapping the population of small impact craters, to determine the roles that planetocentric, heliocentric, or other impact debris play in its cratering record. To map the surface of Tethys, we chose five regions that were located in geographically distinct areas and had high-resolution (~150 m/pix) image coverage by the Cassini ISS camera. We studied all craters that had at least 7 pixels across but mapped down to 5 pixels for completeness in the crater counts. We observe an abundance of small craters (D < 3 km) in the oldest region; this does not appear to be due to secondary cratering effects from the Odysseus

impact basin. Fitting the production functions from Zahnle et al. (2003), we find that neither their Case A nor Case B scenarios align with the observed cratering record at Tethys. We conclude that in addition to the standard outer solar system impactor populations, there is a Saturn-centric impactor source that is cratering Tethys.

Plain Language Summary

A major outstanding question post-Cassini is the following: How old are the mid-sized moons of Saturn (Mimas, Enceladus, Tethys, Dione, and Rhea)? Recent models of their orbital evolution have suggested that they could be as young as 100 Myr. Characterizing the impactor flux and how it has changed with time may help constrain the histories of these moons. We have mapped small craters (diameter <10 km) on Tethys to examine the sources of objects that collide with the moon. We find that the older terrain unit has a surplus of small impact craters that is consistent with a source of Saturn-orbiting debris. Younger terrain units appear to be more consistent with sun-orbiting debris at small diameters. This scenario is compatible with both young and old moons but suggests an early source of planetocentric debris. Further study on other satellites in the system is needed to ascertain age relationships.

2.1 Introduction

2.1.1. Formation and Orbital Evolution of Saturn's Mid-sized Icy Moons

Data gathered by the Cassini spacecraft answered some questions we had prior to the mission and raised further questions about the nature of the inner moons, Mimas, Enceladus, Tethys, Dione, and Rhea. Each are distinctly different in their degree of geologic surface activity, bulk density, size, surface coloration, heating history, and

orbital eccentricities (Castillo-Rogez et al., 2018; Hendrix et al., 2018; Schenk et al., 2011; Spencer et al., 2006), leading to exciting new questions about the system.

Several of these questions revolve around how the moons formed and evolved, as well as their ages. Studies of the system have suggested that (1) the mid-sized icy moons (MIMs) formed from the Saturn subnebula as Saturn itself was accreting (Canup, 2010; Canup & Ward, 2006; Peale & Canup, 2015); (2) the moons formed directly from Saturn's ice rich rings (Canup, 2010; Charnoz et al., 2010, 2011; Crida & Charnoz, 2012); (3) a hybrid scenario of the nebula and ring origins in which Mimas, Enceladus, and Tethys form from the rings while Dione, Rhea, and Titan form from the Saturn subnebula (Salmon & Canup, 2017); or (4) a catastrophic disruption of a Titan sized body reaccreted into the moons we see today (Asphaug & Reufer, 2013). Unlike the major Galilean satellites, which follow a decrease in density due to a decreasing amount of silicates with distance from Jupiter (Peale, 1999), the Saturnian satellites follow no clear trend in bulk densities, challenging the standard formation model and adding additional constraints to formation and evolution scenarios (Castillo-Rogez et al., 2018).

Mean-motion resonances that are expected to occur between the satellites in this system (e.g., Tethys-Dione 3:2 and Dione-Rhea 5:3) further complicate the formation scenarios of the satellites. Simulations of the moons' orbital evolution (Ćuk et al., 2016) suggest that Dione and Rhea have passed through the 5:3 mean motion resonance but that Tethys and Dione have yet to encounter the 3:2 resonance because they would still be in that resonance if they had. These results suggested to Ćuk et al. (2016) that either the MIMs are young (~100 Myr) or that they experienced very slow tidal migration (Q_{Saturn} < 80,000). However, they then argue that high tidal heat flux at Enceladus cannot be

replicated if slow tidal migration occurred in the moon system. To form the moons recently, the disk from which they form is created through orbital instabilities and collisions between previous generations of moons (Ćuk et al., 2016). This formation scenario implies that the cratering records observed on the MIMs are dominated by planetocentric (Saturn-orbiting) debris rather than heliocentric (Sun-orbiting) debris. Hence, careful examination of the cratering records of the MIMs could provide useful constraints on their impactor populations, with implications for both their ages and the mechanism by which they formed.

One issue with the Ćuk et al. (2016) interpretation is the assumption of a constant Q (tidal dissipation factor) over the history of the system. Astrometric measurements have shown that Saturn's tidal Q has an average value of ~1,250 and is different for each satellite (Lainey et al., 2012, 2017), likely because Q is frequency dependent (Fuller et al., 2016). Simulations of the coupled thermal-orbital evolution of the MIMs, using a time-varying Q, can reproduce many of the orbital and interior characteristics of the moons (Neveu & Rhoden, 2019). Across all of these simulations, Mimas must be 1 Gyr or younger and Rhea must be primor- dial. Uncertainties in model parameters, as well as numerically necessary simplifications to the physical model, have led to a range of possible solutions in which the other moons could be young or old (Neveu & Rhoden, 2019).

2.1.2. Crater Counts and Their Interpretations

Crater counts, in combination with radiometric age dating of returned samples from the Moon, have tradi- tionally been used to ascertain the absolute ages of planetary surfaces in the inner solar system (e.g., Neukum et al., 2001). Robust age determinations

require an in-depth understanding of the source population of impactors and how that population likely changed over time. This level of certainty in impactor sources and flux has not been attained for the Saturnian system, due to the lack of samples and to the diversity of crater morphologies and sizes. Cratering in the inner solar system is primarily caused by the impact of asteroids onto the surface (Marchi et al., 2009; Neukum et al., 2001; Strom et al., 2005) whereas craters on the bodies in the outer solar system have a wider range of sources. Specifically, at Saturn, potential sources for these craters include heliocentric material, planetocentric material, or debris formed from impacts onto the co-orbital moons of Tethys and Dione (Dobrovolskis et al., 2010; Dones et al., 2009; Nayak & Asphaug, 2016; Smith et al., 1981, 1982; Zahnle et al., 2003).

One of the hallmark production functions for the outer solar system was described by Zahnle et al. (2003) where they defined a Case A and Case B scenario. This Case A scenario is derived from cometary records of impacts at Jupiter and impacts on Jupiter's moons, and Case B is derived from crater counts at Triton (Zahnle et al., 2003). However, these two endmembers are likely not fully representative of the bombardment history within the Saturn system. Singer et al. (2019) surveyed craters on Charon and found that the Case A scenario from Zahnle et al. (2003) does match the closest to the crater data at $D < 10$ km, which also matches the young cratered terrains on Europa and Ganymede (Greenstreet et al., 2015; Singer et al., 2019). To apply our knowledge of the heliocentric impactor population of the Kuiper Belt to the Saturn system (e.g., Centaurs), the scattering of material by giant planet migration and later interaction with resonances would need to be known (Di Sisto & Brunini, 2007; Tiscareno & Malhotra, 2003; Volk & Malhotra, 2008). Several extrapolations of the small Centaur distribution and impact rate

were attempted before New Horizons based on information from available crater distributions on outer solar system satellite surfaces and dynamical information (Di Sisto & Zanardi, 2013, 2016; Zahnle et al., 2003). These came up with very shallow slopes (such as Case A from Zahnle et al., 2003) from the data available at Jupiter to very steep slopes (such as Case B from Zahnle et al., 2003) from the data available on Triton, to values in-between based upon data from Saturn (Di Sisto & Zanardi, 2013, 2016). Of these predictions, Case A (Zahnle et al., 2003) appears to be the closest to the data available from New Horizons (Singer et al., 2019), and particularly there appears to be a lack of small craters on Pluto and Charon's surfaces when compared to predicted impact rates by Centaurs using steeper slopes (Di Sisto & Zanardi, 2013, 2016; Singer et al., 2019). However, it is unclear how relevant a production function derived for the Jovian or Neptunian systems is for the Saturnian system.

Results from the Voyager missions at Saturn suggested two populations of impactors in the system: Populations I and II (Chapman & McKinnon, 1986; Horedt & Neukum, 1984a; Plescia & Boyce, 1982, 1985; Shoemaker & Wolfe, 1981; Smith et al., 1981, 1982). Population I was characterized by a shallow slope in size-frequency distribution of the impact craters and an abundance of craters larger than 20 km. Population I is similar to the crater distributions observed on the Galilean satellites and is potentially observed on Rhea (Dones et al., 2009; Kirchoff et al., 2018; Kirchoff & Schenk, 2010). Population II has an abundance of craters less than 20 km in diameter and has been observed on Dione, Tethys, Mimas, and Enceladus (Kirchoff & Schenk, 2010, 2015; Kirchoff et al., 2018).

In addition, secondary craters (created when ejecta from formation of a primary crater impacts the surface) and sesquinary craters (created when ejecta orbits the body before impacting) may also play a role in modifying these surfaces (Alvarellos et al., 2005, 2017; Bierhaus et al., 2012). Production functions that are specific to the outer planets are particularly important because extrapolation of the lunar production functions past Mars (e.g., Neukum et al., 2005) yields results with large errors and does not best reflect the sources of impactors available in this region of the solar system (e.g., Campo Bagatin & Benavidez, 2012; Dones et al., 2009; Kirchoff & Schenk, 2010, 2015; Kirchoff et al., 2018; Nesvorný et al., 2011). In order to develop new constraints for impactor populations and satellite formation ages in the Saturn system, we first study the crater populations of Tethys.

2.1.3. Tethys

Tethys has a radius of 531 km, a bulk density of 985 kg/m^3 (Thomas, 2010), and an orbital eccentricity of 0.0001. The current bulk density of Tethys suggests an interior that is composed of mostly water ice and very little silicate. Recent results from Neveu and Rhoden (2019) indicate that Tethys may have had an ocean for the first ~1 Gyr post-formation, when enough heat was present to maintain one, but the ocean froze out leaving behind a solid interior.

Tethys is well known for the Odysseus impact basin (D 1⁄4 450 km) and the adjacent graben system of Ithaca Chasma (Giese et al., 2007; Moore et al., 2004). Ithaca Chasma is thought to have formed either as a direct result of the Odysseus basin-forming impact, or through the freezing out of Tethys' ocean (Chen & Nimmo, 2008; Moore et al., 2004). Studies of viscous relaxation of craters on Tethys (White et al., 2017) find that

larger craters have experienced topographic relaxation (up-doming of the crater floor and gradual shallowing of the floor) due to a period of enhanced heat flux on the satellite, further supporting the idea that Tethys has not always been a solid ball of ice.

Crater counting studies of Tethys have been conducted since the Voyager era and have found a surface that is heavily cratered. Data gathered by the Cassini mission greatly improved the resolution of Tethys' surface imagery from ~1 km/pix using Voyager images to global coverage at ~300 m/pix. This enhancement in image resolution enables studies of the surface in finer detail and expands the limit of resolvable craters to smaller diameters, enabling a more complete survey of the impact history of the body. Kirchoff and Schenk (2010) examined craters on Tethys to obtain their size-frequency distributions and found that the Odysseus basin is relatively young when compared to the cratered plains (estimates of 400 Myr–1 Gyr) while other areas of Tethys are ~4 Gyr based on the Zahnle et al. (2003) production functions. Our study expands upon the work done by Kirchoff and Schenk (2010) by mapping craters and building size-frequency distributions based on the high-resolution (<200 m/pixel) images obtained by the imaging science subsystem-narrow angle camera (ISS-NA) (Porco et al., 2004) onboard the Cassini spacecraft.

We catalogue now-resolvable craters as well as other smaller scale lineations and potential pit chains, not previously mapped. We also examine the distributions of elliptical and polygonal craters on Tethys. Elliptical craters are thought to form when the impactor comes in at a low angle (<15°) (Bottke et al., 2000; Elbeshausen et al., 2013; Gault & Wedekind, 1978; Melosh, 1989; Schultz & Gault, 1990); mapping their abundance on Tethys can provide insight into dynamics of the impactor population.

Polygonal craters form in areas that have preexisting structural weaknesses in the subsurface (Beddingfield et al., 2016; Öhman et al., 2010). For example, a study of polygonal craters on Dione (Beddingfield et al., 2016) revealed a genetic relationship between mapped polygonal craters and fault orientations in Dione's subsurface. Hence, polygonal craters can reveal information about the subsurface of Tethys that would otherwise be inaccessible.

Our data provide a more complete accounting of the crater distributions on Tethys' surface, which can inform dynamical models of the formation and evolution of the system. We describe the procedures used for gener- ating the image mosaics, criteria for crater mapping, and the resulting analysis following recommendations by the Crater Analysis Techniques Working Group (1979). We find that Tethys' small-scale crater record has regional differences in impactor populations, which imply that planetocentric impactors, with characteristics unique to the Saturnian system, played an important role in modifying Tethys' surface.

2.2 Methods

2.2.1 Image Location

We utilized the USGS PILOT website (Bailen et al., 2013, https://pilot.wr.usgs.gov/) to identify images taken by the Cassini ISS-NA (Porco et al., 2004) that were geographically distributed, had the desired image resolution of better than 200 m/pix, and had appropriate lighting conditions and viewing geometries for crater mapping. We identified 14 suitable images within five regions: one on the leading hemisphere near Odysseus (Region 1), three on the trailing hemisphere near Ithaca

Chasma (Regions 2, 3, and 5), and one at the edge of the Odysseus' antipode (Region 4). By mapping on the leading and trailing hemispheres, we can begin to assess whether there is an asymmetry in the crater distributions. Similarly, the antipodal region can be used to investigate the possibility of any disrupted terrain or secondaries from the Odysseus forming impact. Table 2.1 lists the images used in this study, their pixel scales, center coordinates, incidence angles, and phase angle. Figure 2.1 shows the mosaic footprints in the context of Tethys' surface geology.

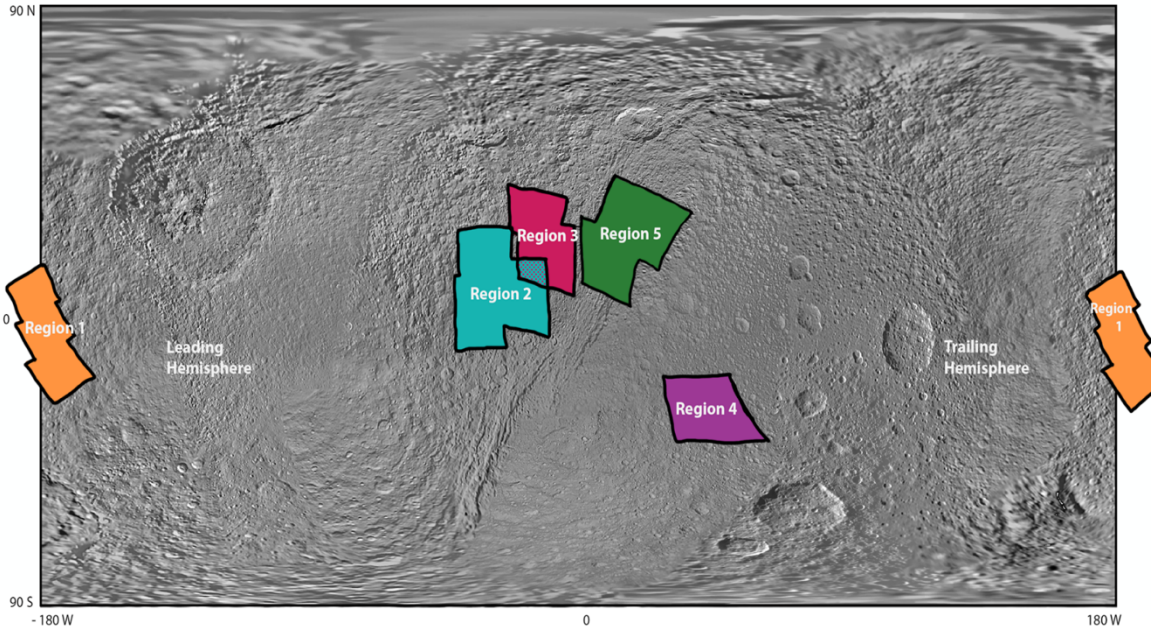

Figure 2.1. Tethys basemap by Roatsch et al. 2009 with footprints outlining each area mapped in this study.

Table 2.1. Images used in the study

Image	Resolution (m/pix)	Center Lat/Lon (°)	Incidence Angle [1] (°)	Phase Angle [2] (°)	Mosaic/Image Area (km^2)
Region 1					
N1713137226_1	106.83	3.61 N 177.75 E	41.240	69.570	47,565.40
N1713137436_1	116.19	6.890 S 181.37 E	41.422	66.681	
N1713137645_1	125.96	19.33 S 186.07 E	44.753	74.209	
Region 2					
N1561668012_2	141.12	3.37 N 342.30 E	58.148	83.174	75,832.31
N1561668355_2	154.88	14.35 N 329.11 E	73.234	77.172	
N1561668192_2	148.40	1.07 S 327.68 E	70.722	79.813	
Region 3					
N1561667141_2	115.70	28.66 N 344.35 E	68.264	102.646	45,822.60
N1561667296_2	118.82	23.78 N 346.82 E	63.675	98.711	
N1561667401_2	121.34	20.49 N 348.56 E	60.475	96.162	
N1561667506_2	124.17	17.11 N 350.17 E	57.3209	93.714	
N1561668522_2	163.78	16.73 N 348.83 E	56.326	74.698	
Region 4					
N1506219742_1	155.72	28.10 S 41.27 E	40.264	19.137	40,765.98
Region 5					
N1561668728_2	172.48	15.65 N 7.97 E	40.74	72.72	68,440
N1561668893_2	180.75	26.33 N 18.97 E	40.46	70.79	

[1] Incidence angle is defined as the angle between a surface normal to the planet's surface and the sun

[2] Phase angle is the angle between the camera and the sun at the time of observation

2.2.2 Image Processing

All images were processed using the USGS Integrated Software for Imagers and Spectrometers (ISIS3; Anderson & Sides, 2004). Images were converted from PDS format to ISIS3 compatible format (ciss2isis). The spacecraft navigation and pointing location were added to the files via spiceinit. Data were then radiometrically calibrated using cisscal, which converts digital number (DN) values into I/F (Intensity/ Flux) values. A lowpass filter was applied to the images, followed by a trim of 1–2 null pixels on the sides of the images. If the images were not part of a mosaic, they were map projected and brought into ArcGIS. If the images were to be part of a larger mosaic, we attached the camera statistics using camstats then initiated the image footprints using footprintinit, found the overlap between the images using findimageoverlaps, and created the overlap statistics via overlapstats. These steps were necessary to properly prepare the images to be controlled (illustrated in Figure 2.2). If two images have an overlap, a crater in the images can be used as a control point. A crater in image A could be shifted by a few kilometers in image B due to slight differences in the observation geometry between the two observations. To ensure the images line up at the same location in both images,

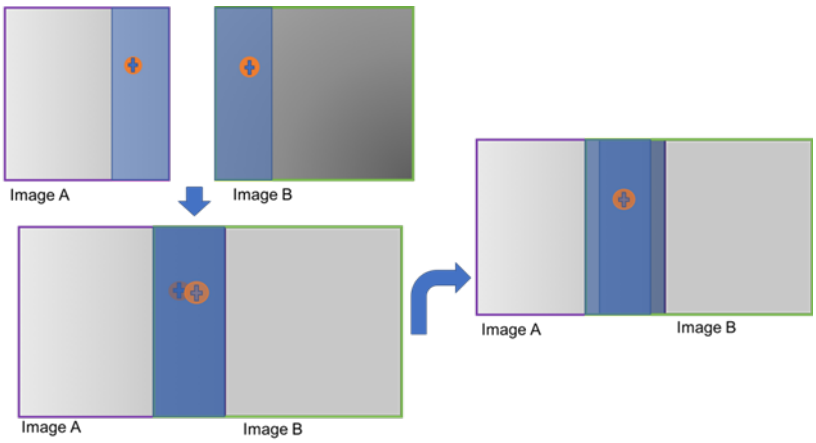

Figure 2.2. Schematic of the control net process. Images A and B have a common impact crater in the image (orange circle with + symbol inside). The goal in this process is to align the crater between the two images so that there is no visible seam between the images in the final mosaic. The resulting product is an image where the plus in the center of the crater is perfectly aligned between both images.

image B is adjusted so that the control crater in image B lines up directly over that same crater in image A. This process ensures a mosaic with barely visible seams since the area of overlap between the two images was controlled premosaicking.

A definition file is needed to initiate the control net; ours was modified from the standard USGS file. We generated seed points within the control net using Autoseed and visually inspected the resulting net to ensure that the placement and number of points across all images were appropriate. Cnet was then run to manually align each point with the same point in the second image, which ensured better geospatial control of the final mosaic. Once the process was completed for all seeded points, cnetcheck was run to check that all points were tied to other images and that there were not any parts of the image overlaps that were missing any control points. Jigsaw was run to apply the control net to the images, and the images were then map projected and mosaicked. Figure 2.3 summarizes our image processing workflow using the ISIS3 commands.

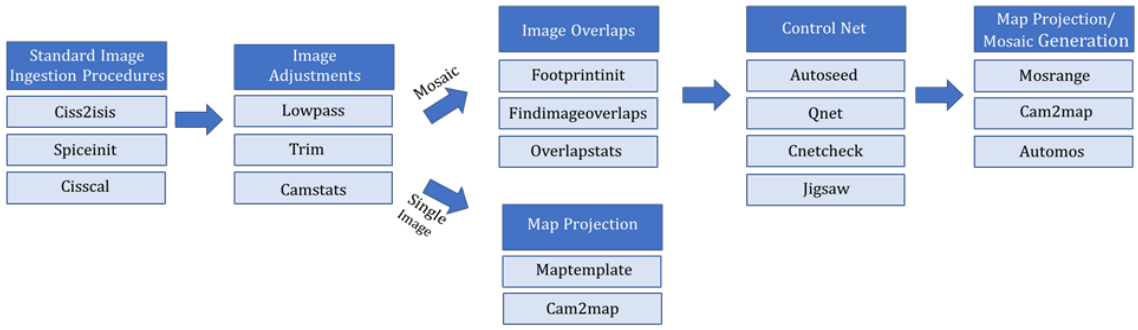

Figure 2.3. Image processing flowchart for Cassini ISS data. Commands listed in each box are the commands that were used in ISIS3 to process the data. Not included are the user inputs for each command. Input arguments can be found on the USGS's support site for the program.

2.2.3 Mapping Criteria

To improve the accuracy of crater identification and measurement, we required a minimum of 5 pixels across a candidate crater (see crater counting recommendations by Fassett (2016) and Robbins et al. (2014, 2018). This resolution limit enables mapping of craters that are at least ~700 m in diameter, which would not be identifiable in the 400 m/pix Tethys basemap (Roatsch et al., 2009). A more conservative cut-off of 7 pixels across (D ~ 1 km) was used when generating the size frequency diagrams, but to assure completeness at the 7-pixel cut-off, we approached the 5-pixel limit when mapping.

Once the images/mosaics were produced, we brought the files into ArcMap and began to map on the images. We overlaid the images onto the USGS basemap (Roatsch et al., 2009), which we projected in a simple cylindrical projection. This projection meets the needs of the project since we are not mapping features far enough away from the equator to worry about distortions in polygon shape or area which would occur poleward of 50° N/S. The average pixel scale of the images used in this project was ~133 m/pix.

To facilitate crater mapping, we used the CraterHelper tools produced by the USGS (Nava, 2010). This add-on to ArcMap allowed us to record the diameter, major and minor axes, and the latitude and longitude information for each crater. This tool also accounts for the minor distortion of a circle if a crater is mapped further away from the equator in an equirectangular projection. We relied on shadowing within the identified features to determine if they had positive or negative relief.

For us to classify a feature as a crater, it had to show negative relief as expressed by the shadowing/lighting conditions of the rest of the image, be roughly circular, and be a minimum of 5 pixels across. If a potential crater had 50% or more of the floor covered

in shadow, it was mapped as a likely crater. Craters classified as elliptical had to show signs of elongation along one of the major axes and had a measured ellipticity, defined as the major axis/minor axis, value >1.1 (Bottke et al., 2000). Additionally, we examined the azimuthal values of the major axis of the elliptical craters in each region. We measure orientation from north, where 0° north translates to a north/south orientation of the crater. Craters classified as polygonal had to exhibit connected straight rim segments, similar to the definition used in Beddingfield et al. (2016). Groups of three overlapping craters were classified as connected craters. Craters within these groups appear to be missing a portion of a rim and are joined with the other craters in the group suggesting a potential formational relationship. For larger craters, we mapped out any visible ejecta blanket; the extent of which was determined by observing where the surface texture changed from a smooth material (which was mapped as the ejecta blanket) back to the apparent rougher texture of the surrounding terrain. Example craters are shown in Figure 2.4.

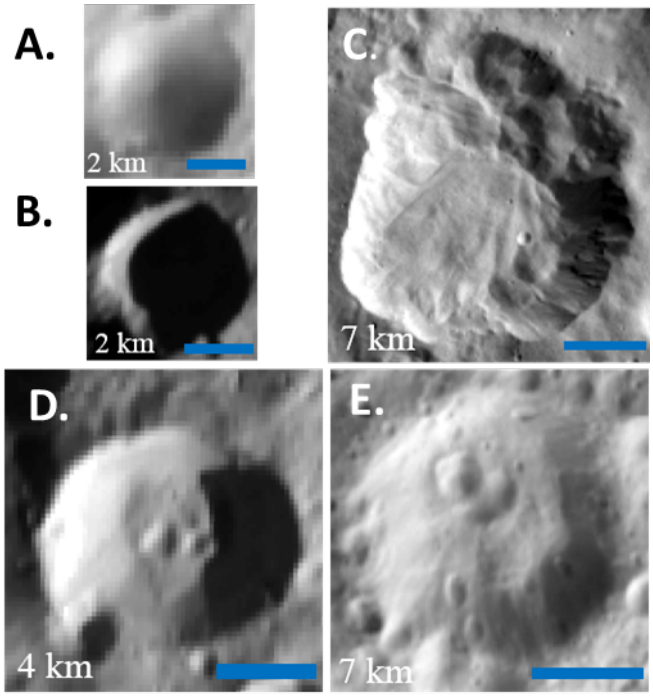

Figure 2.4. Example craters for each morphologic type**: A.** circular crater. **B.** Uncertain crater due to lighting geometry. **C**. Irregular shaped crater. Not fully circular, elongated, etc**. D**. Elliptical crater. **E**. Polygonal crater.

2.2.4 Crater Statistics

Our crater counts are presented in the form of the cumulative size-frequency distribution (CSFD) and the Relative (*R*)-Plot, which are the formats recommended by the Crater Analysis and Techniques working group (1979). To produce a CSFD, the crater diameters are sorted and plotted by taking the cumulative number of craters counted (as individual points) and dividing that by the count area (in km^2). Uncertainties in cumulative crater density are calculated as $\frac{\sqrt{N}}{A}$ where *N* is the cumulative number of craters and *A* is the count area. In general, when interpreting a CSFD, a higher position on the plot suggests the terrain is older, as that region has the highest number of craters per unit area. However, an additional source population (such as secondaries in a region near a larger impact crater) could lead to a higher curve without indicating a different age. Thus, we are also interested in interpreting differences in the slope of the CSFDs curve. Differences in slope are often attributed to differences in impactor populations, secondary cratering, or other processes like resurfacing. However, on the CSFD, more subtle differences in slopes/populations can be missed.

The R-Plot is a useful means of observing differences that might otherwise be obscured in a CSFD. To construct the *R*-Plot, data is binned in $\sqrt{2}$ increments starting from 1 km. Once the data is binned, the *R*-value is calculated using equation 2.1

$$R = \frac{\overline{D}^3 N}{A(D_a - D_b)} \qquad \textbf{Eq. 2.1}$$

, where $\overline{D}$ is the geometric average diameter value in the bin via $\sqrt{D_a D_b}$, D_a and D_b are the minimum and maximum diameter value for each bin, respectively. *N* is the number of craters within the diameter bin, and *A* is the count area. Error for *R*-values are calculated

as $\frac{\sqrt{R}}{A}$. All plots are displayed on a logarithmic scale. As in the CSFD, curves that plot higher on the y-axis are suggestive of older terrain, excluding the possibility of secondaries, because there are more craters per unit area on that portion of the surface.

2.3. Results

Figures 2.5–9 show our mapping results for each region. The first part of each figure shows the mosaics/images (a) before any mapping and (b) after mapping. For easy comparison across regions, Table 2.2 summarizes the number of craters per 1 km diameter bin for each region, and Table 2.3 breaks the crater counts down into our five morphological categories. Connected craters were not included in the counts/analysis due to difficulties in measurement, but their presence is still noted; all other crater feature classes are included in the size-frequency distributions.

Figure 2.5 shows Region 1, which is the closest to the Odysseus impact basin and displays all five of our crater classification types. We additionally mapped linear features in this area (Figure 2.11a). Crater counts within Region 1 show a total of 990 craters with morphologic breakdowns of 848 circular, 91 elliptical, 10 polygonal craters, 4 irregular craters, 0 connected craters, and 37 likely craters. We note the presence of four connected craters as well. Most of the linear features tend to have an east/west orientation (Figures 2.11a and 2.13). The long, connected crater (green) in the bottom panel of the mosaic does extend into images on the east and west side, so it is a large potential crater chain. Orientations of the elliptical craters also trend along an east/west direction, with some

spread. We map the 1–2 km craters (green points) separately from the impacts or impacts from debris released from Tethys' co-orbital satellites.

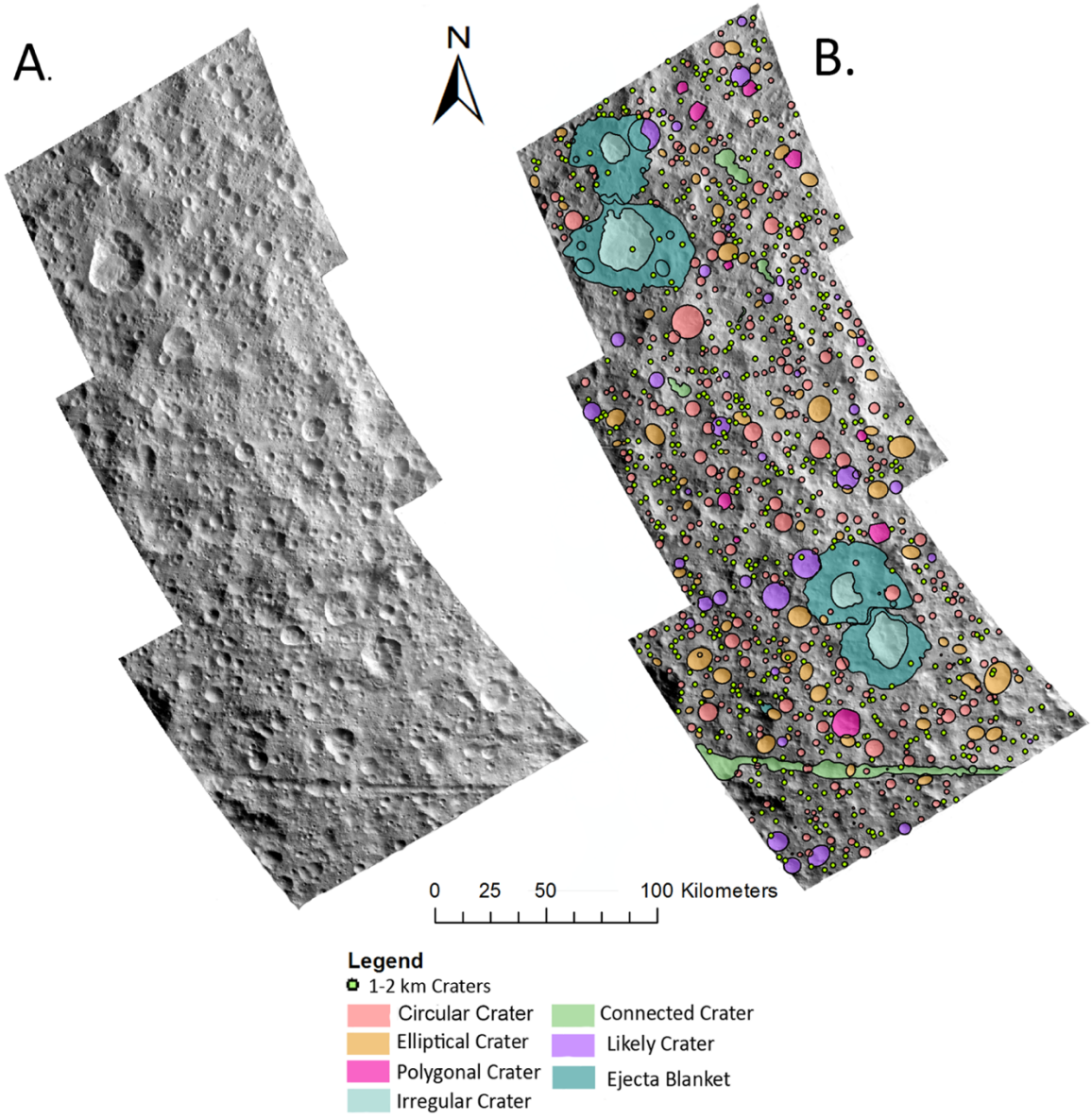

Figure 2.5. Unmapped and mapped mosaics of Region 1. (A) shows the unmapped mosaic. (B) shows the mapped mosaic with all features shown This region displays the highest number of craters and lineations of all mapped study areas. This is also the region closest to the Odysseus impact basin. For larger craters, any visible ejecta blanket (softened terrain appearance relative to the surrounding terrain) was also mapped. Crater color corresponds to the morphologic type. 1-2 km diameter craters are shown only as points due to the scale.

In Region 2.6, near Ithaca Chasma (Figure 2.6), we counted 792 craters with 615 being circular, 88 elliptical, 9 polygonal, 1 irregular crater, 1 connected crater, and 79 likely craters. All 88 elliptical craters here have diameters larger than 2 km, which comprises 11% of the total mapped craters in Region 2. There are fewer lineations when compared to Region 1, and their orientations are nonuniform. We also note fewer polygonal craters in this region compared to Region 1. This region contains many "likely" craters, mainly due to lighting conditions on the western portion of the mosaic. This lighting would result in a shadow that covered more than 50% of the crater.

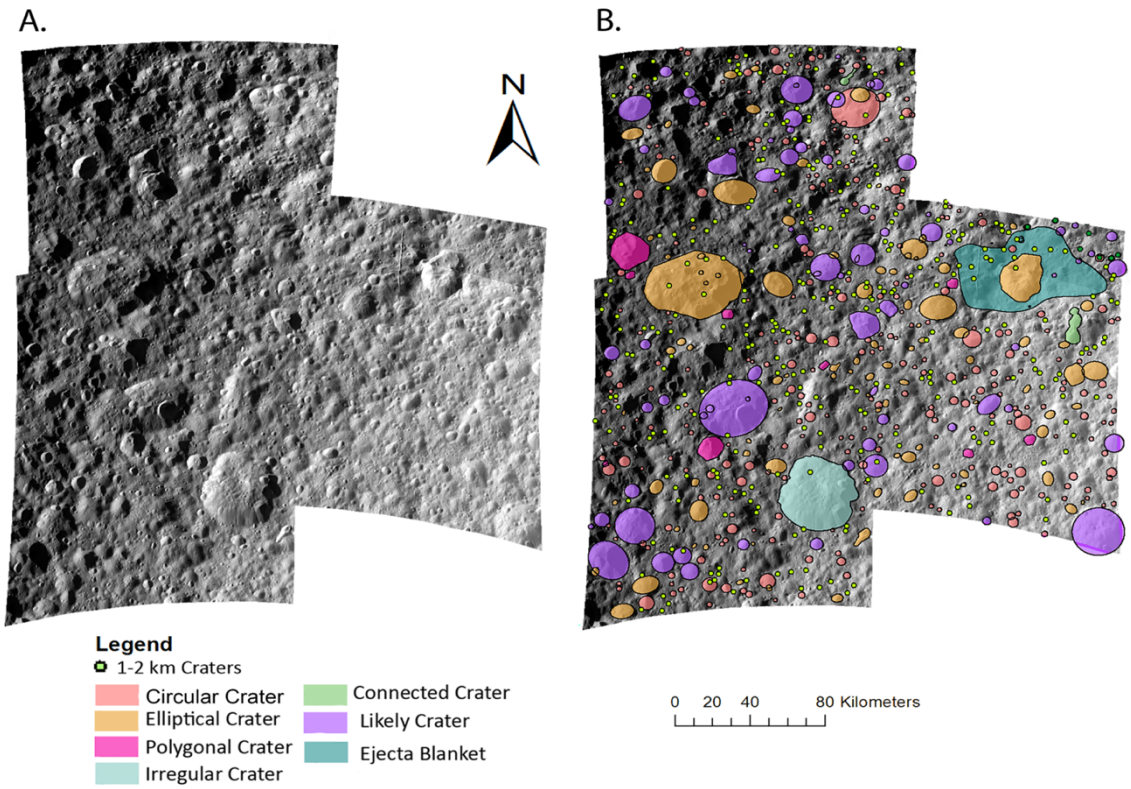

Figure 2.6.Unmapped and mapped mosaics of Region 2, which is located near the Ithaca Chasma canyon system. A. The unmapped mosaic, which has lighting conditions that change slightly moving from left to right. B. The mapped mosaic with all features shown. We note the starred crater in the top right panel (shared in Region 3) (Fig. 2.7), which is a type example of our irregular crater feature class.

Our crater counts in Region 3, located near Ithaca Chasma (Figure 2.7), revealed 638 craters across this area. Within the morphological subdivisions of craters, we see 491 circular craters, 91 elliptical craters, 9 polygonal craters, 0 irregular craters, 0 connected craters, and 47 likely craters. Region 3 (Figure 2.7) shows more diversity in the morphological classes of the linear features observed on the surface. This region also ties Region 2 in the number of polygonal craters but has more elliptical craters. There is a substantial ridge that begins within our mapped area and extends onto the basemap.

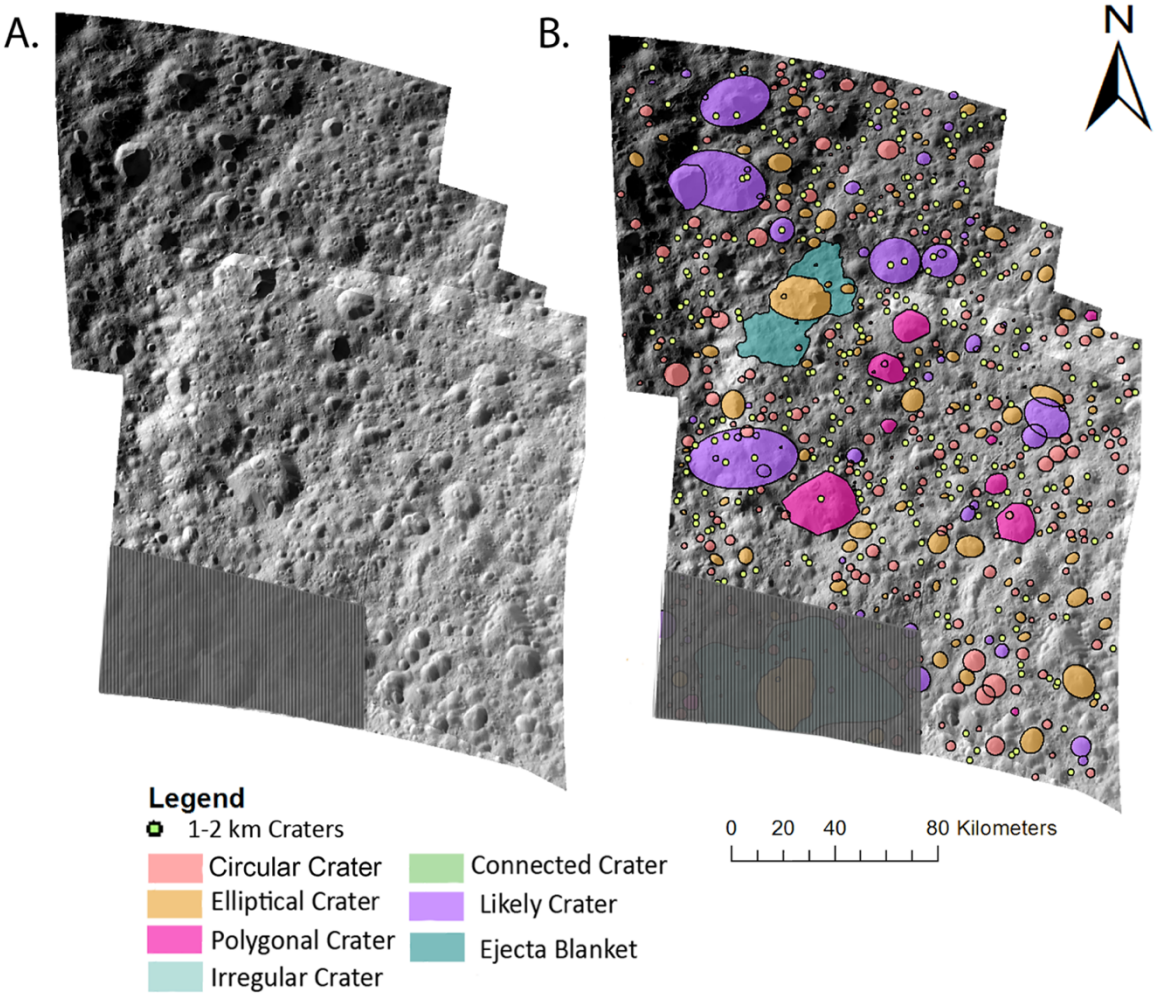

Figure 2.7. Unmapped and mapped mosaics of Region 3, near Ithaca Chasma. (A) shows the unmapped mosaic which has lighting conditions change slightly moving from left to right and top to bottom. (B) shows the mapped mosaic with all features indicated. Grey striped area is shared with Region 2 (Fig 2.6.). Region 3 has more elliptically shaped craters than the other mapped mosaics.

Regions 2 and 3 are located near the Ithaca Chasma tectonic system, such that the regional geology may have been influenced by the formation of Ithaca Chasma.

Our counts in Region 4, located near the antipode of Odysseus (Figure 2.88), revealed a total number of 590 craters: 518 circular craters, 39 elliptical craters, 7 polygonal craters, 0 irregular craters, 0 connected craters, and 26 likely craters. Overall, Region 4 does not show a large range of different features, as compared to the other three regions. It is primarily populated with simple bowl-shaped circular craters with a smaller proportion of elliptical craters. It shows fewer linear features than the other three regions as well. Region 4 was an area we included in this survey due to its proximity to the antipode of Odysseus, which may have affected its surface evolution differently than the other regions. We do not see evidence of disrupted terrain or a distinct difference in the terrain when compared to the surrounding surface or any abundance in one crater size over another. Based on a ballistic trajectory assumption (e.g., Moore et al., 1974), we hypothesized that the antipodal regions (Region 4) on Tethys would exhibit more smaller

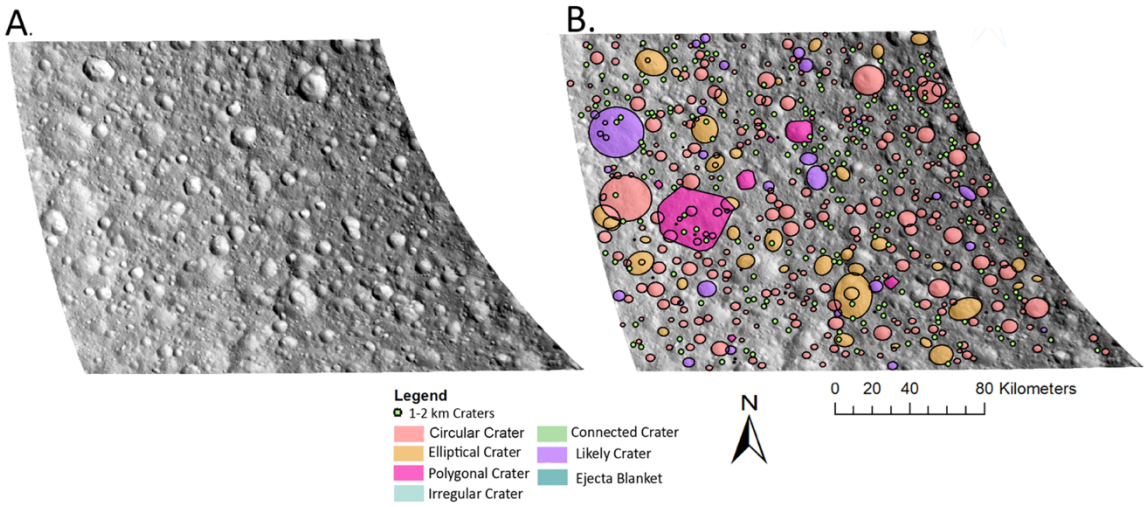

Figure 2.8. Unmapped and mapped mosaics of Region 4. (A) shows the unmapped mosaic. (B) shows the mapped mosaic with all features shown. Region 4 has fewer craters of all kinds when compared to the other mapped regions. It also does not have as many tectonic structures as the other regions.

craters than other regions due to ejecta from Odysseus, but we found the smallest population of 1–2 km impacts (197, Table 2.2), suggesting that secondaries from Odysseus are not as prevalent in this area of Tethys. More details on secondary crater modeling from Odysseus can be found in Ferguson et al. (2018) and Bierhaus et al. (2018) (full model details).

Region 5 (Figure 2.9) overlays a portion of the Ithaca Chasma graben system where we observe a total of 965 craters: 826 circular craters, 120 elliptical craters, 7 polygonal craters, 11 irregular craters, 0 connected craters, and 1 likely crater. Due to the location of this mosaic, this area represented an opportunity to solidify trends possibly related to Ithaca Chasma that appear in the data for the neighboring Regions 2 and 3. Unlike the other mapped regions, this region directly overlies an extensive network of tectonics within Ithaca Chasma, which can affect the cratering record on that portion of the surface. Region 5 exhibits the most irregular shaped craters with 11, which could be indicative of more extensive crater modification within Ithaca Chasma.

Craters that we classified as “likely” may be older than some of the neighbor craters, which is suggested by the “softening” of the apparent rim. These craters tend to be larger and have been added into the CSFD and R-plots. Even in cases where the lighting made for a less certain identification, we think the “likely” craters are most likely of impact origin since Tethys does not display volcanic craters or other landforms that could be mistaken for an impact crater.

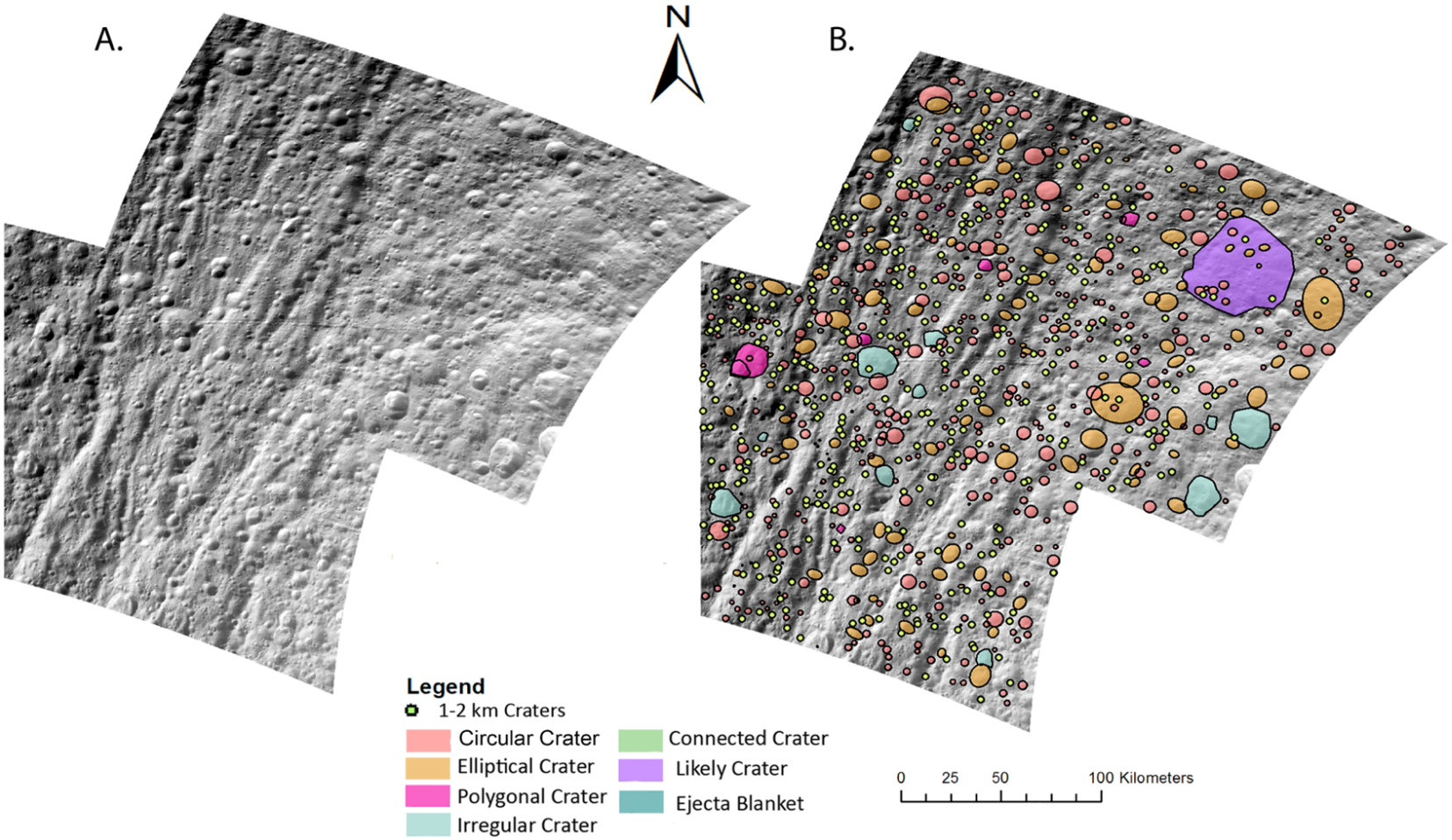

Figure 2.9. Unmapped and mapped mosaics of Region 5. (A) shows the unmapped mosaic. (B) shows the mapped mosaic with all features indicated. Region 5 has a high density of small craters, but is lacking in craters larger than 7 km.

Comparisons of crater distributions are illustrated in Figure 2.10. The roll-off of the CSFD in Figure 10a from increasing values with decreasing diameter to flat values with diameter at D = 1 km indicates that our data are complete to D = 1 km (see Robbins et al., 2014), as was our goal by measuring craters down to 5 pixels across (see section 2.2.3). We do not observe many craters larger than 30 km across our five regions, which is to be expected in the relatively small areas in which the counts are completed. From Figure 2.10a, only seven more craters across all mapped regions have diameters above 30 km. In addition, a large regional survey by Kirchoff and Schenk (2010) observed a lack of large craters in the global mosaics between 30 km and 80 km; 75% of our total observed craters across all five regions fall within the diameter range of 1–4 km (see Table 2.2 for exact numbers).

Table 2.2. Crater counts in 1 km diameter bins between all five regions and the total number of craters in each bin.

Diameter Bin (km)	Region 1	Region 2	Region 3	Region 4	Region 5	Total
0-1	24	10	42	23	59	158
1-2	484	306	245	197	365	1597
2-3	222	201	157	142	197	919
3-4	105	90	85	75	121	476
4-5	53	54	44	60	75	286
5-6	30	38	18	21	39	146
6-7	20	27	11	18	30	106
7-8	14	8	8	18	29	77
8-9	15	11	4	15	12	55
9-10	7	10	7	3	11	38
10+	18	37	17	18	27	117
Total	**990**	**792**	**638**	**590**	**965**	**3975**

Table 2.3. Number of craters in each crater morphology category that have measured diameters.

Crater Type	Region 1	Region 2	Region 3	Region 4	Region 5	Total
Circular	848	615	491	518	826	3298
Elliptical	91	88	91	39	120	429
Polygonal	10	9	9	7	7	42
Irregular	4	1	0	0	11	16
Uncertain	37	79	47	26	1	190
Total	990	792	638	590	965	3975

Our CSFD has Region 1 plotting higher at small crater diameters, indicating a relative excess of small craters with diameters between 1 and 3 km. Within the diameter range of 3–10 km, Regions 1, 4, and 5 all have relatively similar slopes, being shallower-sloped (<−2 cumulative) for D ~ 3–8 and steeper-sloped (>−2 cumulative) for D ~ 8–10 km, with some small variations in distributions within error. Regions 2 and 3 plots slightly lower crater densities than the other three areas in this diameter range and appear to have somewhat different shapes. Region 2 has a shallow slope from D ~ 3–5 km, similar to Regions 1, 4, and 5, but then attains an approximately −2 cumulative slope (flat R-values) for D ~ 5–10 km. Meanwhile, Region 3 appears to have an approximately −2 cumulative slope for D ~ 3–10 km. Thus, the crater SFD shapes for Regions 2 and 3 have more similarity to each other than Regions 1, 4, and 5 in this diameter range. Between 10 and 20 km in diameter, some interesting changes happen in the shape comparisons: Regions 2, 3, and 4 seem to be similar with an approximately −2 cumulative slope, while Regions 1 and 5 have a similar shape with a very steep slope until D ~ 13 km followed by a very shallow slope ("v" shape in the R-plot, Figure 10d). The five regions seem to become consistent again at ~20 km diameter, but due to small number statistics at these diameters, we cannot determine differences outside of uncertainties. Table 2.3 illustrates the breakdown of morphology types within our mapping.

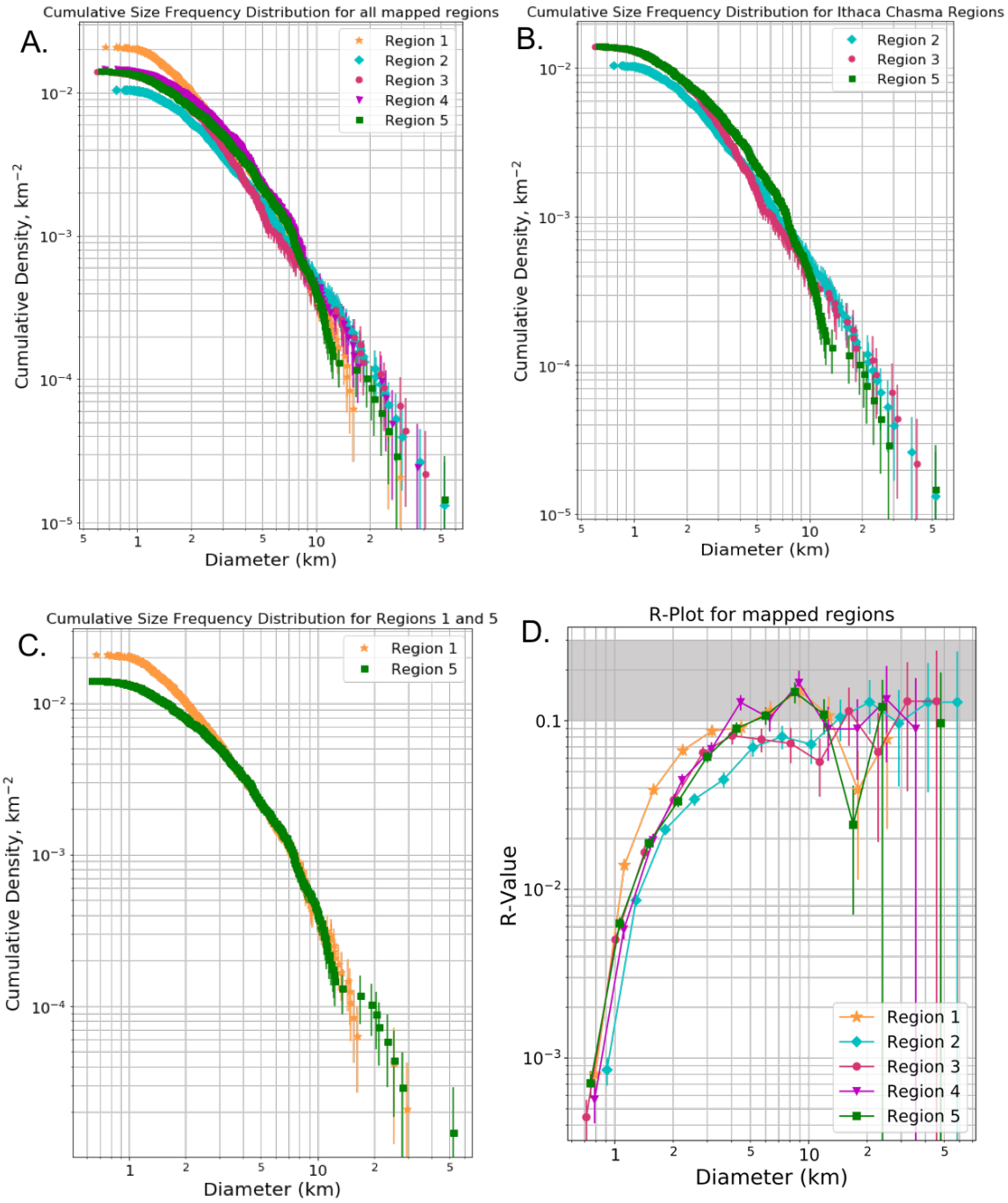

Fig 2.10. Size frequency distributions for the mapped terrain. 10A. Cumulative size frequency diagrams for all five regions. We observe an increase in small craters in Region 1 (orange stars) relative to the other terrain units. 10b shows the CSFDs for the three regions located near/on Ithaca Chasma, showing that between 1-2 km Regions 3 and 5 were likely impacted by the same population. 10c: CSFD for Regions 1 and 5 showing a distinctly similar shape to each other between 3.5 and 11 km. 10d: R plot for mapped terrain on Tethys. We still observe an increase in small craters in Region 1 (1km < D < 3km).

Figure 2.11 illustrates the tectonic mapping that was completed over the five regions. The number of tectonic features varied across the regions but were most prevalent in Regions 1 and 5. Our nomenclature for these features was chosen as such to avoid implications of the formation process.

2.4. Discussion

2.4.1. Crater Results

In terms of the relative ages between the mapped areas, the similarity of the cumulative densities over most diameters indicates that these regions are basically all of similar age. Looking at the small differences suggests Region 1 is the oldest of the five regions, then Regions 4, 5, and 3 have intermediate ages, and Region 2 is the youngest area. We have based this interpretation on the fact that Regions 1, 4, and 5 have higher R-values on the R-plot than the other two mapped regions at diameters between ~5 and 10 km (Figure 2.10d), which is indicative of a relatively older age, if these craters are produced by primary impactors, or an additional source of nonprimary impactors to account for the large number of small craters. This trend is also confirmed when viewing the CSFDs (Figures 2.10a–10c).

The curves for Regions 1 and 5 are distinctly different in shape than the other mapped terrain (Figure 2.10). First, Region 1 has the increase in crater density for 1- to 3-km craters. Second, Regions 1 and 5 show a very steep slope at D ~ 7–15 km, which is suggestive of large craters being relatively absent from these areas. While this comparative lack of craters does appear real, as the difference in density occurs outside of our computed uncertainties, the smaller number of craters (D > 15 km) does introduce issues with small number statistics. Thus, we cannot be completely confident this

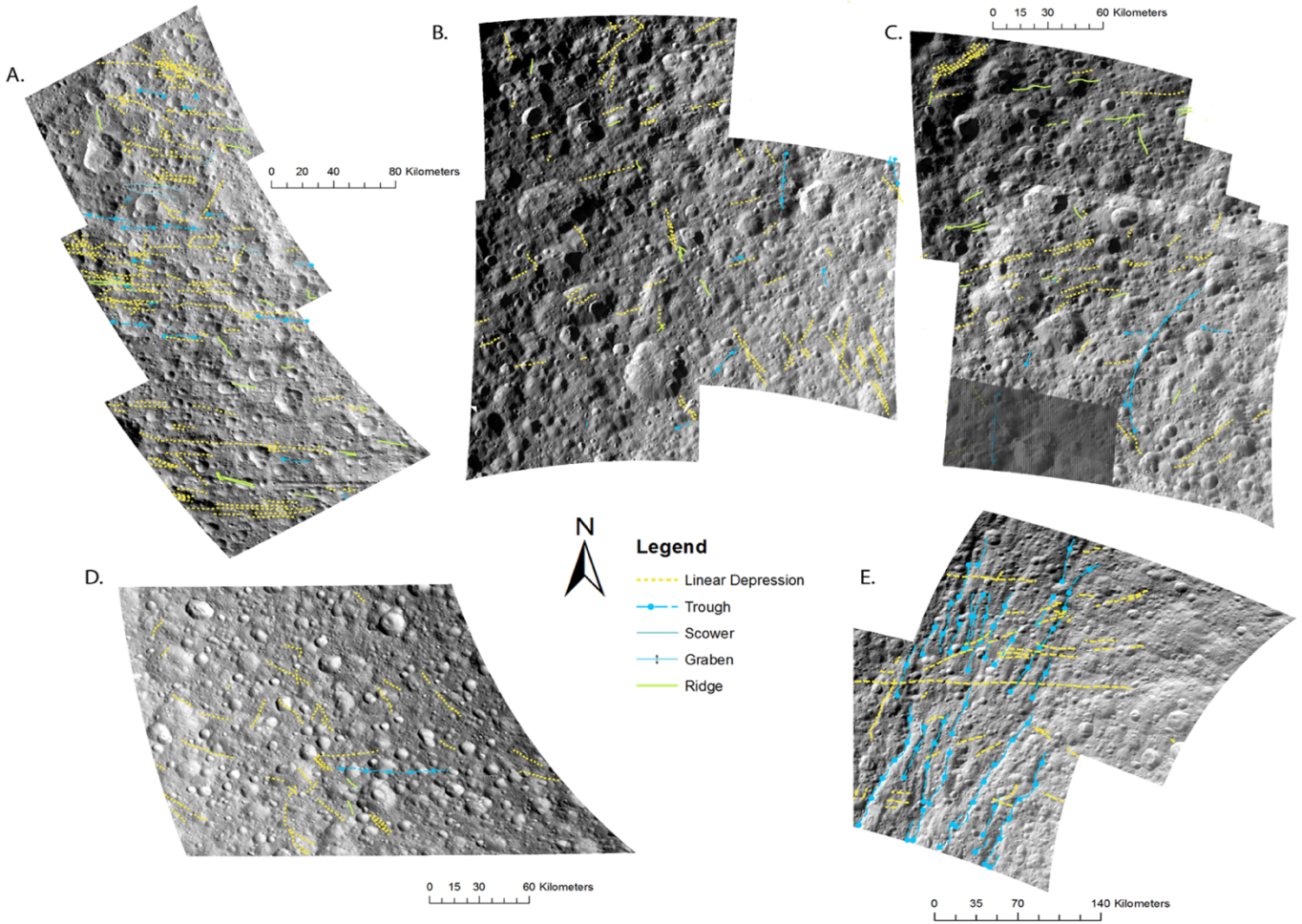

Fig 2.11. Tectonic maps of the 5 regions surveyed in this study. A. Region 1, B. Region 2, C. Region 3, D. Region 4, E. Region 5. Between the five areas, Region 1 shows the largest number of linear features and with a consistent directional pattern regardless of morphology. Orientations of Region 5' s features can be broken down between Ithaca Chasma (predominately oriented N/S) and all other linear features (predominately oriented E/W)

comparative lack of D ~ 15 km craters in Regions 1 and 5 is real. Furthermore, we cannot suggest an obvious reason for this observation. The locations associated with Ithaca Chasma and other tectonics is suggestive of a relationship, but given that Regions 2 and 3 are also near Ithaca Chasma, we are unable to make a clear connection and propose an erasure process.

Comparing our regional mapping to the production functions from Zahnle et al. (2003) as endmembers (Figure 2.12), we see that neither Case A nor Case B (see section 2.1.2 for descriptions of potential impact populations) fit the slopes at all sizes and/or regions but portions of each distribution is fit by one or the other. Region 1's CSFD has a shape that is fit well by Case A from D ~ 1.5–2.5 km and by Case B for D ~ 4– 8 km. In Region 2, Case A currently only lines up with diameters between ~1.5–4 km and Case B matches up at D ≥ 10 km. Within Region 2, neither case from Zahnle et al. (2003) perfectly fits the diameter ranges from ~4 to 10 km. Region 3's best fit from these production functions comes at D ≥ 4 km, with only Case B fitting well. With diameters larger than 10 km, small number statistics are likely to factor in more to these diameter ranges, so with more large craters that fit might change. In Region 4, Case A fits only at ~2–4 km and fits Case B at ~D > 4 km. Region 5 agrees with a Case A between ~2 and 5 km in diameter and at D > 7 km the Case B function fits more within the error bounds.

As discussed in detail in section 1.2, we suggest that Case A is most consistent with a heliocentric population, while Case B is most consistent with a planetocentric population (Dones et al., 2009; Kirchoff et al., 2018; Singer et al., 2019). Furthermore, even though Case B is derived from Triton data and would apply in detail only to the Neptune system, it may be generally representative of what a planetocentric population

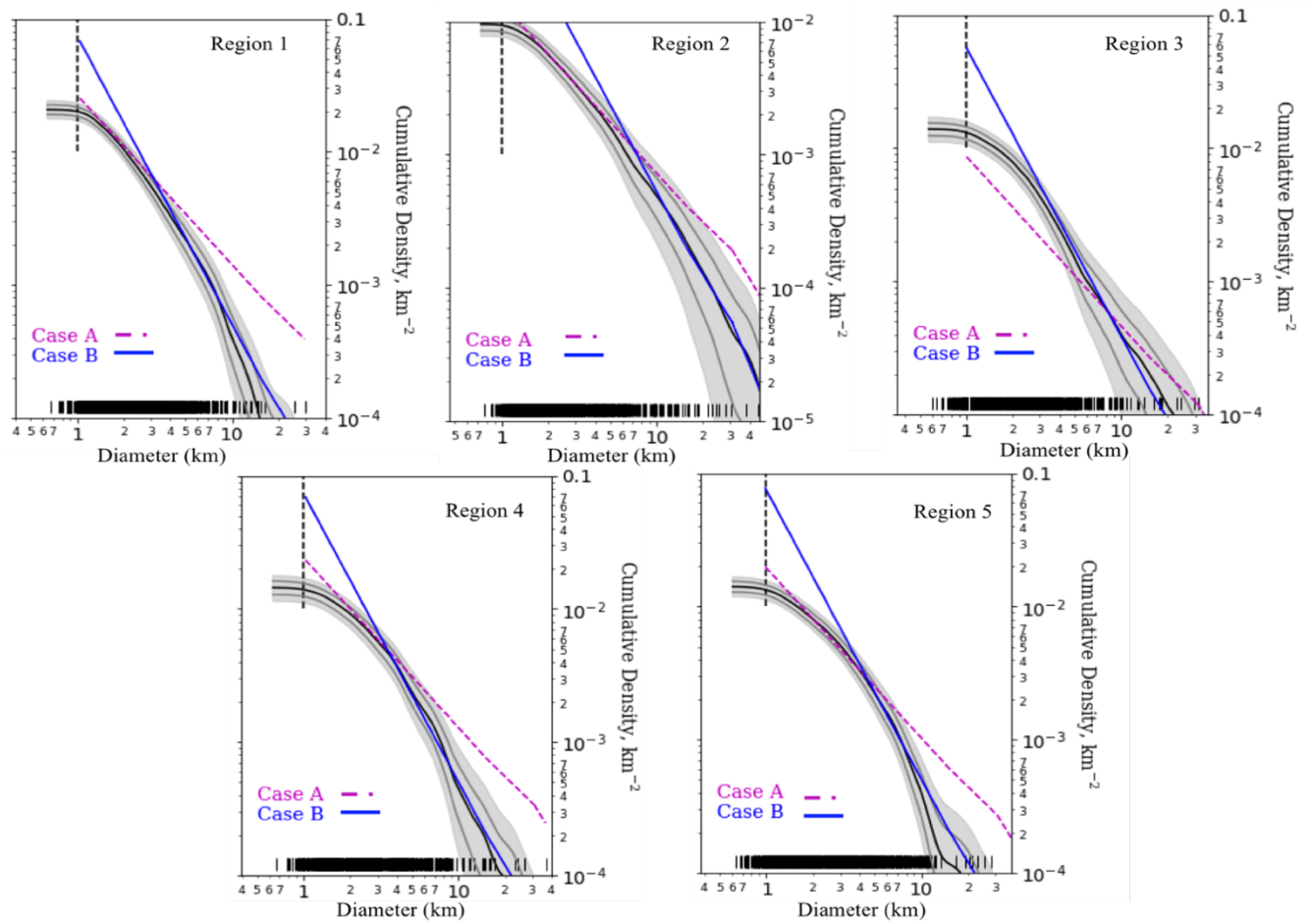

Figure 2.12. CSFD's for each region with Zahnle et al., 2003 production functions plotted on top of the crater counts. Black curves and grey envelopes represent the SFD and calculated error using the kernel density estimator and bootstrap approaches by Robbins et al. (2018). The vertical black dashed lines indicate our completeness diameter of 1 km and the short vertical lines at the bottom of the plots show each individual diameter measurement (a.k.a., rug plots). The Case B line (blue) matches slope nicely for most regions around D 10 km, but Case A appears to fit the shape of the curves of Regions 2-5 at diameters between 2 and 4 km. While not a perfect fit, the shape is a better fit than the shape of the Case B curves.

may look like. In all five regions, D ~ 7–10 km generally aligns best with the Case B slope. In Regions 1, 2, 4, and 5, their CSFDs at small diameter (~1 km < D < 5 km) generally agree best with Case A. This Case A scenario does match up with bodies across the outer solar system (Singer et al., 2019) but not fully at Saturn which further points to a different bombardment source/history for this system.

There are some potential implications of these results that will require additional work to investigate. First, because the observed crater SFDs fit neither the predicted heliocentric nor general planetocentric populations, there may be value in deriving an implied impactor SFD that includes the anticipated heliocentric population as well as a Saturn-specific planetocentric population. Currently, the planetocentric populations that are available for comparison with our crater counts are based on Triton. Given that formation scenarios for the midsized moons of Saturn include accreting from ring material during outward migration from Saturn and re-accumulation after disruption of a previous generation of moons, the debris available to impact Saturn's moons may be quite unlike that of the Neptunian system.

Similarly, it would be valuable to understand how SFDs might change through time. We see changes in slopes between the SFDs of younger and older regions, but the changes are difficult to interpret. The observed crater SFDs would likely differ between (a) a population of impactors that slowly changed from one dominated by planetocentric debris to one dominated by heliocentric debris and (b) a spike in planetocentric debris (e.g., from the break-up of a moon). The timing matters because new craters are superimposed onto older craters; the relative sizes and the flux of impactors will change how the surface is modified and the extent to which older populations are preserved.

In the context of the debate on the formation ages of the satellites (Ćuk et al., 2016; Neveu & Rhoden, 2019), our results could currently work in either scenario of young or old moons. If the moons formed near-contemporaneously with Saturn, we suggest that they could experience a steady planetocentric flux early on that becomes depleted as time increases.

Observed 1–2 km craters could be from small primary impact events, or they could be secondary craters from other larger primary impacts on the surface. If these are primary impacts, it is unclear what their source may be. One method of determining the input of different impactor populations is the presence of a leading/trailing asymmetry in the crater record on synchronously rotating bodies (Horedt & Neukum, 1984b; Shoemaker & Wolfe, 1981; Zahnle et al., 2001). The presence of this type of asymmetry is expected when the body has been cratered by a primarily heliocentric population, where the leading hemisphere is expected to be hit more often than the trailing side. However, crater saturation can obscure the pattern (Charnoz et al., 2011; Dones et al., 2009; Lissauer et al., 1988). Within the Saturn system, no unambiguous asymmetry has been observed on these moons (Hirata, 2016; Horedt & Neukum, 1984b; Kirchoff & Schenk, 2010; Zahnle et al., 2001), which implies predominantly planetocentric impactors, nonsynchronous rotation, or that the surfaces are saturated. We note, however, that our mapped regions are not located directly at these points on the surface, and counts from those areas would need to be compared to fully assess the potential for an asymmetry.

There are other possible explanations for the differences in density we see for small craters ($D < 3$ km in Region 1). This difference in shape of the size frequency

diagrams suggests that the small crater population has been preferentially enhanced in Region 1 compared to the other areas on Tethys. Potential sources of the enhancement are secondary craters or sesquinary craters, or where the debris that created the smaller craters came from one of Tethys' co-orbital satellites, Telesto or Calypso (Alvarellos et al., 2017; Bierhaus et al., 2012, 2018; Nayak & Asphaug, 2016; see Dobrovolskis et al., 2010, for the models of ejecta exchange between the moons). Overall, we are seeing size distributions that are suggestive of a Saturn-specific planetocentric population along with an enhancement of the small crater population near the anti-Saturn point (Region 1). Our investigations of elliptical craters showed a preferred east/west direction along their major axis. Regions 1 and 5 elliptical craters show the concentrated distributions, whereas Regions 2, 3, and 4 have directions that have a wider spread in orientations.

For the discussion so far, we have not included the possibility of crater saturation equilibrium. When a planetary surface has accumulated such a high number of craters that the formation of any new crater erases an existing one, that surface is characterized as having reached crater saturation equilibrium (e.g., Chapman & McKinnon, 1986). To evaluate whether our regions have reached saturation, we use the criteria described by Richardson (2009) where the surface has likely reached saturation if it has an R-value between 0.1 and 0.3 (represented by the gray bar in Figure 2.10d). For the conservative value of $\geq$0.1, we find that each region is saturated for some diameters: Region 1 from D ~ 5 to 13 km, Region 2 for D > ~15 km, Region 3 for D ~ 15 km and D > 30 km, Region 4 from D ~ 4 to 12 km and D ~ 25 km, and Region 5 from D ~ 6 to 12 km and D ~ 25 km. Because these are overall shallow-sloped distributions ($\gtrsim -2$ on average), the shape of the production population is not likely lost (e.g., Chapman & McKinnon, 1986;

Richardson, 2009). Therefore, if these terrains are saturated at these diameters, our discussion about crater SFD and impactor population shapes is not affected. However, our discussion of relative ages could be since saturation equilibrium implies crater density increases are not recorded after a certain point. Nevertheless, the observation of saturation to a restricted range of diameters indicates that the overall trend of relative ages discussed is likely unaffected. If a less conservative value of ≥0.2 is used, then none of the regions are saturated at any diameter.

2.4.2. Other Surface Features on Tethys

Lineations in our mapped regions have a variable range of values in their orientations. This could suggest different epochs of stressful events on Tethys' crust. The features also have a range of cross-cutting relationships, implying that they did not form simultaneously. We find that the lineations in all four regions do not line up with the general trend of Ithaca Chasma. Ithaca Chasma has a mean orientation between 15° and 30°, Region 1 has a mean at 103°, Region 2 at 116°, Region 3 at 78°, and Region 4 at 161° (Figure 2.13). Tectonics of Region 5 were mapped, inclusive of Ithaca Chasma with an average value of 61°. Within Ithaca Chasma, we identified features that are a part of the canyon system, and then, there are features that are aligned approximately perpendicular to the dominant direction of Ithaca Chasma (light green in Figure 2.13) This implies that the tectonic events that created our mapped lineations were formed by a different process than what formed Ithaca Chasma. Observed lineation directions in Region 1 support our interpretation that non-heliocentric debris is responsible for the excess of small craters. Due to resolution limits, we cannot currently count craters on these features to determine their relative ages. Our mapping of polygonal craters reveals

relatively low numbers of them in our final counts. The highest concentration is located next to/in Ithaca Chasma as a part of Regions 2, 3, and 5 hinting that the subsurface has further been fractured by the formation of Ithaca Chasma.

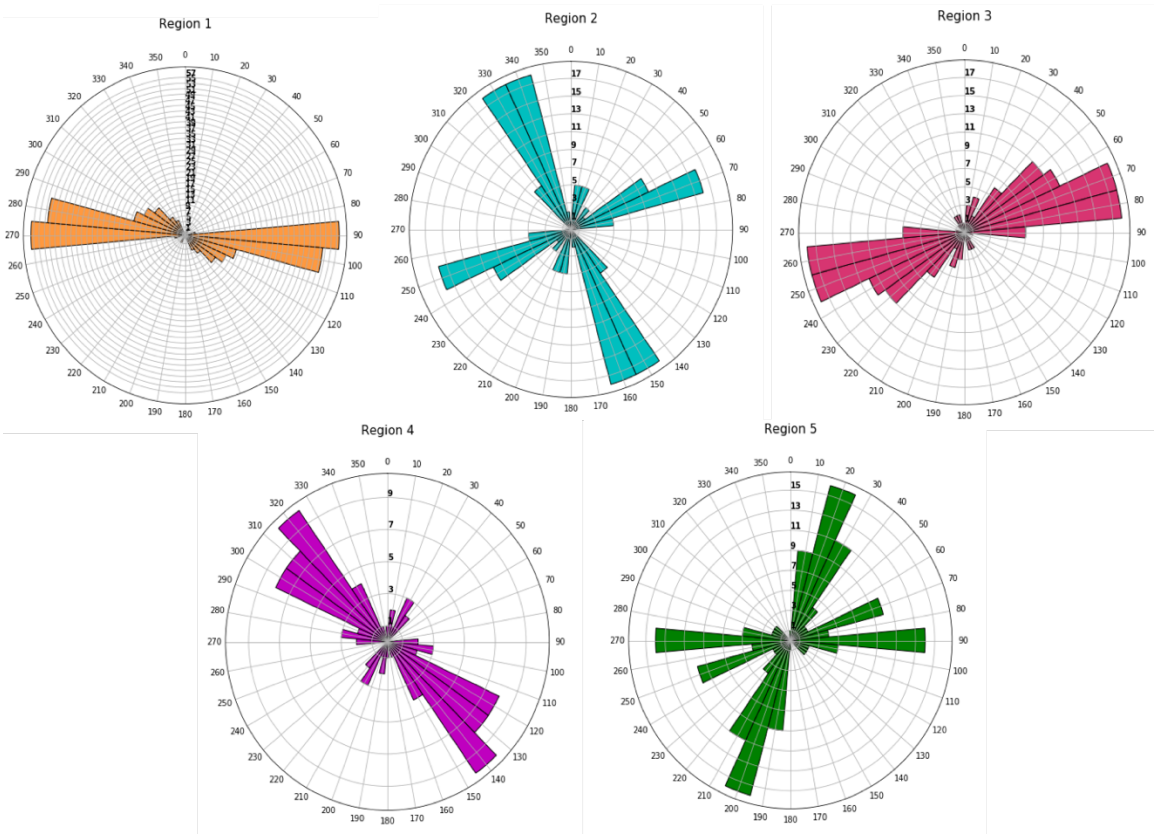

Fig 2.13. Rose diagrams showing the orientations of each tectonic feature mapped in the five regions. 0° represents North and 180° is South. Collectively, no preferred orientation appears for the features, although clustering is observed within Regions 1, 3, and 4. In Region 5, the features that have a direction pointing towards 20° are all a part of the Ithaca Chasma canyon system.

Future work will include investigating different stress mechanisms that are consistent with the observed lineations. One option could be tidal stresses because the stress field is non isotropic and could, thus, generate spatially and temporally variable orientations. However, Tethys' eccentricity is almost exactly zero, so a tidal origin would require these features to have formed in a past epoch of higher eccentricity or from a

different tidal stress source (e.g., obliquity, inward migration). For general patterns associated with these mechanisms, see Kattenhorn and Hurford (2009). The general distribution of these tectonics seems to be more consistent with extensional formation.

2.5. Conclusions

We have generated new maps and crater counts within well-imaged regions of Tethys, which can assist in impactor flux models for the Saturnian system. We are adding to the crater counts that have already been completed on Tethys to form a better understanding of the cratering history and the age of Tethys. Our regional mapping comprised five regions on Tethys: one near the Odysseus impact basin, three near the Ithaca Chasma canyon system, and one near the antipode of Odysseus. These regions were chosen due to their coverage by images with higher resolutions, which enabled us to resolve small-scale surface features. The regions are also located far enough away from each other so that we could test for any differences in impactor populations in our counts. The ages of the Saturnian satellites would provide critical constraints on the presence and longevity of oceans within the Saturnian moons as well as insight into how satellite systems form and evolve.

We counted a total of 3,975 craters between the five regions. We broke these craters down between the morphological classes of circular, elliptical, polygonal, irregular, and connected craters. We find that Regions 2, 3, and 5 have the highest total concentration of polygonal craters, which may be indicative of a high degree of subsurface fracturing near/in Ithaca Chasma than at other locations on Tethys. Region 1 has the highest total number of craters and linear features and highest proportion of simple circular craters. Based on our CSFD and R-plot analyses, our mapped regions are

generally the same age, but looking at the small differences at D < 3 km, Region 1 appears to be the oldest of our mapped terrains. Saturation may be occurring in some of our mapped terrain, but it depends on the cut-off chosen for the saturation equilibrium. This implies that our relative age estimates may be off, but the SFD and impactor population shapes are not affected by a change in saturation. Region 4 was chosen specifically to investigate terrain variations in an area antipodal to a large impact basin, which would theoretically experience the lowest density of small impacts. Our map of this region did not reveal any specific changes in terrain.

Our crater measurements indicate an enhancement of craters with diameters between 1 and 3 km at the anti-Saturn point (Region 1). This enhancement could be due to debris from the co-orbital satellites or from secondary craters where patterns from the parent crater have not been investigated. Previous work on secondaries from Odysseus (Ferguson et al., 2018) showed the contribution from the basin forming impact is minimal on our mapped areas. The formation mechanism of the observed crater chains is still an intriguing question that will require further analysis due to their irregular orientation patterns.

In regard to the tectonic features on the satellite, Regions 2 and 3 show fewer lineations than the other regions, which is surprising considering they are close to Ithaca Chasma. We expected that these close regions would have linear features that have similar orientations to the canyon system, but this trend was not observed. None of the regions have linear feature orientations that perfectly overlap with one another, which is suggestive of periods of non-isotropic stresses across the satellite.

While we observe what is likely a unique impactor population to the Saturn system, there are still questions remaining about the impact history of Tethys and the rest of the Saturn system. Some questions include

- What are the characteristics of the planetocentric impactor flux at the system and how does it vary across the satellites?
- How does secondary cratering from other large impacts onto Tethys affect the regional crater record?
- What influence do debris from impacts onto the co-orbital moons have on the surface record of Tethys?

Future analysis involving a combination of data analysis and dynamical modeling provides a starting point to answer these questions.

Similar to the other midsized moons of Saturn, Tethys is a world that is rife with a complex crater record and tectonic past that can be utilized to evaluate the age of the satellite and system. From the impact crater size frequency distributions on Tethys, we find that the majority of areas align with a planetocentric source population but does not entirely fit the established functions. We propose that in addition to the previously established production functions for craters in the outer solar system that a planetocentric distribution unique to the Saturn system is what primarily drives the cratering on Tethys.

2.6 Acknowledgments

The authors would like to acknowledge the support of a NASA Cassini Data Analysis Program (Grant NNX16AI42G) awarded to A. R Rhoden, a NASA Future Investigators in Earth and Space Sciences and Technology (FINESST) (Grant 80NSSC19K1532)

awarded to S. N. Ferguson and S. Desch, and Cassini Data Analysis Program (Grant NNX17AG01G) awarded to M.R. Kirchoff. Crater databases have been included as part of this manuscript. The authors would also like to thank Kelsi Singer, Luke Dones, and Bill Bottke for their comments on the data analysis. The authors would also like to thank Matija Ćuk, Caleb Fassett, and an anonymous reviewer for their reviews which greatly enhanced the manuscript. This research has made use of the USGS Integrated Software for Imagers and Spectrometers (ISIS3).

Data Availability Statement

Our crater counts in an excel file and final ArcMap files are available for public use on Figshare (Ferguson, 2020a; Ferguson, 2020b) DOI of https://doi.org/10.6084/m9.figshare.12509948.v1 and https://doi.org/10.6084/m9.figshare.12518390.

https://doi.org/10.1029/2008GL035402

2309. https://doi.org/10.1002/2013JE004477

CHAPTER 3

REGIONAL IMPACT CRATER MAPPING AND ANALYSIS ON SATURN'S MOON DIONE AND THE RELATION TO SOURCE IMPACTORS

Paper to be submitted to JGR Planets with co-authors Alyssa Rhoden and Michelle Kirchoff

Abstract

Recent dynamical modeling of the formation and evolution of the Saturnian satellites (Ćuk et al., 2016) has suggested that the ages of the inner moons (Mimas, Enceladus, Tethys, Dione, and Rhea could be as young as 100 Myr. This estimate is in contrast to previous models that have suggested an age that is more contemporaneous with the formation of Saturn 4.5 Gyr ago. We examine the impact craters of Dione using imagery from NASA's *Cassini* ISS camera to analyze their size-frequency distributions (SFDs) and age relations. We surveyed four areas across different geologic terrains as defined by Kirchoff & Schenk (2015) and compared our crater counts to the production functions described by Zahnle et al., 2003. In addition to crater counts, we study different crater morphologies to further examine the bombardment source for the craters. We find evidence for a Saturn-specific planetocentric impactor source, as neither Zahnle et al., (2003) production function fully fits the data. We compare our Dione data with our previous work on Tethys (Ferguson et al., 2020) and find similarly sloped SFDs between the satellites, but Dione's surface has been extensively modified at smaller crater sizes (D ~< 5km) and has been impacted by larger impactors, creating more large craters (D ~> 20 km) on Dione than Tethys. In contrast, Tethys represents an ancient un-modified surface within the Saturn system. Further study and data are needed for the satellites of Uranus

and Neptune's moon Triton to fully constrain the bombardment history of the Saturn system.

Plain Language Summary

Following the conclusion of NASA's *Cassini* mission, a major unresolved question is how old are the inner moons (Mimas, Enceladus, Tethys, Dione, Rhea) of Saturn? Studies that have formed the moons and changed their orbits around Saturn over time have suggested that these moons may be as young as 100 million years old. This is in contrast to previous work that inferred these moons formed at a the same time as Saturn (age ~ 4.5 billion years), or later in Saturn's history but still long ago (ages between 4 and 1 billion years). Narrowing down the ages of these satellites has implications for how groups of moons form around planets and how they can change over time. To examine the age relationships, we counted the number of impact craters on Saturn's moon Dione over four different areas of the surface, to determine what sources of debris within the Solar System could have made these craters. A higher number of craters would indicate an older surface, whereas a low number of craters would indicate a younger surface. Lower crater numbers could also be attributed to other geologic processes such as volcanism changing the surface and erasing the craters. We counted a total of 3,897 craters in four separate areas across Dione's surface. We analyzed their size distributions on the surface and compared them to previous predictions for what a surface in the outer solar system could look like when bombarded with Sun-orbiting material. Our comparison showed that the Dione data did not match previous predictions, which we interpreted to show that a Saturn-orbiting source of debris is creating the craters on the surface. All four mapped areas are similar in age and are likely quite old. Additional

studies examining the change over time of a Saturn-orbiting source of debris are needed to confidently assert an age. We find that the surfaces of Tethys and Dione have similar distributions of craters on their surfaces, but that previously active processes on Dione have erased a fraction of these smaller craters, causing a difference between the two moons. Tethys then is an example of an old surface that hasn't seen as much activity as Dione. Saturn currently appears to host a unique cratering record, but by obtaining more data from the moons of Uranus and Neptune we could more accurately determine the ages of Saturn's moons.

3.1. Introduction

How old are Saturn's mid-sized icy moons, and how did the Saturn system itself form and evolve? Even with the wealth of data delivered by the *Cassini* mission, these critical questions remain unanswered. Dynamical models by Ćuk et al., 2016 suggested that the inner satellites (Mimas, Enceladus, Tethys, Dione, and Rhea) could be as young as 100 Myr, whereas other models describing the moons formation out of either the proto-Saturn disk or Saturn's rings (see formation discussions in Chapters 1 and 2) place a formation age of the satellites closer to 4.5 Gyr. Saturn's rings could also provide a clue to the ages of the satellite system if its age is better known. Measurements from the Cassini Grand Finale mission found the mass of the rings to be $1.54 \pm 0.49 \times 10^{19}$ kg (Iess et al., 2019). Even with this unprecedented constraint on the rings' mass, there still is debate in the community whether this indicates a young age for the ring (100 Myr) or an older age (4.5 Gyr) (Crida et al., 2019). With this wide age range of 100 Myr to 4.5 Gyr for both the rings and the satellites, ground-truth data, in the form of *in situ*

observations of the surfaces of these satellites, is critical for placing further limits on ages.

Impact cratering analysis is one avenue for constraining the ages of these satellites. Comparisons of impact crater distributions to the corresponding production functions for that area of the Solar System allow for a more direct examination of what created these impact craters and when (Neukum et al., 2001; Dones et al., 2009). Age dating based on craters has been successful in the inner solar system, especially thanks to radiometric dating of the returned samples from the Apollo and Luna missions (Neukum et al., 2001). Returned samples and a well-described impactor population from ground-based observations have helped to refine the knowledge of the source impactor size-frequency distribution (SFD). The impactor SFDs have then been taken and translated to a cratering rate, which is then used to obtain the surface age of the area of interest (Neukum et al., 2001, Hiesinger et al., 2012; Hartmann 2005; Zahnle et al., 2003; Dones et al., 2009).

For the outer planets, the knowledge of the size-frequency distributions of heliocentric (Sun-orbiting) impactors is more limited due to the difficulties in obtaining high-resolution observations. Additionally, at Saturn and possibly Neptune a planetocentric impactor source may also be responsible for a significant number of craters on the satellites of these planets. However, placing constraints on the dynamical evolution of a planetocentric source is challenging due to the transient and local nature of this source. Analysis of the impact craters observed in the imaging data from *Voyager 2* (Smith et al., 1981, 1982; Shoemaker & Wolfe 1981; Plecia & Boyce 1982; Horedt & Neukum 1984a; Chapman & McKinnon 1986) revealed Saturnian moons with two likely

sources of impactors, which the authors termed Population I and Population II. Population I, which was shown to have a SFD with a shallower slope and an abundance of craters larger than 20 km, is likely dominant on Rhea, and is similar to the course of craters on Jupiter's Galilean satellites (Smith et al., 1981, 1982; Shoemaker & Wolfe 1981; Plecia & Boyce 1982; Horedt & Neukum 1984a; Chapman & McKinnon 1986). Population II has an abundance of smaller craters (D < 20 km) and was observed to contribute to craters on the remaining inner satellites of Saturn (Mimas, Enceladus, Tethys, and Dione).

Prior to the arrival of *Cassini* to the Saturn system, Zahnle et al., 2003 described two major production functions that were predicted to be the dominant source of craters on the satellites. Case A was based off crater counts on Europa and Ganymede and the current cometary impactor rates (Zahnle et al., 2003). Case B was then based off crater counts on Triton and a further evolved cometary impactor flux. Both production functions assumed a heliocentric source for these craters rather than a planetocentric source (Zahnle et al., 2003), although the need for a Case B implies that either the cometary flux changes with distance from the Sun or there is a planetocentric source adding small craters.

Examination of the source regions for the craters in the outer reaches of the Solar System requires modeling of how these populations evolved over time due to giant planet migration and later interactions with resonances (Di Sisto & Brunini, 2007; Tiscareno & Malhotra, 2003; Volk & Malhotra, 2008). This modeling provides a base to then examine how these source regions have evolved over time. One such source is the population of

Centaur objects where studies have shown them to cause shallow sloped size-frequency distributions on the satellites of Jupiter (Di Sisto & Zanardi, 2013, 2016; Zahnle et al., 2003) and a steeper slope on Triton. For the Saturnian satellites in particular, the slopes of the size-frequency distributions from Centaurs appear to lie in between the distributions seen for Jupiter and Triton (Di Sisto & Zanardi, 2013, 2016). Studies of other outer planet satellite systems showed that Jupiter as well as Pluto & Charon tend to match well with the Case A scenario rather than Case B showing a shallower sloped distribution (Singer et al., 2019).

During the Cassini mission, studies of the cratering records on the inner satellites revealed complex surfaces with variations across each satellite (Dones et al., 2009; Kirchoff & Schenk 2010, 2015; Hirata 2016; Kirchoff et al., 2018). Our previous work on Tethys (Ferguson et al., 2020), further suggested that planetocentric debris unique to Saturn is the dominant source of the craters on the surface and that previously described production functions don't fully capture the impactor size frequency distributions within the Saturn system. To further examine how the crater record varies at each satellite, we now turn our focus from Tethys to Dione.

Dione (r = 560 km, ρ =1.47 g/cm^3) has a combination of older, cratered terrain and younger regions, indicated by the bright ice on the wispy terrain on the trailing hemisphere (Beddingfield et al., 2015). It may currently have an ocean underneath its ice shell (Beuthe et al., 2016; Zannoni et al., 2016), pushing the total number of ocean worlds orbiting Saturn to 3 . Encealdus' South Polar Terrain showed evidence for a liquid water reservoir (Spencer et al., 2006), which was then confirmed to be tied to a global ocean

(Thomas et al., 2016) instead of a regional sea due to Cassini gravity measurements. Dione's ocean was inferred based on observations of its gravity field (Hemingway et al., 2016). Dione's surface has likely experienced several periods of active resurfacing (Kirchoff & Schenk 2015) followed by periods of extensional tectonic deformation, which are more concentrated on the trailing hemisphere (Collins et al., 2009). Contractional deformation is also observed on the surface, but to a much lower extent than the extensional features (Collins et al., 2009). Larger craters on Dione have the appearance of having undergone viscous relaxation, which may indicate a higher heat flux in the more recent history (~ 1 Gyr) of Dione as well (Phillips et al., 2012; Hammond et al., 2013 White et al., 2017).

Located with the wispy terrain on the trailing hemisphere is a region of ice that appears darkened in comparison to the rest of the satellite. Darkening of the ice is likely due to bombardment of particles from Saturn's magnetosphere interacting with the ice already present on the surface (Clark et al., 2008). Wispy terrain in this area cross-cuts the areas of particle bombardment (Stephan et al., 2010) also indicating that the wispy terrain unit is likely younger than the surrounding terrain since the wispy terrain still shows a bright appearance and few other features crosscut the tectonics (Martin & Pathoff 2018). Absolute age measurements for the region of dark ice islimited, but recent studies of surface ages using the ratios of amorphous to crystalline water ice on Dione have suggested that the more densely cratered terrain on Dione is approximately 2 Gyr in

age (Rivera-Valentiń et al., 2020) and other areas on the trailing hemisphere could be as old as 1.4 Gyr (López-Oquendo et al., 2019).

Here we catalogue craters in additional regions on Dione to complement previous mapping studies by Kirchoff & Schenk 2010; 2015 and build a more complete size-frequency distribution for the craters on the surface. We've completed crater counts across four distinct regions on the surface varying across geologic unit and location. In addition to the circular craters that are reported, we've mapped other crater morphologies such as polygonal and elliptical craters. Polygonal craters in particular have been documented across Dione (Beddingfield et al., 2016) and are of use when examining the extent of previous periods of fracturing in the ice shell. Elliptical craters are also useful for examining the source of the craters as they often record the direction of impact due to their oblique nature (Bottke et al., 2000; Elbeshausen et al., 2013; Gault & Wedekind, 1978; Melosh, 1989; Schultz & Gault, 1990). Here, we note trends in elliptical crater orientations on a regional scale and the overall prevalence/distribution of mapped polygonal craters.

We investigate how the surface units on Dione affect the observed size-frequency distributions of craters on the surface and the most likely dominant impactor source on Dione. Additionally, we evaluate how much the crater SFD's change with increasing distance from Saturn by comparing our regional crater counts for Dione to our previously published work on Tethys (Ferguson et al., 2020). We aim to provide additional

measurements of the crater SFD on Dione's surface to further constrain the dominant impact source in the Saturn system and the characteristics of that population.

3.2. Methods

Following the image processing techniques of Ferguson et al., 2020 we mosaicked Cassini ISS images (Porco et al., 2004) together for areas of overlapping interest. Images were first located using the USGS PILOT website (Bailen et al., 2013, https://pilot.wr.usgs.gov/). This process included ingestion into the USGS Integrated Software for Imagers and Spectrometers (ISIS3, Anderson et al., 2004); the camera pointing information is attached to the images and the images are calibrated to the camera model. After initial image processing, the images are tied together using the *findimageoverlaps* command and an initial control net is generated to aid in the refinement of the position of the images when they are overlain on one another. Cnet is used to refine the control net such that the images are aligned with less offset than if they were just mosaicked after the map projection. This process of using the control net allows for the reduction in the appearance of seams in the mosaic, which can aid in the identification and measurement of crater shapes for craters that are located along the image boundaries. Figure 3.1 shows the location of all four mapped areas on Dione. These areas were chosen due to their pixel scales and lighting conditions. Image names, resolutions, incidence angles, and central coordinates are shown in Table 3.1.

Table 3.1. Images used in this study and their characteristics

Image	Resolution (m/pix)	Center lat/lon (°)	Incidence Angle (°)	Phase Angle (°)	Mosaic Area (km^2)
Region 1					
N1665974517_1	225.35	37.25 N 237.34 E	57.01	57.52	182,696
N1665974689_1	229.21	15.70 N 245.65 E	60.91	56.01	
N1665974861_1	234.02	8.83 S 252.62 E	70.25	54.55	
Region 2*					
N1649313734_1	122.51	35.15 S 11.31 E	47.19	8.47	118,911
N1649314237_1	147.59	25.34 S 13.01 E	41.83	9.07	
N1649314777_1	174.64	9.82 S 14.74	36.14	9.56	
N1649315242_1	198.29	7.789 N 17.64 E	37.3	9.92	
Region 3					
N1662200149_1	239.24	6.63 N 105.81 E	63.01	71.59	138437
N1662199979_1	237.03	29.42 N 108.14 E	62.28	73.79	
Region 4					
N1507742440_2	194.2	28.32 N 167.75 E	48.91	21.53	84307
N1507742601_2	184.86	9.35 N 172.11 E	29.55	21.68	

Once the images are controlled, they are map projected in an equirectangular/simple cylindrical projection. Resulting mosaics were brought into ArcGIS and overlaid on the global mosaic generated by Roastch et al., 2008. While the average pixel scale of the base map is 154 m/pix, in order to make a global mosaic, the various input images would have had to be upscaled or descaled to enforce a unified resolution across the mosaic. Our approach of using the single images and mosaicking them retains their resolutions by not forcing the images to match a global standard. In instances where the mapped areas are above 30° N/S the resulting mosaic is then reprojected in ArcGIS to ensure accurate measurement of the crater diameters. We

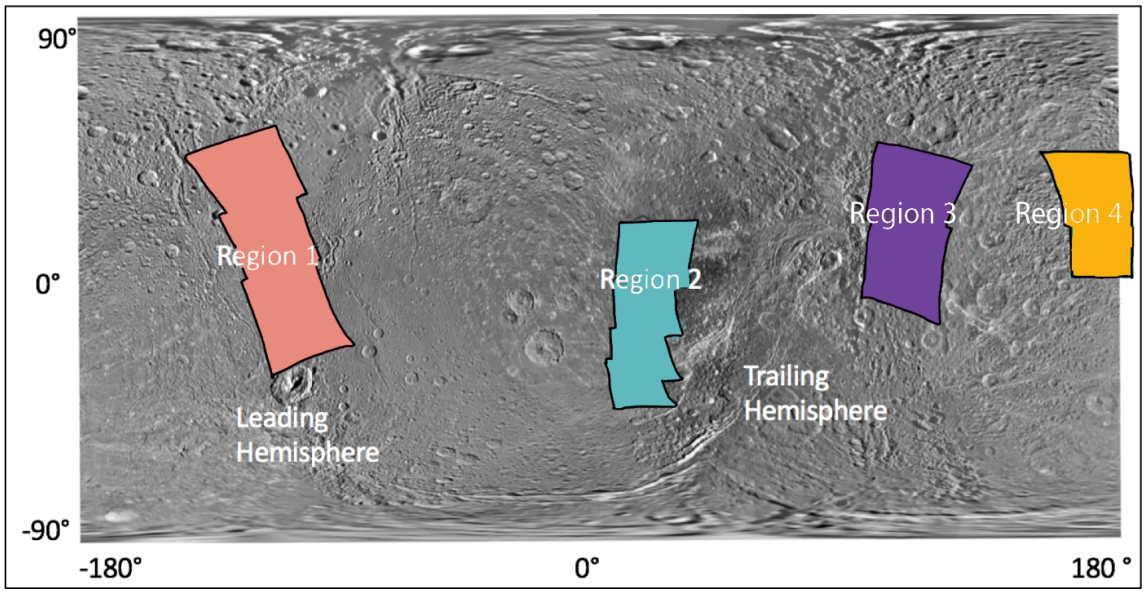

Figure 3.1. Locator map for the four regions surveyed in this study. Basemap from Roatsch et al., 2008

utilized the CraterHelper tools extension for ArcGIS (Nava 2010) and the Graphics and Shapes toolkit (Genneses 2011) to measure the sizes of the craters. Both toolkits measure the crater in 3D space, which helps reduce the bias in size measurements that can occur within craters due to the image projection.

For a crater to be mapped as such we require the feature to be at least 5 pixels across (Robbins et al., 2014, 2018; Fassett 2016); using the average image resolution of 198.1 m/pix leads to a minimally identifiable crater size of D~994 m. Candidate craters would also need to display negative relief as shown by the shadowing/lighting conditions, be roughly circular, and when possible show an observable crater rim. Our criteria for the minimum pixel size allows for more confident identification of craters. Craters smaller than that are however included for the sake of completeness in the counts. When size-frequency diagrams are created, we cut-off the craters around the 7 pixel range (~1.39 km) as a more conservative size limitation due to the resolution of the

images. Additional crater morphologies were mapped such as polygonal craters and elliptical craters.

Polygonal craters were mapped as they can indicate the presence of fracturing within the subsurface (Shoemaker et al., 1963, Öhman et al., 2010; Beddingfield et al., 2016) and have been shown to have a strong presence on the surface of Dione (Beddingfield et al., 2016). These craters have at least one straight rim segment and have formed from jointing that occurred in the underlying faults (Ohman et al., 2008) and have been surveyed on many types of surfaces across the Solar System. Following convention we mapped these craters as polygonal if there was more than one straight rim segment that connected with another rim segment to form a polygonal wall shape.

In the case of elliptical craters, they are often formed during a low angle impact and at slower impact velocities (Gault & Wedekind 1978; Bottke et al., 2000; Collins et al., 2011; Elbeshausen et al., 2013). We mapped elliptical craters and measured their major and minor axes; we then computed the ellipticity of the crater by taking the ratio of the major axis to the minor axis. In the final database, craters were labeled as elliptical if they had an ellipticity value greater than 1.2. Previous studies have used an ellipticity value of 1.1 as a cut off (Bottke et al., 2000), but we have chosen a higher value to fully capture the elliptical nature of the crater.

We utilize the cumulative size frequency distribution (CSFD) and the relative (R) plots as described by the Crater Analysis and Techniques Working Group (CATWG, 1979). CSFDs are generated by first sorting the data in descending order, which builds a sequence of diameters. Then on a loglog plot, “plot the diameter of each crater against the cumulative number of craters per unit area with equal or larger diameters (N/ surface

area) (CATW, 1979).” This produces the Y axis which normalizes the counts to obtain the total number of craters per unit area. Standard Poisson's errors are computed by taking the square root of the Nth crater in the sequence divided by the surface area. CSFDs are useful for looking at the broader trends in the dataset, but they tend to minimize smaller variations in the data. For our purposes, the CSFDs are particularly useful to examine variations in the impact cratering production functions that have been proposed for the outer planets (Zahnle et al., 2003).

We utilize the R-plot as the binned nature of these plots better highlights the variations in the data and can be more useful for analyzing changes in the impactor source by allowing for a closer look inflection points that may have been observed on a CSFD. Construction of the R-plot requires the data be binned in $\sqrt{2}$ increments of diameter starting from 1 km. From there, the R-value is calculated using equation 3.1.

$$R = \frac{\overline{D}^3 N}{A(D_a - D_b)} \qquad \textbf{Eq 3.1.}$$

$\overline{D}$ is the geometric mean of the diameters in the bin, D_a and D_b are the minimum and maximum values in that particular bin, N is the total number of craters in the bin, and A is the count area. Errors for the R-plots are calculated as $\frac{\sqrt{R}}{A}$. All plots shown are plotted in log-log space. If a crater curve appears higher on the plot, then that is indicative of an older relative surface age when compared to the other mapped terrain types. Should the mapped areas overlap in their positions on the R and CSFD, then their ages are relatively similar (within error). Poisson errors used here are just the statistical error and don't include uncertainties that are inherent in crater counting (Robbins et al., 2014, 2018)

3.3. Results

Figures 2-5 show the unmapped mosaic (a) and the mapped mosaic (b) for easy comparison between images. Additionally, for ease in comparison across regions, Table 2 breaks down the crater counts into 1 km diameter bins per region and Table 3 shows the combined counts of each mapped morphology by region. Individual points on each map are representative of craters whose diameters are between 1-2 km. They were singled out so that variations in that size range could be analyzed.

Figure 3.2 shows Region 1, which is located on the leading hemisphere and is distinguished by the large crater Lagus in the bottom panel. Following the geologic units of Kirchoff & Schenk 2015, this area lies within their mapped "Smooth Terrain" unit, which is defined as a high density of craters D <= 15 km and a low density of craters larger than 30 km (Kirchoff & Schenk 2015). Between these two diameters, the slopes of the SFD's are steeper than what is observed in other areas of their counts (Kirchoff & Schenk 2015). Our counting of this area shows 1280 total craters, followed by a morphology breakdown of 1182 circular craters, 87 elliptical craters, 11 polygonal craters, and 0 irregular craters. Across Region 1, the majority of craters lie within the circular taxonomic class, although we note the concentration of polygonal craters in the upper panel of the image. These polygonal craters are also found near some larger tectonic features that are present within the scene. Unlike the rest of the mapped areas, we did not classify any of these craters as irregularly shaped. There are a couple which may appear more irregular than others, but we classified them as elliptical and circular

respectively since their shapes predominately appeared to be more consistent with those classifications.

Figure 3.3 shows Region 2 which is located close to Dione's trailing hemisphere,

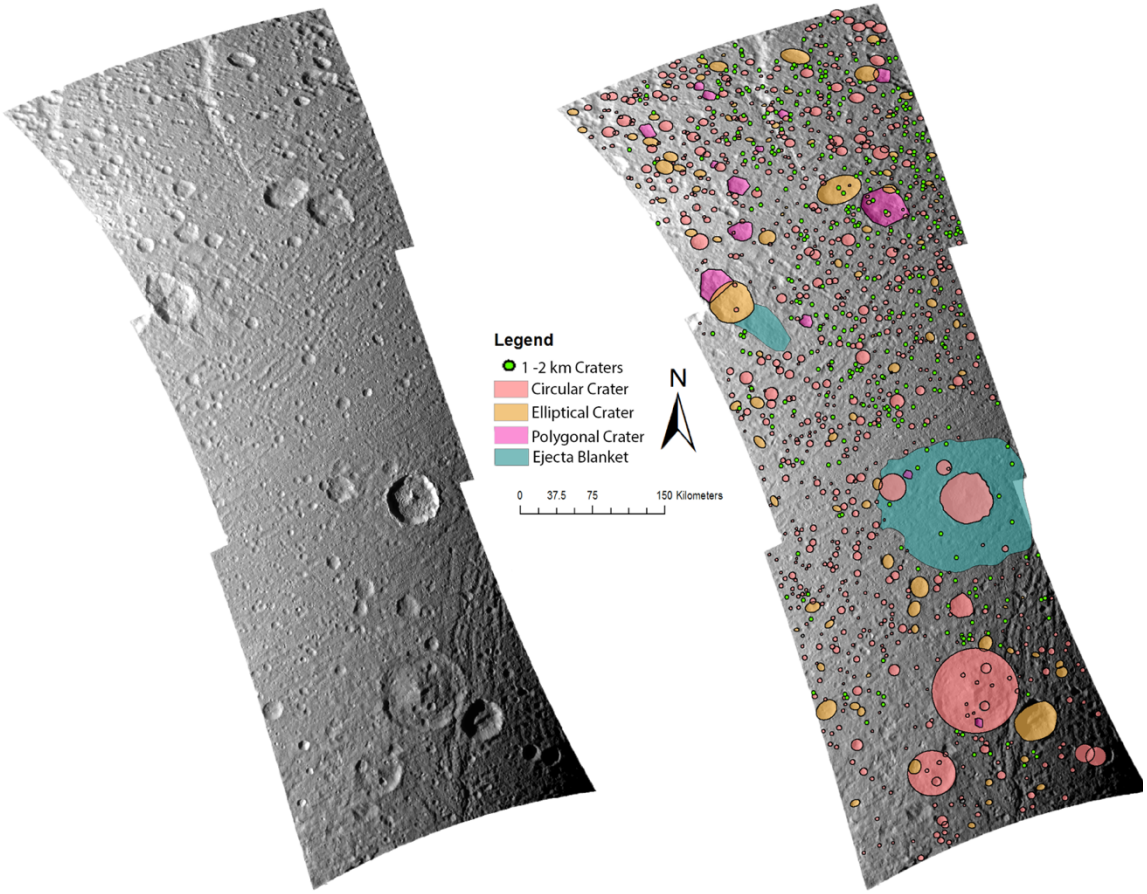

Figure 3.2. Unmapped (a) and mapped (b) mosaic for Region 1. This is the sole region mapped on the leading hemisphere. When visible, ejecta blankets of larger craters were mapped (based on a softened appearance of the terrain). Each color corresponds to a morphology type and craters with diameters between 1-2 km are shown as points due to the scale.

within the "Intermediate Cratered Terrain (ICT)" unit defined by Kirchoff & Schenk 2015. The ICT unit has a lower crater density than their oldest mapped units, but still has a higher crater density than the remaining units. ICT, as mapped, covers the majority of the sub and anti-Saturnian hemispheres (Kirchoff & Schenk 2015). We mapped 910 total

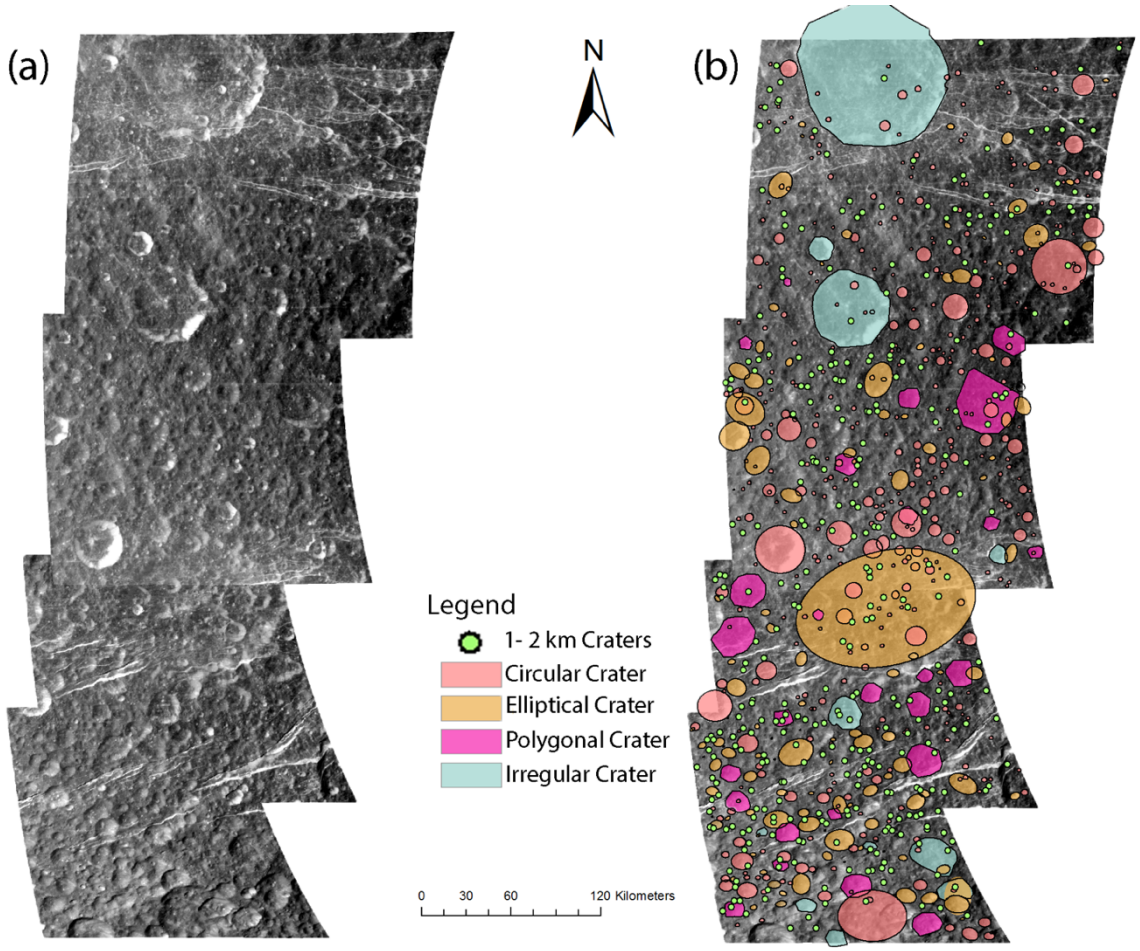

Figure 3.3. Unmapped (a) and mapped (b) mosaics for Region 2. This location was chosen due to its proximity to an edge of the wispy terrain. This area also has a higher percentage of polygonal craters located within its boundaries.

craters, which break down taxonomically into 776 circular, 97 elliptical, 26 polygonal, and 11 irregular. Region 2 is unique in that it is just bordering an edge of the wispy terrain tectonic system, which may have an influence on the final crater counts.

Figure 3.4 shows Region 3, which is located on the trailing hemisphere and the eastern side of the wispy terrain. Following the unit boundaries within Kirchoff & Schenk 2015, this area lies within their "Faulted Terrain (FT)" unit. This unit encompasses the Wispy Terrain and has a lower density of craters D ≤ 45 km when compared to the ICT, but their densities in D ≥45 km are similar. Within this area we find 849 total craters: 684

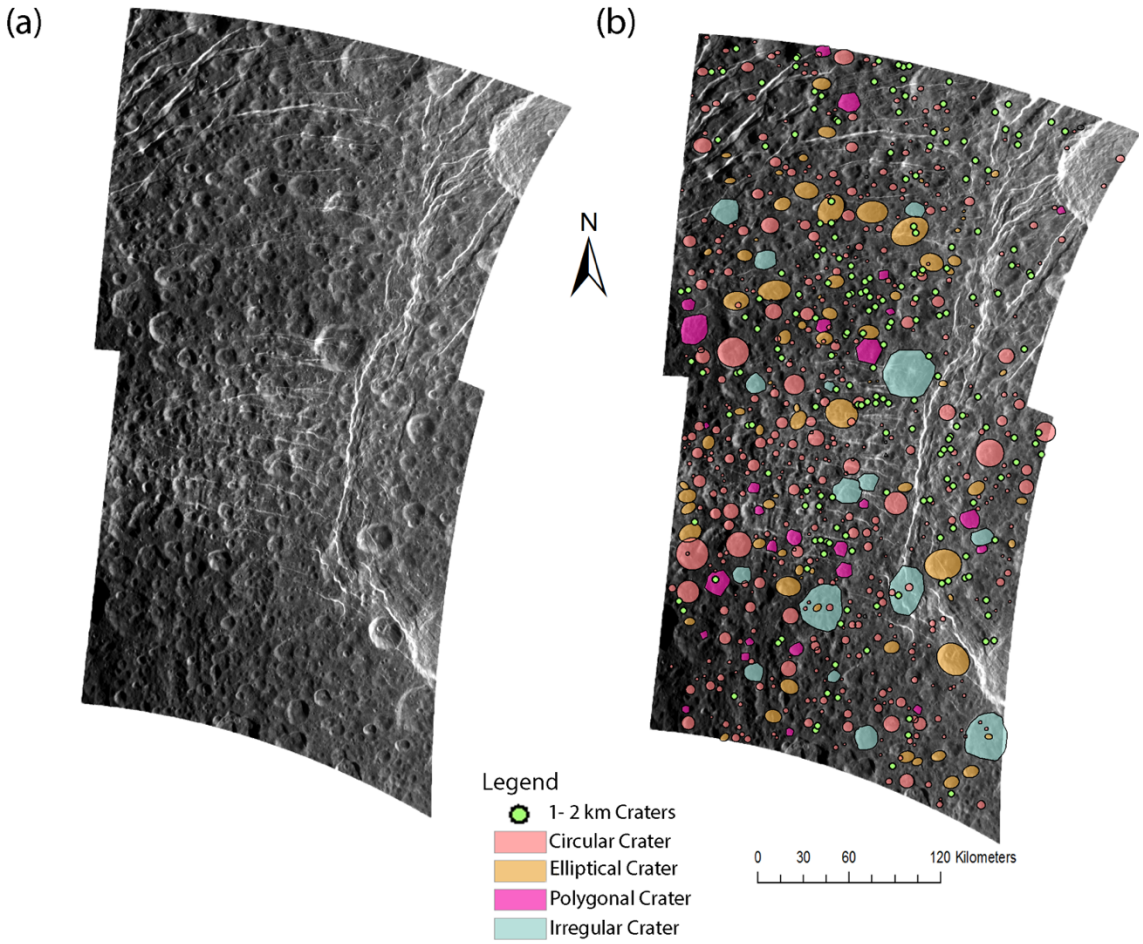

Figure 3.4. Unmapped (a) and mapped (b) mosaics for Region 3. This area is located on the opposing edge of the wispy terrain from Region 2. Similarly seen in Region 2, a higher fraction of polygonal craters are observed here than in Regions 1 and 4.

circular, 123 elliptical, 26 polygonal, and 16 irregular craters. Similarly to Region 2, which also bounds the Wispy Terrain, we find a high concentration of polygonal craters, which highlights their relationship to underlying and observed surface fractures. Elliptical craters in this area are oriented in an east/west direction (Figure 3.7).

Figure 3.5 shows Region 4, also located on the trailing hemisphere and within the ICT unit defined by Kirchoff & Schenk 2015. We count 858 total craters with 703 circular, 117 elliptical, 17 polygonal, and 14 irregular craters. From the polygonal craters we observed, the influence of tectonics on this area appears to be less than in Regions 2

& 3 where we observe a higher number of polygonal craters (see Table 3.3). This inference is supported by a visual inspection of Region 4 which reveals far fewer tectonic features.

From the raw crater counts, we built the cumulative size-frequency distributions

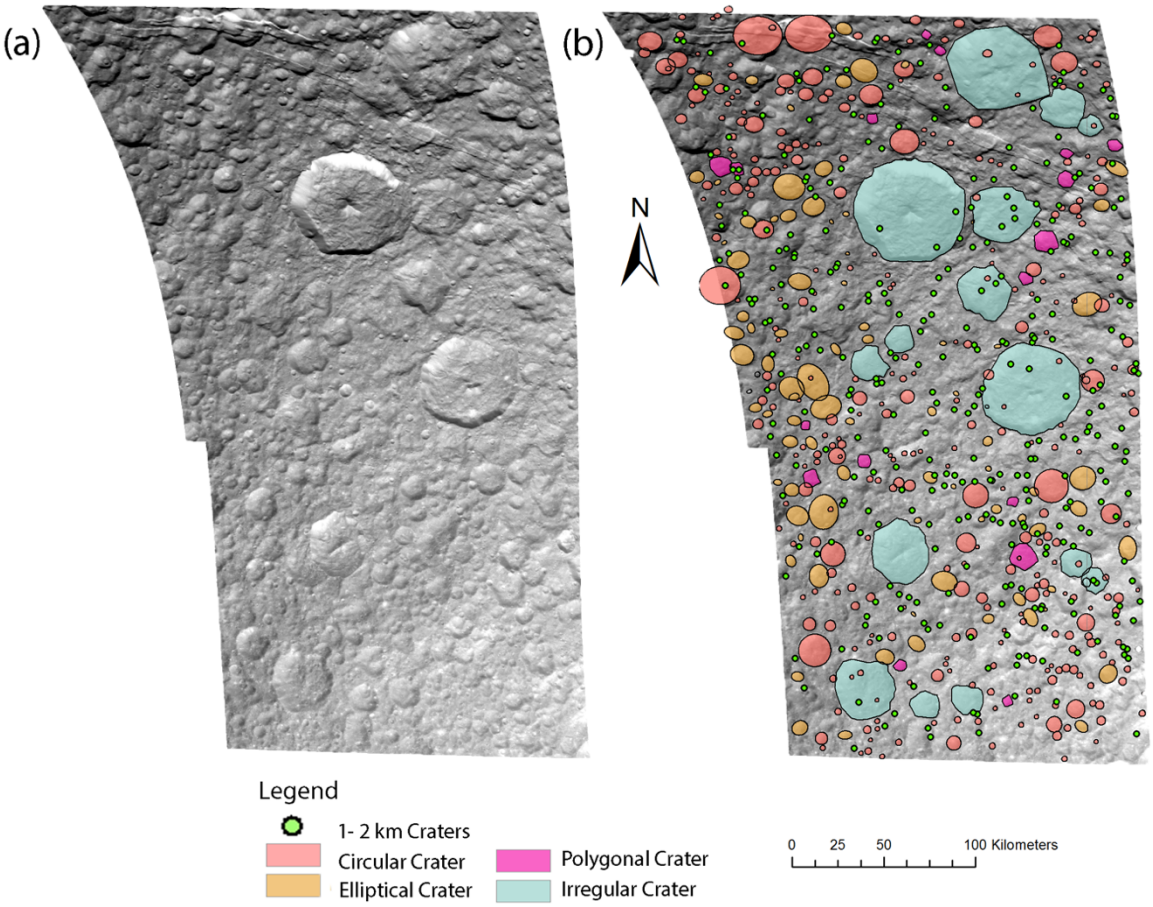

Figure 3.5. Unmapped (a) and mapped (b) mosaics for Region 4. This area is located on the edge of the trailing hemisphere and is best characterized for the higher number of irregular shaped large craters.

(CSFDs) and R-plots for the surveyed areas (Figure 3.6). Based on the CSFD's we find that the crater counts are complete down to 1.2 km where the roll off is observed on the plot in Figure 3.6a. Craters larger than 20 km are observed more frequently in these areas than on Tethys (Ferguson et al., 2020). This is likely due to larger counting areas, which allowed for more larger craters to be fully contained within an image/mosaic. Total

amounts of these larger craters isn't high, so there still may be a dearth of these larger craters across the satellites, similar to what was observed in Kirchoff & Schenk 2010.

In the diameter range of ~ 1-5 km, the cumulative slopes are quite shallow (~ -2 slope, flat R values in figure 3.6c), suggesting a mechanism of removing craters from that size range in order to make the curve shallow. Regions 1 and 4 have very similar distributions between 2 and 4 km. For craters between 5 and 10 km, a divergence between Region 1 and the other three regions becomes more apparent as the slope for Region 1 becomes steeper, showing a decrease in the cumulative number of craters in that size range per unit area. Regions 2-4, on the other hand, have similar slopes and show little variation in this size range. Craters with diameters between 10 and 20 km in Region 1 continue to show a steeper slope relative to the other three mapped areas. However, there are small breaks in the slope for D ~ 13 km and D ~ 15 km. Regions 2-4 also show a break in slope for D ~ 15 km and their slopes gradually start to steepen as well. For D > 20 km, Region 1 has breaks in its slope around D ~ 22 km and again for D ~ 30 km. Region 3's slope increases dramatically between 20 and 30 km, showing a marked drop off in comparison to the other three areas. Again, there's a break in the slope for Region 3 at D ~ 30 km and then the slope steepens again at D ~ 40 km. Region 4 steepens with Region 3 until it breaks off and has a shallower slope at D ~ 25 km. Between Regions 2, 3, and 4, Region 2 has the shallower slope at these larger diameters as well. These differences in slope across the regions imply that they have been inconsistently affected by larger craters, although small number statistics may also play a role.

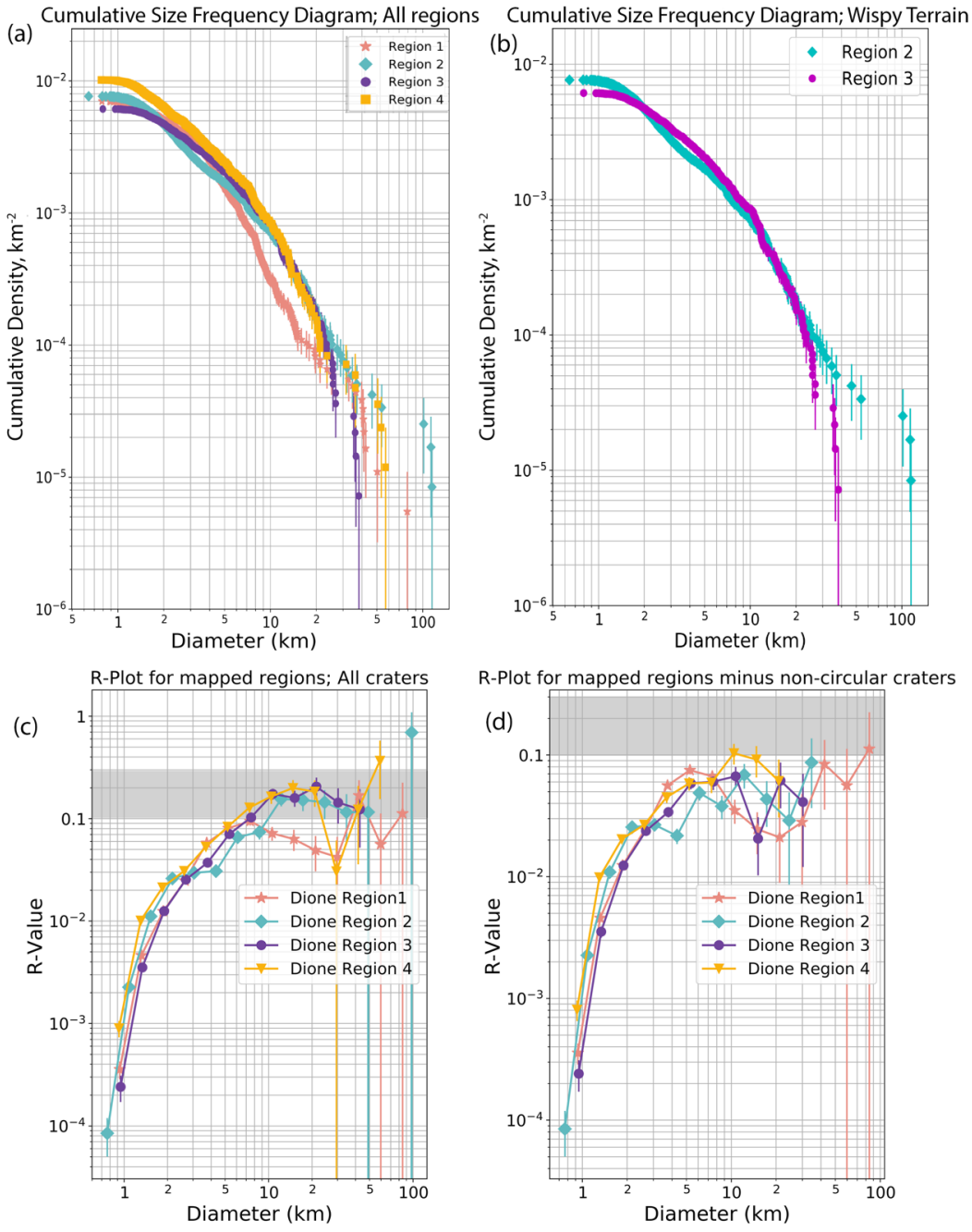

Figure 3.6. Size-frequency distributions for the mapped terrain. (a) Cumulative size-frequency diagram for all four regions. All mapped areas plot relatively close to one another, indicating a similar relative age. (b) Cumulative size-frequency diagram for the two regions with close proximity to the wispy terrain. Shallower slopes at the small diameters indicate the influence of resurfacing on the crater distributions. (c) R-plot of mapped terrain, inclusive of all crater morphologies. (d) R-Plot of mapped terrain, solely based on the circular crater morphology. Grey bar in (c) and (d) is representative of the crater equilibrium mark (see section 3.4 for more details). Regions reach the crater equilibrium point at different diameters depending on which morphologies are included.

Figure 3.6b illustrates the differences between two edges of the wispy terrain unit. Region 3 has a shallower slope between D ~ 1.5 - 2.5 km, which shows an overall lower crater density in this small size range. This lower density could be caused by previously active resurfacing processes that may have affected Region 3. However, Region 2 has a consistently lower crater density for D ~ 2 – 10 km. From ~ 10 km – 20 km, the two areas have extremely similar slopes, but diverge once more at D > 20 km where their slopes deviate significantly.

Table 3. Crater Morphologies for Each Mapped Area

Morphology	Region 1	Region 2	Region 3	Region 4	Total
Circular	1182	776	684	703	3345
Elliptical	87	97	123	117	424
Irregular	0	11	16	14	41
Polygonal	11	26	26	17	80
Secondaries	0	0	0	7	7
Total	1280	910	849	858	3897

We report the regional crater counts, broken down by crater sizes, spaced in 1 km bins, in Table 3.2. Crater counts are then further broken down by morphology in Table 3.

Table 3.2: Crater counts in 1 km Diameter Bins Between all four mapped areas and their totals

Diameter	Region 1	Region 2	Region 3	Region 4	Total
0-1	9	16	2	16	43
1-2	350	336	191	307	1184
2-3	252	230	191	168	841
3-4	211	86	107	106	510
4-5	170	40	75	56	341
5-6	79	38	54	42	213
6-7	62	24	43	26	155
7-8	36	30	34	35	135
8-9	38	13	23	21	95
9-10	16	10	12	10	48
10-15	34	49	71	43	197
15-20	9	18	23	15	65
20-50	12	16	23	10	61
50+	2	4	0	3	9
Total	**1280**	**910**	**849**	**858**	**3897**

The majority of our mapped craters fall within 1-5 km where they comprise 74% of the total counts. Table 3 further illustrates the

prevalence of polygonal craters being located near more of the tectonically active surface; 65% of the mapped polygonal craters were located in the regions closest to the wispy terrains. Elliptical craters were observed across the satellite and with seemingly no preference for one hemisphere over another. Elliptical craters also comprise a small portion of the overall mapped morphologies with 10.8% of all craters counted being classified as elliptical. Figure 3.7 shows the orientations of mapped elliptical craters overplotted on one another. North is measured as 0° and a North/South oriented crater would plot vertically on the rose diagram. We do observe a trend in the East/West direction for the elliptical craters, but there is a variation across the possible orientation ranges.

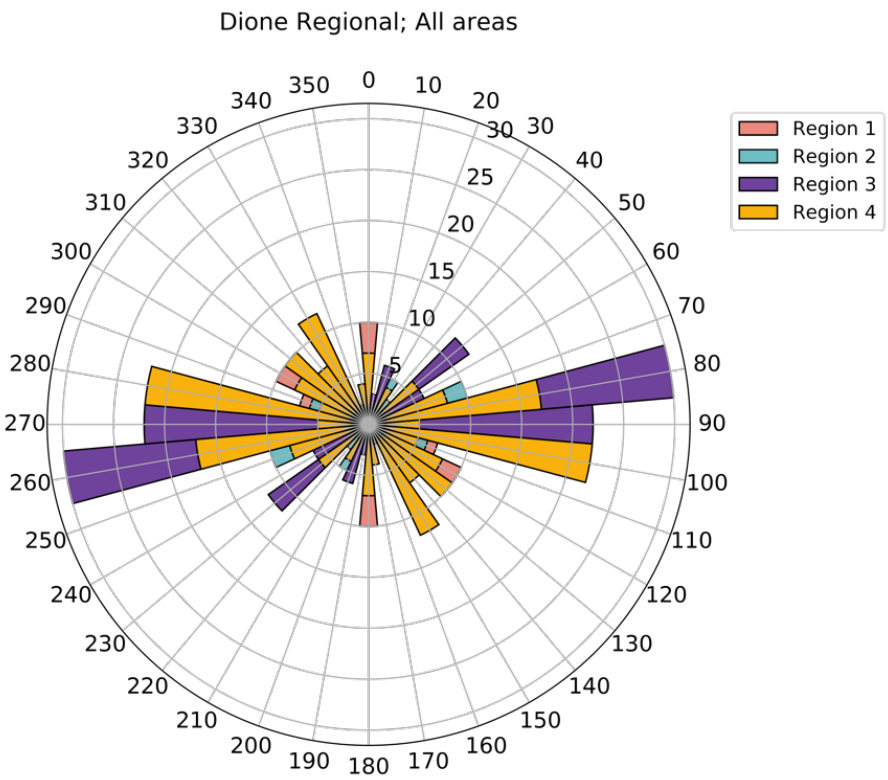

Figure 3.7. Rose diagram for all mapped elliptical craters on Dione. We observe a slight preferential orientation in the East/West direction.

3.4. Discussion

Age relationships for the four mapped areas are fairly straightforward in that no one region appears drastically older or younger than another. This likely means that while the surface

ages may differ within error, these surfaces were modified along similar geologic timescales. The SFD's show overall shallow-sloped distributions for the craters between ~1- 5 km, which we interpret to be representative of the surface having undergone some resurfacing process. A comparison between our mapped regions and the unit boundaries defined by Kirchoff & Schenk 2015 show that Region 1 is in their "Smooth Terrain(ST) ", Regions 2 and 4 are in the "Intermediate Cratered Terrain (ICT) " and Region 3 is located within the "Faulted Terrain (FT)". Kirchoff & Schenk 2015 observed a decrease in densities for craters at D $\lesssim$ 15 km and increased densities of craters at D $\gtrsim$ 50 km for the ICT and FT units and suggest that resurfacing has played a role in shaping the SFDs of these terrain units. We agree with that statement at smaller diameters for Regions 2, 3, and 4 (in our study 1 km $\lesssim$ D $\lesssim$ 4 km), but note that our sample size at D $\geq$ 50 km is limited so we comment on the SFD changes reported at that diameter.

One of the more likely processes for crater erasure could be overprinting of the surface by larger impacts, or the resulting debris from those larger crater formation events and their ejecta blankets, and related seismic shaking (Kirchoff & Schenk 2015). Viscous relaxation as a resurfacing mechanism would be less likely for this size range as the relaxation process more greatly affects larger craters than the craters in this diameter range and often will still leave a signal that the crater was once present on the surface (Bland et al., 2012; Hammond et al., 2013; Singer et al., 2019). Cryovolcanism has also been suggested as a method for wide-scale resurfacing on Dione (Schenk & Moore, 2009), but on the small scales that we mapped, signs of cryovolcanism weren't observed in Regions 2, 3, and 4. Region 1, on the other hand, lies within the "Smooth Terrain (ST)" unit, which is an area that has been suspected to have been fully resurfaced through

cryovolcanic activity (Schenk & Moore 2009; Kirchoff & Schenk 2015). Our counts agree well with previous reports (Kirchoff & Schenk 2015) of a shallow slope for craters between D = 15-30 km and that this steepness is not observed in the other mapped terrains.

Comparing the relative ages of the two units near the wispy terrain, their surface ages are likely similar to one another, but Region 3 may have experienced more recent resurfacing due to its slightly lower crater density between 1 and 2 km. This would not necessarily provide a constraint on the time when the faulting that formed the wispy terrain was active.

Turning to the question of how the impactor sources at Saturn may have changed over time, we compare our crate counts to the production functions (Case A and Case B) described by Zahnle et al., 2003. To accomplish this, the crater data is plotted (Figure 3.8) using methods from Robbins et al., 2018 and then compared to the cratering rates described in Zahnle et al., 2003 (see discussion in section 3.1 for further descriptions). Neither Case A or Case B fully fit the data that we've collected for Dione. Though each case does fit the crater SFDs at varying diameter ranges. Region 1's SFD fits with Case A for 2 km $\lesssim$ D $\lesssim$ 4 km then Case B fits well from 4 km up to ~ 25 km where a break in the slope occurs and neither production function is able to match that slope break. Region 2 has Case A fitting from 4 -10 km and Case B fitting from ~12 km to ~ 20 km. Once again, Region 2 has a slight break in the slope around 20 km that the production functions don't fully capture. Region 3's data fits well with Case A from 4 to ~ 10 km and then diverges away where Case B then matches from 10 km to ~ 22 km, and that production function also diverges away from the data. In contrast to the previous two regions, there

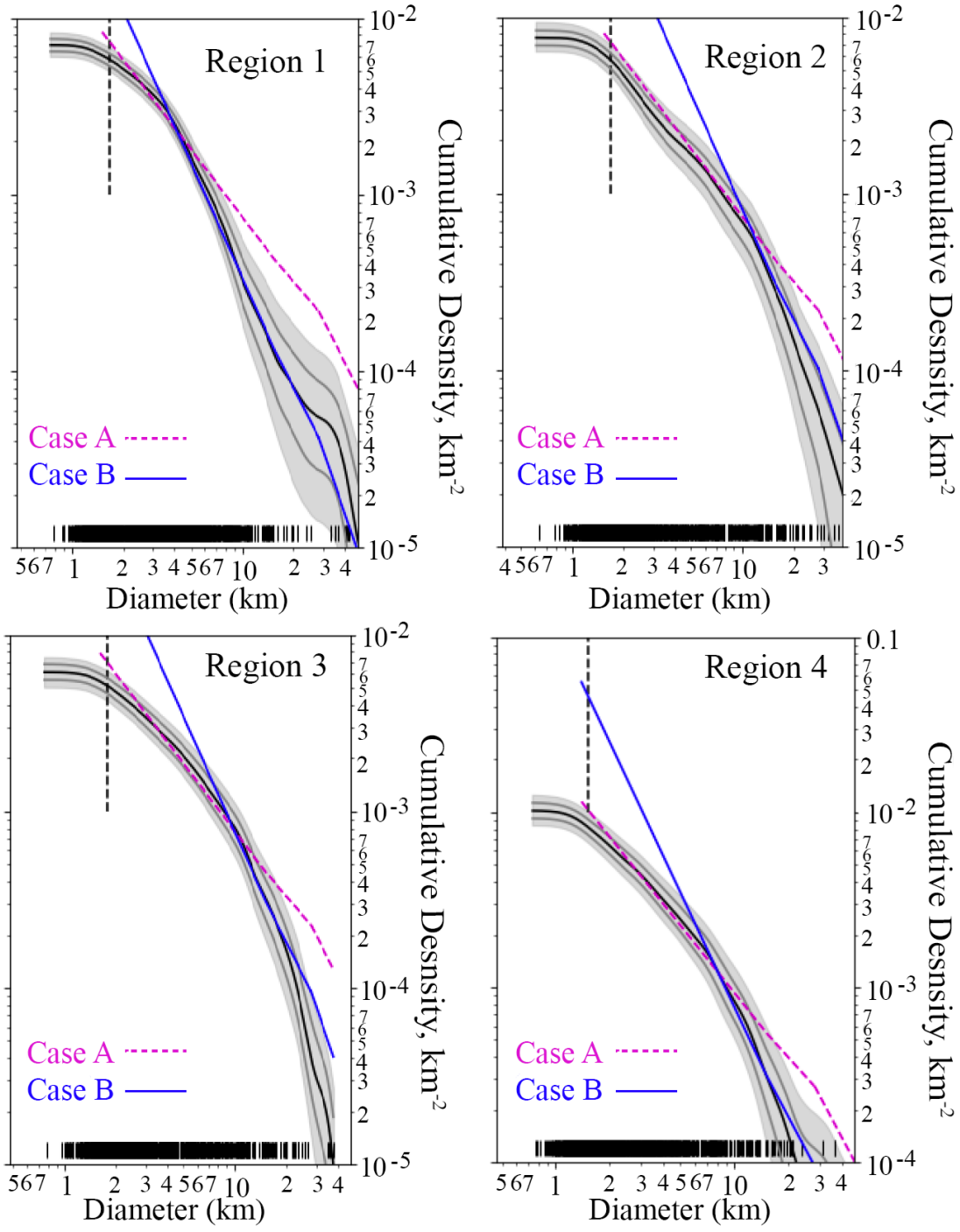

Figure 3.8. CSFDs for each mapped area with the Zahnle et al., 2003 production functions plotted on top of the data. Solid black line represents the crater counts, the grey envelope and light grey lines represent the error bounds from a kernel density estimator (Robbins et al,. 2018). Case A is represented by the dashed magenta line and Case B is represented by the solid blue line. The dashed black line represents the completeness diameter for each dataset. Short black lines (rug-plot) at the bottom represent each crater. Case A is a good fit for some diameter ranges (such as 5-10 km for Region 2), as is Case B (for example 7-20 km for Region 3), but neither are a perfect representation of the data.

isn't a slope break at 20 km though the slope becomes steeper and the Case B production function doesn't match it. For Region 4, Case A fits slightly between 3 and 7 km, then Case B fits once more from 7 – 20 km where it then slightly changes slope in a way that the crater data does not. Similarly to what was observed on Tethys (as reported in Ferguson et al., 2020), we see that neither of the described production functions fully describe the SFDs of the cratering record on Dione.

What these results imply is that the bombardment environment at Saturn is so unique to the planet that current outer planets production functions aren't fully capturing the complexities of the small body populations that are responsible for creating these craters. We suggest that these craters on Dione were created by a dominant planetocentric population that is local to Saturn. While the Case B scenario has often been thought of as representing a planetocentric source, it is still derived from heliocentric cometary cratering rates, but at a rate that differs from the observational data at Jupiter. Zahnle et al., 2003 suggest that another explanation for the Case B scenario is that it could be representative of what a planetocentric source looks like just for Triton. However, the imaging data for Triton is extremely limited, and the smallest craters in our study would not be able to be counted due to the pixel scales of the images, which range from 0.8–1.65 km/pixel (Schenk & Zahnle, 2007) for the mappable Voyager images.

Schenk & Zahnle (2007) found only 100 candidate craters larger than 5 km on the Voyager encounter hemisphere and came to the conclusion that Triton was also most likely cratered by a planetocentric source, further showing how young the surface of the moon is. Our data shows that Case B – designed to fit Triton's craters - doesn't fit Dione's craters well at the smaller diameters (1 km $\lesssim D \lesssim$ 4 km), which either implies

that Case B lacked sufficient data to accurately capture small crater slopes or that an additional heliocentric source was responsible for these smaller craters. An issue with placing responsibility for the small impacts on heliocentric objects like comets is that small enough comets may not be that abundant in these outer regions of the Solar System (Zahnle et al., 2001, 2003). Some sources for a local Saturn-centric impactor population could be from impact debris on other satellites that migrated to Dione, disruption and break up of early generation of moons, or sesquinary/secondary debris.

As a test to examine how the crater SFDs vary with distance from Saturn, we compared previous studies on Tethys to the our data from Dione (Figure 3.9). We scaled the Tethys crater diameters to Dione specific conditions following from Chapman & McKinnon 1986. Tethys is represented with the subscript 1 and Dione is represented with the subscript 2 in equation 3.2.

$$SF = \left(\frac{g_1}{g_2} * \frac{{U_2}^2}{{U_1}^2}\right) \qquad \textbf{Eq 3.2.}$$

where g_1=18.5 cm/s^2 g_2= 22.4 cm/s^2, , and U_1= 21 km/s U_2= 19 km/s. We calculate the scaling factor (SF, equation 3.2) to convert crater diameters on Tethys to Dione diameters as 0.918, so a 10 km crater on Tethys would be a 9.18 km crater on Dione. Once scaled, for our small crater range of 1- 4 km, all four Dione regions start lower in this size range and have shallower slopes, which strengthens the claim that this diameter range has been affected by resurfacing processes on Dione. If Tethys represents a well preserved ancient crater record with minimal modification, then it would follow that the shallower distributions of small craters would have been affected by resurfacing processes.

In both surveys, when these areas have been compared to the Zahnle et al., 2003 production functions, the Case B scenario does fit well at these larger diameters. It is important to note though with this comparison that the areas on Tethys are smaller than what was mapped on Dione, so fewer large (D > 20 km) were observed in the Tethys dataset. Comparisons at this larger diameter range should be made with caution due to the lack of data from Tethys. It appears that the overall shapes of the distributions on the two satellites is similar, further providing evidence for a Saturn-specific planetocentric population. The main variation between the satellites is that Dione has likely had a more geologically active history with potentially several instances of wide-scale resurfacing of the moon (Kirchoff & Schenk 2015).

When dealing with small crater diameters, it is also important to consider the possibility of crater saturation equilibrium. This is a possible state of a planetary surface where the formation of any new craters over prints the pre-existing craters, such that there is no net gain or loss in the overall SFD of the region (e.g., Chapman & McKinnon 1986). We utilize the criterion presented in Richardson, 2009 where they describe a surface as reaching crater saturation if the R-value is between 0.1 and 0.3 (this range is shown as the gray box in figs 3.6c,d). We present two R-plots to consider, one with all mapped craters (3.6c) and one with only the circular crater morphology included (6d). Examining the R-vales for fig 3.6c, each region is saturated at some diameter using the more conservative cut off of 0.1. Region 1 saturates at ~ 40 km and again at ~85 km, Regions 2-4 are then saturated from ~7- 40 km. Using a less conservative R-value of 0.2, some saturation still occurs for the Regions 3 and 4 where Region 3 is saturated at ~ 15 km and ~ 20 km and Region 4 is saturated at ~ 20 km as well. However if we examine fig

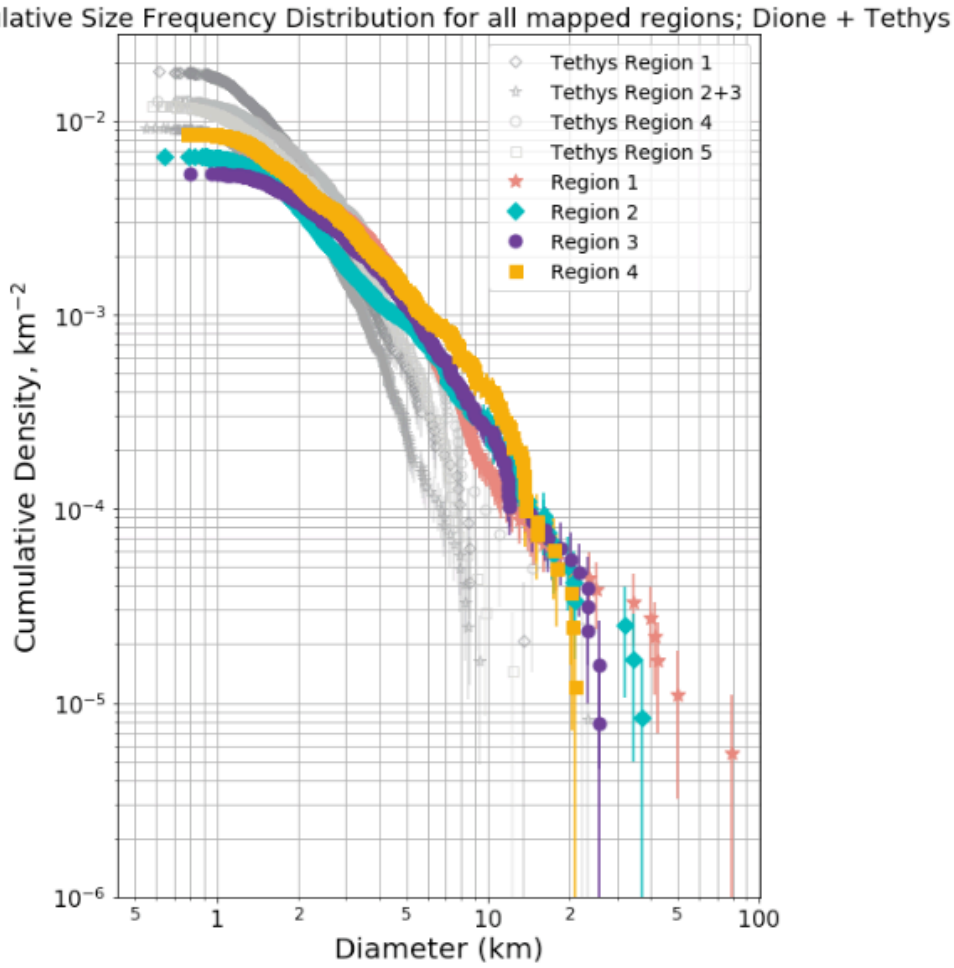

Figure 3.9. Scaled CSFD's from Tethys' gravity to Dione's. Tethys data is from Ferguson et al,. 2020 and is plotted in grey. Dione data is plotted in color in the same scheme as fig 3.6. On the whole, the diameter range between ~1-5 km has a shallower slope for the Dione data than the Tethys data, indicating that resurfacing has played a large role on this surface. Dione also has a higher density of larger (D > 20 km) craters that Tethys.

6d with just the circular craters we find that for a R-value of 0.1, only Region 4 is saturated at ~ 10 km and Region 1 reaches saturation at ~ 85 km. Using the 0.2 value for saturation then shows that none of the mapped areas have reached saturation for circular craters. We note that these distributions on the whole are shallow-sloped and the shape of the production population is still visible in these SFDs (e.g. Chapman & McKinnon 1986;

Richardson, 2009), which leads us to infer that our interpretations of the crater SFDs and the population shapes aren't affected by saturation.

Further examining the elliptical craters in the regional scale mapping, we find that they have a slight preferential orientation in the East/West direction, with an apparent isotropic signature around all other angles. This preference for an East/ West direction could be indicative of a planetocentric origin for these craters as planetocentric debris would likely impact from an East/West angle as the material would already be orbiting Saturn around the equator and in plane with the satellites. For all mapped elliptical craters, we find an average diameter of 8.74 km.

To further address what the bombardment environment at Saturn was really like, it would be valuable to generate likely SFDs for the several impactor sources that are at play within the system, so that their relative effects on the cratering records of each satellite could be untangled and possibly tied to their orbital evolution timescales. Additionally, more data from the moons of Uranus and Neptune would be ideal to further characterize the range of cratered surfaces and their respective SFDs so that a more complete analysis of the potential impactor sources at Saturn could be analyzed. Currently the only cratered surface that has been suggested to be cratered by planetocentric material outside the Saturn system is Neptune's moon, Triton (Schenk & Zahnle 2007). A mission concept submitted to NASA's Discovery program for a *New Horizons* style fast flyby of Triton (Prockter et al., 2019) would image the surface with a narrow angle camera capable of capturing images down to 200 m/pix (Mitchell et al., 2019), comparable to the resolutions used in this study. In addition to answering foundational questions about Triton's age and history, the cratering record on Triton can

then be used to further our understanding of the bombardment environment at Saturn, should the Triton craters turn out to be of a planetocentric origin.

3.5. Conclusions

Here we present new maps and crater counts within high-resolution images of Dione, which can be further utilized to analyze the bombardment environment at Saturn. Combined with orbital evolution models, these data can be used to further analyze the history and ages of the satellites in the Saturn system, thus providing more constraints on the evolution time scales of the inner mid-sized satellites. We mapped four areas on Dione: one located on the leading hemisphere, two areas on the boundaries of Dione's wispy terrain, and one area on the boundary between the leading and trailing hemisphere. We chose these areas due to their favorable lighting geometry, image resolutions, and spatial coverage across the satellite. These four mapped areas comprised a wide swath of the surface and are ideal for analyzing variations in crater SFDs with terrain types. Progress towards a more complete understanding of the formation and evolution time scales of the mid-sized moons would provide necessary constraints on evaluating the likelihood and duration of oceans within the ice shells of these satellites. We pose the following questions: 1) How much do the crater SFDs vary with terrain type, 2) What is the dominant impactor source on Dione, and 3) How do the crater SFD's change with increasing distance from Saturn?

We've counted a total of 3897 craters across four regions while also distinguishing between the crater morphologies. We find 65% of the mapped polygonal craters occur in close proximity to the wispy terrain, strengthening the evidence that these craters form within areas that have been previously fractured and show where the

subsurface may also have been fractured from tectonic processes. Based on our CSFD analysis we find that all four areas have relative ages that are close to one another and some diameters (on average between 7 and 40 km) may be saturated depending on the value used for that determination. The SFDs for small crater sizes D ~ 1-5 km show a shallow-sloped distribution that imply these craters have been erased by some resurfacing mechanism. When comparing the Dione cratering record to our previous study on Tethys, we suggest that Tethys' surface provides a look at an older, un-modified surface whereas Dione's has been extensively modified by periods of widescale resurfacing on the satellite.

Our crater SFDs don't fully agree with either of the two predicted production functions (Zahnle et al., 2003) for the Saturn system, so we hypothesize a Saturn-specific planetocentric population of impactors as being responsible for the majority of the observed craters. This conclusion is in line with our previous studies of Tethys where neither production function fully fit that data and we advocated for an unique planetocentric population to the Saturn system. These results are in line with other independent studies that also found that the cratering records support a planetocentric origin of these craters (Kirchoff & Schenk 2010, Kirchoff & Schenk 2015; Hirata 2016; Kirchoff et al., 2018; Ferguson et al., 2020; Bell 2020). What we currently see with increasing distance from Saturn is that the overall shapes and likely impactor populations of the Dione SFDs are similar to that of Tethys with the exception of the resurfacing events that have occurred during Dione's past. Further work is needed to best quantify what this planetocentric source looks like and the timescales that it could be dynamically

stable within the system. A combination of in-situ mapping studies and dynamical N-body simulations would be best equipped to carry out this kind of survey.

Dione represents a complex, possibly ocean-bearing world with several competing geologic processes that have extensively modified its surface. It's striking wispy terrain scarp features indicate a likely recent period of geologic activity and the cratering record shows extensive evidence for widescale resurfacing of the satellite. We find that, similar to its neighboring moon Tethys, Dione's craters were likely created by a planetocentric source that is unique to Saturn and does not fit previously established predictions for the cratering rates. Future missions to the Uranian and Neptunian systems could also aid in completing our knowledge of what the cratering records look like for the outer solar system, which in turn will help with narrowing down the likely sources for the craters we observe at Saturn and to settle the question if any other giant planet system has experienced a similar chaotic past.

3.6 Acknowledgments

The authors would like to acknowledge the support of a NASA Cassini Data Analysis Program grant (Grant NNX16AI42G) awarded to A.R Rhoden and a NASA Future Investigators in Earth and Space Sciences and Technology (FINESST) (grant 80NSSC19K1532) awarded to S.N. Ferguson & S. Desch, and Cassini Data Analysis Program grant (NNX17AG01G) awarded to M.R. Kirchoff for their support. Crater databases have been included as a part of this manuscript and uploaded to the data repository site figshare upon publication of the manuscript. This research has made use of the USGS Integrated Software for Imagers and Spectrometers (ISIS).

CHAPTER 4

A UNIQUE SATURNIAN IMPACTOR POPULATION FROM ELLIPTICAL CRATERS

This chapter has been submitted to the journal Earth and Planetary Science Letters as of 6/8/21 and has the permission of the following co-authors to reproduce the manuscript here in the dissertation. Co-authors include Alyssa Rhoden, Michelle Kirchoff, and Julien Salmon.

Abstract

The crater populations of Saturn's midsized icy moons are not well matched by the size-frequency distributions of impacting material inferred from other outer planet satellite systems (Kirchoff et al., 2010, 2015; Ferguson et al., 2020), frustrating attempts to date their surfaces and constrain models of their formation (Charnoz et al., 2011; Salmon & Canup 2017; Ćuk et al., 2016). Elliptical craters record the trajectories of impacting materials (Bottke et al., 2000; Elbeshausen et al., 2013; Holo et al., 2018) and can thus be used to characterize the impactors' dynamics and facilitate crater interpretations. Here, we report evidence of a Saturn-orbiting impactor population, distinct from any previously described source population, identified through global mapping and analysis of the elliptical crater populations on Saturn's moons, Tethys and Dione. Based on the crater orientations and distributions, we have isolated this population and analyzed the characteristics of the remaining craters. On both moons, these craters are better matched by the production function constructed from craters on Triton (Zahnle et al., 2003) than from the Jovian moons (Zahnle et al., 2003), although the high likelihood of planetocentric material in both the Saturnian and Neptunian systems

precludes us from determining an absolute age using the Triton production function. Rather, we can conclude that the mid-sized Saturnian satellites have been strongly affected by collisions, giving rise to a Triton-like crater population along with a unique population that is not observed at Triton. Identifying the source of this unique population places constraints on the formation and evolution of the Saturnian satellites.

4.1. Introduction:

Elliptical craters form from low-angle impacts (Bottke et al., 2000; Elbeshausen et al., 2013; Collins et al., 2011), such that the orientation of the major axis records the direction in which the impactor traveled before hitting the surface (Bottke et al., 2000; Elbeshausen et al., 2013; Holo et al., 2018). Patterns in impactor directions or locations on the surface may provide insight as to the characteristics of the impacting population. For example, heliocentric debris should enter the system at all angles (Zahnle et al., 1998), leading to elliptical craters with randomly distributed major axis orientations at all latitudes. Debris already within the Saturn system would be more likely to orbit in the same plane as the moons, so those elliptical craters may have predominantly east-west orientations and be more heavily concentrated at the equator. We generated global maps of elliptical craters and examined them for patterns in concentration, orientation, and location across the surface to identify specific source populations and their characteristics.

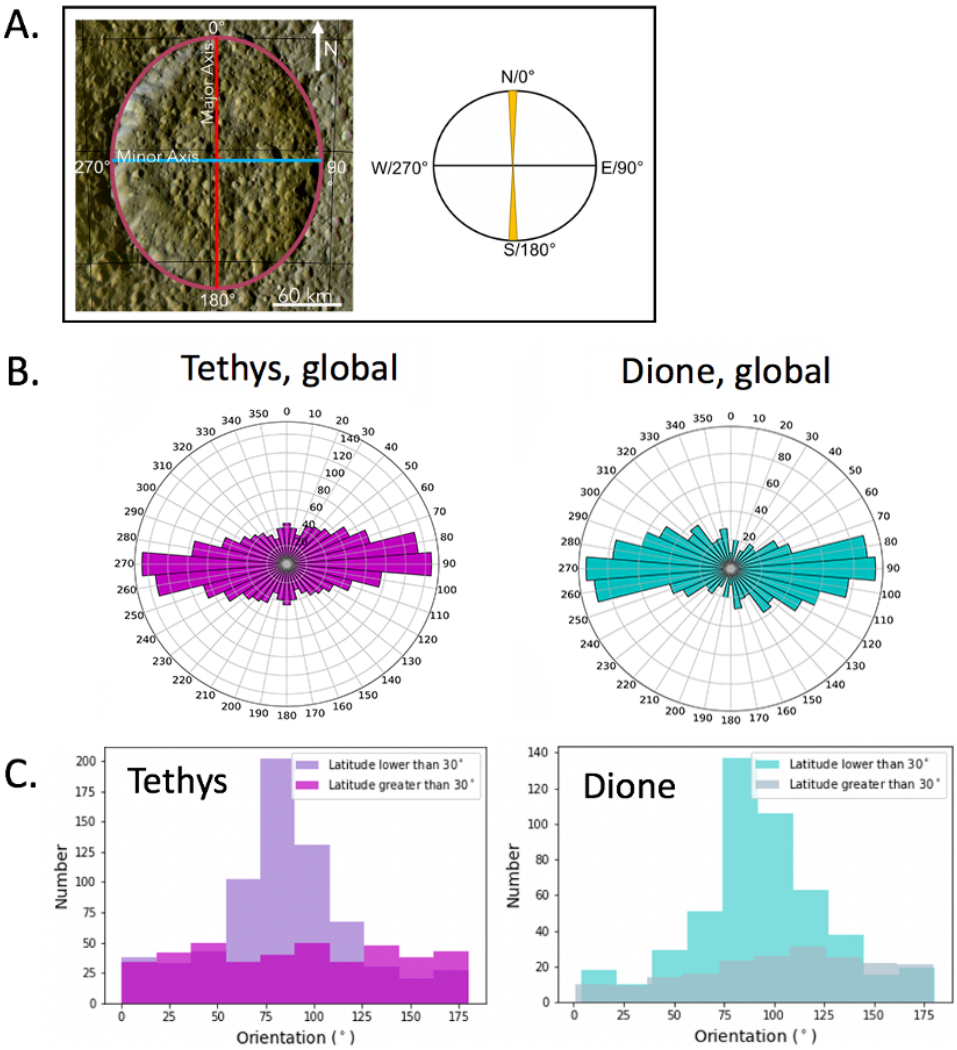

Figure 4.1. A) Penelope, a large elliptical crater on Tethys, with its major and minor axes labeled and orientation directions noted (left) and its "orientation" on a rose histogram (right). For each mapped crater in this study, we record the angle of the major axis, measured clockwise from 0° N, which for Penelope would be ~1° (a north-south orientation). B) Rose histograms of all elliptical craters mapped on Tethys (left) and Dione (right) show a strong preference for east-west oriented craters, consistent with a planetocentric source of impactors. C) Elliptical crater orientations grouped by latitude. One shade indicates craters within 30° of the equator, and the other indicates craters poleward of 30° (see legend). Here, we see that the preferred east-west orientation is largely confined to the equatorial bin; craters at higher latitudes display isotropic orientations, indicative of a heliocentric source population.

4.2. Methods

We mapped elliptical craters in the USGS global base maps of Tethys (Roatsch et al., 2009) and Dione (Roatsch et al., 2008), which have average image resolutions of 293 m/pix and 154 m/pix, respectively. We mapped across all longitudes, from 60°S to 60°N.

Poleward of ~60°, the combination of image foreshortening and lower image resolution make crater identification and measurement much more challenging. Within the mapping software, ArcGIS, the base maps are typically displayed in a simple cylindrical projection, which distorts shapes at higher latitudes. When mapping in higher latitude domains (i.e., poleward of 30°), we re-projected the base maps in ArcGIS into a sinusoidal projection, centered on the current mapping area, to ensure accurate shape identification.

We mapped all craters larger than 2 km that appeared even slightly elliptical; at this size, it is unlikely that the illumination conditions and viewing geometry of the basemap images would obscure many craters, as lighting conditions have been shown to affect craters on the scale of meters rather than kms (Ostrach, 2013). We then measured the major and minor axes of the craters with the Crater Helper Tool (Nava, 2010) for ArcGIS, which makes measurements that are independent of map projection. We computed ellipticity (ε = major axis diameter /minor axis diameter) and excluded craters with $\varepsilon < 1.2$ from our analysis (Bottke et al., 2000) to avoid any craters that only appear elliptical due to surface modification, such as wall slumping. Finally, we used *Cassini* images with better resolutions than the base maps, where available (~30-40% of our mapping area), to double-check crater shapes. As the initial classification of elliptical craters depends on the apparent shape of the crater, cross-checking with higher-resolution images and measuring all non-circular craters improves accurate identification.

We again use the Crater Helper Tool (Nava, 2010) to record the "orientation" of the craters, which we define as the azimuth of its major axis in degrees clockwise from north (Figure 4.1A). Hence, an elliptical crater with its major axis pointed east-west

would have an orientation of 90/270° and would appear as a horizontal line on a rose histogram. Although some uncertainty in the ellipticity measurement could be introduced due to lighting or viewing geometry (e.g. shadows slightly lengthening one axis), there is no obvious mechanism by which craters with a particular orientation would be preferentially missed or that an east-west oriented crater would be mistaken for a north-south one.

4.3. Results

On Tethys, which has less resurfacing, and thus a presumed older average surface age than Dione (Kirchoff & Schenk 2015; Stephan et al., 2016), we identified 1106 craters with $\varepsilon > 1.2$, which range in diameter from 2 to 70 km. On Dione, we identified 678 craters with $\varepsilon > 1.2$, which range in diameter from 3 to 73 km (none smaller than 3 km were identified). Crater locations are shown in Figure 4.2. The size ranges of these craters make it unlikely that they formed as secondary craters, in which ejecta on a ballistic trajectory from a primary impact hits the surface and forms a new crater.

Even at the global scale, we see that there is a peak in the distribution at east-west (90°/270°) oriented elliptical craters (Figure 4.1B). The signal becomes even more pronounced when we separate the craters into latitudinal bins. Figure 4.1C shows standard histograms in which the orientations of craters within 30° of the equator are in the lighter shade (purple for Tethys and teal for Dione) and poleward of 30° are in the darker shade. The 30° cutoff creates nearly the same surface area in each bin, yet there are many more elliptical craters within the equatorial bin than at higher latitudes on both Tethys (by a factor of ~1.68) and Dione (~2.4). Furthermore, the elliptical craters at

higher latitudes are nearly isotropic in orientation whereas the equatorial group is strongly peaked at east-west orientations.

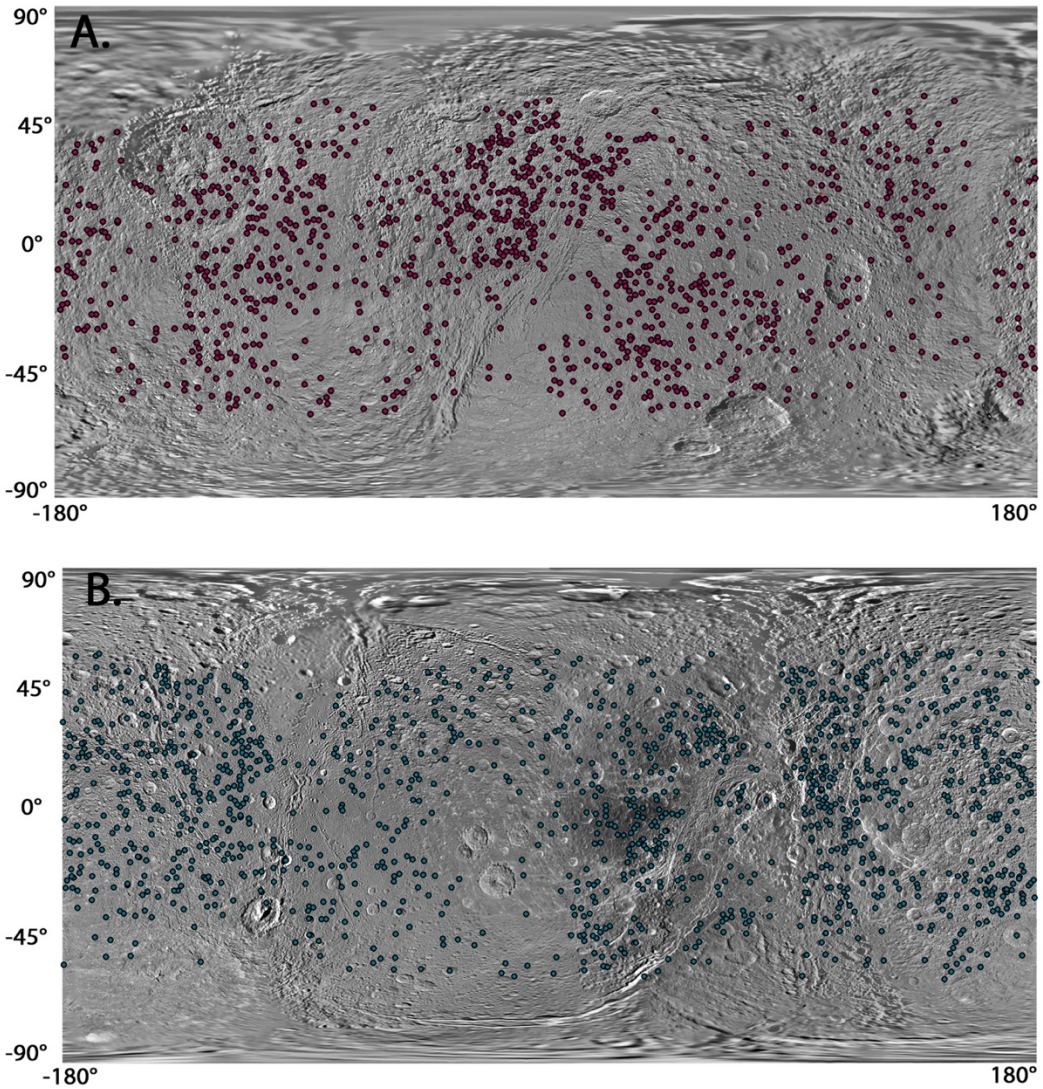

Figure 4.2. Mapped craters with ellipticities ≥ 1.2 on (A) Tethys and (B) Dione. Symbols indicate crater locations; no size information is conveyed here. Elliptical craters were identified everywhere on the moons, but their frequency is lower within regions covered by lower resolution images. Basemaps from Roatsch et al. (2008; 2009).

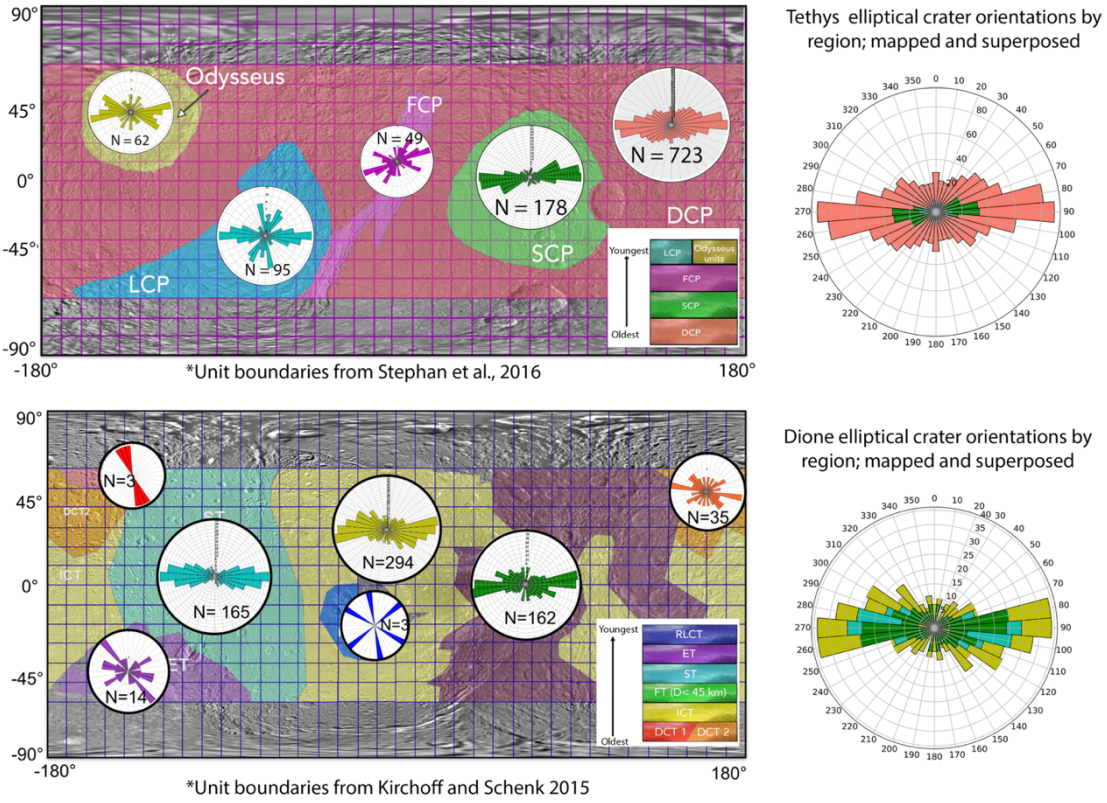

Figure 4.3. Rose histograms of elliptical crater orientations on Tethys (top) and Dione (bottom) within the geologic units described by Stephan et al. (2016) and Kirchoff & Schenk (2015), respectively. Relative stratigraphic columns are shown in the bottom right corner of each map. Rose histograms in which regions are plotted on the same radial scale are shown to the right of the maps. On Tethys, the two oldest units, the dense cratered plains (DCP) and the smooth cratered plains (SCP), have the most elliptical craters and high proportions of east-west oriented elliptical craters. The younger units show a wider spread in orientations, although they also have far fewer elliptical craters. On Dione, the two oldest units occupy a small portion of the terrain and thus have few elliptical craters, whereas the middle-aged units (ICT, FT, ST) consistently show concentrations in east-west oriented elliptical craters. The two youngest terrain units show few elliptical craters, with a spread of orientations. This lack of "younger" elliptical craters could indicate that the sources of elliptical craters decreased with time.

In Figure 4.3 (top), we show a map of Tethys, color-coded by geologic unit (Stephan et al., 2016). Superimposed on this map are rose histograms showing the orientations of the elliptical craters that fall within each geologic unit. The units with the largest numbers of craters (salmon, N = 722 and green, N = 178) have strongly peaked orientation distributions, in which elliptical craters are preferentially oriented east-west.

Regions with fewer craters have broader orientation distributions overall. Note that the scale of the radial axis of these rose histograms is different for each region (just as the y-axis on a standard histogram changes with total number of features). To the right of the map, we show the regional data superposed with the same radial scale. The broadly distributed populations from the smaller regions fit well within the annuli of isotropic orientations on the salmon/green regions. Our map of Dione (Figure 4.3, bottom) reveals similar patterns, in which regions with larger numbers of elliptical craters display preferred east-west orientations.

The elliptical craters on both Tethys and Dione indicate two distinct populations of impacting material: one that creates a global population of elliptical craters with isotropic orientations and one that creates east-west oriented craters concentrated near the equator of each moon. The isotropic population seems more consistent with a heliocentric source population. However, this population includes many small impactors, which are not observed on Pluto-Charon, perhaps pointing to a planetocentric source for at least some (and possibly all) of this material. A planetocentric source would have to be quite dispersed in order to be able to impact both Tethys and Dione globally and with no preferred impact orientation. Although a firm conclusion regarding the sources of the isotropic impactors cannot be drawn from the present data, we infer a large contribution from sesquinary impactors and/or other planetocentric sources that would impact from angles outside of Saturn's orbital plane.

The east-west population seems more consistent with what we might expect from a disk of planetocentric material. Because the moons are similarly sized (r = 531 km for Tethys and r = 561 km for Dione), the observations suggest that the population of east-

west impactors had approximately the same vertical distribution above and below Saturn's equatorial plane (~60° of latitude) at the distances of both Tethys and Dione. However, the orbits of Tethys and Dione have different inclinations (by ~1°), so a Saturn-orbiting debris disk cannot simultaneously be thin enough to match the observations and be in the orbit planes of both moons, unless Tethys' inclination increased recently relative to the emplacement of the majority of elliptical craters. Given that Tethys' inclination is pumped through a resonance with Mimas, which in turn interacts with the rings, and that Mimas and the rings could not have co-existed for more than a billion years (Neveu & Rhoden 2019) a geologically-recent inclination is plausible. Another option for the planetocentric sources, could be separate debris disks located around each satellite. However, additional mechanisms for generating such disks are necessary. Alternatively, the observations could be consistent with narrow disks (or thick rings) of material orbiting each moon. Sources of satellite-centric debris could be either the in-fall of an orbitally-decaying satellite (e.g., Phobos at Mars) or ejecta from a large impact onto the moon that flattened into a disk before reaccreting. Neither of these scenarios have been previously suggested for Tethys or Dione.

There are ~2.5 times more elliptical craters on Tethys as on Dione, which is somewhat expected given the inferred older surface age of Tethys, in which more craters have been preserved overall. If we make the assumption that regions with a larger total number of elliptical craters are older than regions with fewer elliptical craters, we can draw some inferences as to the lifetime of the planetocentric material that created the east-west elliptical craters. For regions that have hundreds of elliptical craters, relative ages based on the elliptical crater densities are consistent with age relationships reported

in the stratigraphic maps we used to classify the regions. On Tethys and (to a lesser extent) Dione there is an indication that the range of elliptical crater orientations is slightly broader within the oldest regions, then becomes more narrow in "middle-aged" terrains, and then much more isotropic in the youngest regions. Here, we have neglected regions with fewer than 20 craters, because there are too few craters to rise above the isotropic background we infer from the global populations. These trends suggest a pulse of planetocentric debris, leading to east-west elliptical craters, within a sustained flux of isotropic impactors. The oldest regions have retained the entire record, whereas middle-aged regions have retained less of the early isotropic impacts and young regions experienced little of the east-west pulse.

Crater statistics are often reported as size-frequency distributions (Crater Analysis Techniques Working Group,1979; Neukum et al., 2001), which can then be compared with a production function, the scaled size-frequency distribution (SFD) of craters formed by a hypothesized population of impactors. Attempts have been made to derive production functions of impacting material relevant to the outer solar system (Zahnle et al., 2003; Minton et al., 2012; Schlichting et al., 2013; Di Sisto & Zanardi 2013; Greenstreet et al., 2015; Singer et al., 2019) using the contemporary cometary flux at Jupiter, predicted cometary impact rates in the outer reaches of the Solar System, the cratering records of the Jovian moons, and the cratering records of Triton, Charon, and (to a limited extent) Pluto. In particular, two production functions have been constructed[10] that can be applied to the Saturnian system. The Case A production function was developed around the Jovian system, while Case B was developed around the Neptunian system. At Saturn, Case A under-predicts small craters; if Saturn has been

subjected to the same heliocentric population of impactors (e.g., comets) as Jupiter, an additional planetocentric population is required to explain the abundance of small craters on the mid-sized icy moons (Zahnle et al., 2003). Prior to the arrival of the *New Horizons* spacecraft at Pluto and the subsequent crater analysis, it was thought that the characteristics of the heliocentric population may simply be different across the giant planets (Zahnle et al., 2003). Case B attempted to capture these differences, using Triton's cratering record and a different cometary impact flux than what was used for Case A, and assumed no influence of a planetocentric population at Triton. Current understanding suggests that the Case A scenario was present throughout the Outer Solar System where its signal is strongly observed at Jupiter and the Pluto/Charon system (Singer et al., 2019). What may be occurring at Saturn is that Case A was initially present, but periods of planetocentric cratering occurred and dominate the crater record that we observe today.

Crater mapping and analyses conducted for Mimas, Tethys, and Dione are inconsistent with both the Case A and Case B production functions (Kirchoff & Schenk 2010, 2015; Ferguson et al., 2020), implying a missing (planetocentric) population of impactors within the Saturnian system. In addition, more recent observations of craters on Charon, Pluto, and Arrokoth support a consistent KBO impactor flux across the giant planets, consistent with Case A (Singer et al., 2019), further emphasizing the need for a planetocentric impactor population to explain the observed craters on the Saturnian satellites. The east-west elliptical crater population we have identified is further evidence of this missing population and provides the first glimpse at its physical characteristics.

Using the isotropic elliptical craters on Tethys and Dione may provide better fits to established production functions than the global or equatorial crater populations because there is no evidence of an equatorial concentration of impacting material on the satellites from which the functions were derived. However, scaling relationships between production functions and crater SFDs typically rely on circular craters made from head-on collisions (Collins et al., 2011), with a cosine correction to account for the common impact angle of 45°. It is unclear how to quantify and scale the dimensions of our elliptical craters for comparison with a production function. Modeling studies have shown that the dimensions and volume of elliptical craters are affected by the impact angle, in addition to the size and velocity of the impactor, but the relationship is not well-quantified and appears to be non-linear with size (Elbeshausen et al., 2009). In other words, the extent to which the crater's major axis length is affected by the impact angle is different for craters of different sizes. Furthermore, the differences in impactor velocity between a debris disk and the heliocentric population of impactors need to be quantified in order to deduce impact parameters for two elliptical crater populations with different sources.

To overcome these limitations, we have mapped circular craters in a region of Tethys north of 30° (Figure 4.4A), where the elliptical crater population is more isotropic and less affected by the unique equatorial source population. We used the same tools and methodology as for our elliptical crater mapping, but this time, we mapped all craters regardless of their shape. We then constructed an SFD for the circular craters (N=519) in the region and compared it with the Case A and Case B production functions[10]. As shown in Figure 4.4B, the slopes between our SFD of mapped craters and the Case B production

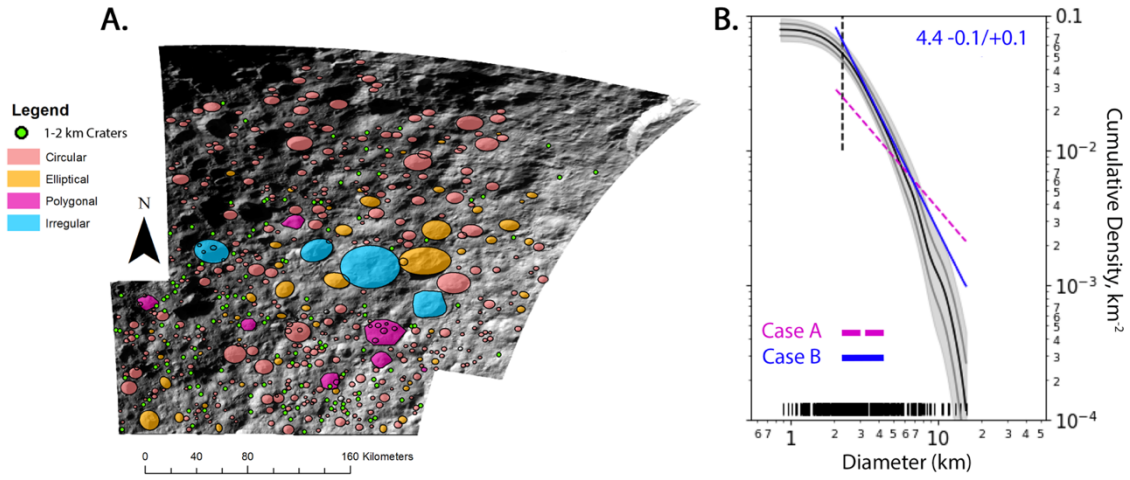

Figure 4.4. A) Regional mapping of an area on Tethys that spans the latitudes of 30° N and 60° N. The mosaic is made out of the Cassini ISS narrow angle camera images N1561669268 and N1561669433 and is displayed in an equirectangular projection. While mapping, the mosaic was re-projected to a sinusoidal projection centered at higher latitudes to ensure accurate shape measurements**.** B) Cumulative size-frequency diagram of solely the circular craters mapped in this study area fit to the Case A and Case B production functions (Zahnle et al., 2003). Case B provides a good fit to the observed SFD, with a surface age estimate of 4.4 Gyr.

function are very closely matched. Other studies have found poorer matches, likely because the planetocentric population we have identified could not be filtered out. Here, we have truncated the Case B production function at 2 km (the vertical dashed line in Fig. 4B) due to the cut-off diameter for crater size in this area, showing that the counts are complete up to 2 km. More recent cataloging of craters on Charon suggests that its SFD rolls off at small sizes[28], as we observe in our crater statistics, but that behavior is not captured in the Triton-derived production function.

4.4. Discussion & Conclusions

Based on the match between the Case B production function and the high-latitude circular craters, the average surface age we obtain for Tethys is 4.4 ± 0.1 Gyr, which implies that Tethys is either primordial or reassembled after a disruption event within a few hundred million years of solar system evolution. It is important to note, however, that

until we can disentangle planetocentric and heliocentric source populations from the cratering records used to generate production functions, there will be inherent uncertainty in these age estimates. A similar analysis could be carried out for Dione, although it has undergone substantially more resurfacing than Tethys and is, therefore, unlikely to indicate an older age. A near primordial age for Tethys would be compatible with the inference that the Odysseus impact basin formed early in Tethys' history (Dones et al., 2009; Geise et al., 2007; ~3.5 Gyr). An ancient Tethys conflicts with orbital evolution models that assume a constant Q of Saturn (Ćuk et al., 2016), highlighting the importance of incorporating a frequency-dependent/time-varying Q (Fuller et al., 2016) in such models.

The characteristics of the elliptical crater populations at Tethys and Dione provide direct evidence of a planetocentric population of impactors at Saturn. The equatorial craters are most consistent with a disk of debris orbiting each moon, or a single debris disk that led to the formation of the elliptical craters when Tethys' inclination was commensurate with that of Dione. We hypothesize that the isotropic elliptical craters represent the system's heliocentric impactor flux, along with satellite-centric material (e.g., from sesquinaries) to account for the overall low abundance of small heliocentric objects inferred from Charon's crater distributions. Based on the SFD of high-latitude, circular craters, we find that Tethys' crater population is consistent with that of Triton, and that Tethys is billions of years old. However, if Triton's craters are largely planetocentric in origin, absolute ages cannot be assigned to either moon via matches to the Case B production function.

Additional modeling and analysis of elliptical crater formation could enable direct comparisons between the observed elliptical populations and the derived production functions, while characterizing elliptical crater distributions on Saturn's more distant moons can help elucidate the origin of the isotropic elliptical craters. These future studies can provide additional constraints on the ages and formation mechanism(s) of the Saturnian moons and the sizes and distribution of impacting material within the Saturn system.

4.5. Acknowledgements: This work was supported by NASA through the following: NASA Future Investigators in Earth and Space Sciences and Technology 80NSSC19K1532, awarded to S. N. Ferguson and S. Desch, and Cassini Data Analysis Program NNX17AG01G.

CHAPTER 5

CONCLUSIONS AND FUTURE WORK

Throughout the previous chapters I have discussed the variety of impact cratering studies that have been conducted on two of Saturn's inner satellites Tethys and Dione. While these are only two moons out of seven major satellites, these moons offer ideal comparisons to one another based on their sizes and slightly differing histories. Both Tethys and Dione have experienced an intense amount of bombardment, but Dione has had seen some of that record erased by resurfacing mechanisms. Major findings of this dissertation include the following:

1. Tethys and Dione share similar crater size-frequency distributions that don't match crater production functions seen in other small bodies outside the Saturn system, which argues for a planetocentric component in addition to a heliocentric component seen elsewhere in the Outer Solar System.

Thus, we propose that a Saturn-specific planetocentric source has dominated the cratering on these satellites. Observed elliptical craters support a planetocentric source with size-frequency distribution similar to that observed at Triton as well as the Saturn-specific source.

Our ability to use production functions for age-dating of these satellites would be enhanced by having theoretical production functions that account for planetocentric material. This would require further dynamical modeling of different sources of debris to quantify the evolution and size-frequency distribution of different types of planetocentric material. Additionally, one would need to further quantify the origins of the planetocentric source and how much each source would contribute to the overall SFD of

planetocentric material. A large source of error in our derived surface age is introduced by production functions used. Until we can disentangle the planetocentric signal from the heliocentric, this remains at best a highly uncertain age.

While chronologies relating crater density to absolute model ages exist for the Inner Solar System, applying those to the Outer Planet Satellites is not advised. These production functions are based primarily off radiometric age dates for returned Lunar samples and comparisons to the crater densities (see 1.4 for more detail). Knowledge of the impactor populations (Main Belt Asteroids and Near Earth Objects) is then used to calculate a cratering rate which is then tied back to the radiometric ages and crater densities to compute an absolute age (Neukum et al., 2001; Hiesinger et al., 2012). Knowledge of the cratering rates build up the crater production functions for the Moon, which are then extrapolated out to other planets like Mars (Hartmann 2005). This extrapolation works in the sense that it is accounting for the same impactor sources at both the Moon and Mars, but even then the uncertainty in the age value grows at Mars due to the lack of returned samples. Anchor points on the Lunar chronology are also limited to two main epochs around ~4 Gyr old and ~ 800 Myr old (Hiesinger et al., 2012), leaving billions of years of Lunar history uncorrelated with a crater density. For the Asteroid Belt, an additional production function exists, which is based off collisional rates in that area of space. The craters on Ceres are dated using both the lunar and asteroid derived models, but the asteroid derived model has been favored due to it's direct applicability to that region of the Solar System (Marchi et al., 2016). Applying either of these models for Outer Solar System cratering further increases the error in the measurments since these objects are cratered by fundamentally different sources and at

different rates. Attempts have been made at using Inner Solar System chronologies on Outer Solar System craters, but they result in either poor fits or poor uncertainties (Neukum et al., 2005; Schmedemann et al., 2021). While the ages obtained do date to ~4.4 Gyr ago, the error bounds on this measurement are larger. It's also conceivable that a large object could be catastrophically disrupted in the Saturn system, leading to a pulse of planetocentric material. These poor agreements show that crater age systems for the Inner Solar System are not compatible with the observed craters in the Outer Planets.

We only examined Odysseus as a source for secondaries on Tethys, other large craters on the surface, such as Penelope, could be equally responsible for an increase in the small crater record, and further modeling should be conducted to address the impact of secondaries on the cratering record. Quantifying the effect of debris from the co-orbital moons of Tethys and Dione on their small crater populations could also help constrain the contributions from different potential source populations. Further, an outstanding question is, Are Tethys and Dione unique in the Saturn system for having co-orbital satellites? Did the other satellites once have these, but they were then destabilized and are no longer observed in the current configuration of the system?

2. Dione is interpreted as having been resurfaced extensively, based on the lower heliocentric impactor flux, the dearth of small craters (1 km < D < 4 km) relative to Tethys, and shallow sloped distributions of the craters.

With the large degree of putative resurfacing and other active processes on Dione, it's warranted to further examine the conditions in which an ocean could exist on the satellite and how it would affect the observed geology. The presence of an ocean that eventually froze out, like that on Charon, would most likely produce an extensional

tectonic signature and would otherwise weaken the subsurface. This subsequent weakening of the subsurface would make it easier for polygonal craters to form when the surface is impacted. Other resurfacing mechanisms like impact gardening and cryovolcanism should also be further investigated as to assess the extent at which these each have affected the cratering record.

3. Elliptical craters aligned in an east-west direction around the equators of both Tethys and Dione can be attributed to this planetocentric component, and the influence of the planetocentric cratering can be assessed and accounted for in future cratering studies.

The majority of these observed elliptical craters are located within areas on the satellites that have been interpreted to be older terrain units with approximate ages around ~2-4 Gyr. One outstanding question is: what sources were responsible for these elliptical craters? Two sources at least would have to be responsible for creating these elliptical craters: one for the isotropically-oriented craters, and another for the observed East/West signature. Further modeling exploring the nature of a debris disk as the origin for the East/West craters is desired to begin untangling the question of the origins of these craters. Furthermore, extending the study of elliptical craters to the other satellites in the system would provide important benchmarks as to the extent and thickness of this potential debris disk. Iapetus represents an ideal moon to test against as it is the furthest away from Saturn and should be dominated by a heliocentric signature in its craters. Rhea and Mimas would then provide more limits on the extent of any debris disk as they are the outer most and inner most satellites, respectively, within the mid-sized icy moons.

Additional impact modeling for the formation and scaling of elliptical craters is also critical to improving how the crater dimensions are scaled between circular and elliptical craters. Tied with the scaling of these craters is how the presence of an ocean could affect the resulting shapes of the craters. Moreover, characterizing the morphologies of these craters through the use of digital elevation models would assist in refining the knowledge of how elliptical craters are formed in ice.

4. Tethys is interpreted to be an ancient surface modified by impacts. Some regions (Region 1) are older than the other regions. Subtracting the planetocentric component, we estimate from the heliocentric component that the oldest regions are ~4.4 Gyr old.

Underlying the questions about ages and oceans is the question, What is the internal heat budget of these satellites? Do these satellites retain enough heat to maintain an ocean and if they do, how long is that ocean sustained? In addition to heat generated by the decay of radioactive isotopes in the cores/mantles of the satellites, Saturn's satellites have been tidally evolved and either have been heated or are currently heated by these resulting tides. The surfaces of these satellites can further be affected by the heat flow through viscous relaxation, in which a sustained heat flux can erase the signatures of impact craters on the surface.

5. These findings suggest Tethys and Dione are likely primordial, but a debris disk formed at some point in their evolution, perhaps associated with breakup of a previous moon and formation of a new moon and was responsible for the planetocentric cratering. Our findings support the model of Neveu & Rhoden in which Tethys and Dione are likely primordial, but Mimas formed more recently

from a debris disk. Future work may refine the timing constraints of when a disk formed and how long one could be sustained.

Currently, I cannot fully rule out formation models or ages for these satellites, but I do support that these moons are much older than 100 Myr and are likely around 3-4.5 Gyr old. One highly uncertain parameter that should be more constrained in an effort to rule out formation models is that of Saturn's quality factor Q. This value in the literature is often held as constant rather than varying with frequency (Fuller et al., 2016). Results presented here suggest that Tethys is indeed an ancient satellite, which conflicts with orbital evolution models that hold Q constant over time and imply a younger age for the satellite. Modeling completed by Neveu & Rhoden 2019 does vary Q by linearly decreasing it with time, and these results also imply an older system of satellites: Rhea must form primordially; Tethys, Dione, and Enceladus are predicted to form no later than 2 Gyr ago, ~ 2 Gyr depending on initial conditions; and Mimas can only be as old as 1 Gyr, as constrained by its interactions with Saturn's rings. Recent modeling of the thermo-orbital evolution of the satellites does depend on the initial Q of Saturn and this did not incorporate the full frequency-dependent Q model, but Q is still decreased linearly with time (Neveu & Rhoden 2019). Astrometry work by Lainey et al., 2017 has suggested that each moon might "lock on" to a different layer of Saturn's atmosphere, which would require each satellite to have its own resonance-dependent Q. Incorporation of this frequency-dependent Q into the orbital evolution models of this system will be key to unraveling the true history of this system.

Progress towards answering questions about the increasingly complex Saturn system can be made with the development and flight of new missions to both Saturn and the Ice Giants. A return to the Saturn system with an orbiter mission equipped with a laser altimeter and a camera capable of capturing images with a pixel scale of 100 m/pix for close flybys of the satellites would further enable detailed geologic analysis of surface features on these moons. A design for a tour in the system would ideally include more Mimas flybys as well, due to the limited nature of the high-resolution coverage of Mimas from *Cassini*. Additionally, further direct planning for stereo imaging of the surfaces would aid in the analysis of the surface geology by allowing for a higher-resolution view of the topography of the satellites. Examining the topography and how it varies across a surface is a key to determining the interior heat flux and the thermal gradient that the satellite may have experienced in its past (e.g., through viscous relaxation). The addition of a laser altimeter would allow for absolute elevation values to be obtained and easily compared across the surface of the satellite and other moons in the system. Similar to how the Ganymede Laser Altimeter (GALA) instrument onboard ESA's JUICE mission is being utilized to examine the tidal response on Ganymede and further confirm an ocean underneath the ice shell (Luedicke et al., 2019), a laser altimeter at the Saturn system could further measure the tidal responses of these satellites as well and potentially answer the question about a current ocean underneath the ice shell of Dione.

Uranus and Neptune are the two remaining planets in the outer solar system that have yet to be visited with a dedicated spacecraft mission since their initial exploration during the *Voyager* mission in 1986 and 1989. Current orbital dynamics necessitate a return to the Ice Giants by launching during the years 2029-2030 for Uranus and 2030-2034 for

Neptune (Leonard et al., 2020; Beddingfield et al., 2020; Cartwright et al., 2020) to take advantage of a gravity assist from Jupiter and image the system in a seasonally different configuration than what was observed with the *Voyager* probes. Otherwise, the next available launch window is in the 2040's with an extended cruise duration due to missing the Jupiter gravity assist. Current cruises are planned for 15 years (Hofstadter et al., 2017) to accommodate instrument and power system lifetimes. A delayed launch into the 2040's would increase technological risk as systems such as the radioisotope power supply are only rated for a 15-year duration (Hofstadter et al., 2017). Overcoming this limitation would require further financial investment into advancing the technologies that would be used on such a spacecraft. Launching a spacecraft to Uranus in the 2030-2034 window allows for the spacecraft to reach the system before Uranus reaches its equinox, which allows for imaging of new locations on the satellites that were previously unseen in the *Voyager* dataset. Uranus represents a unique system to study theories of giant planet formation, as it has an extensive regular satellite system (unlike Neptune). Key questions to understanding the nature of the Ice Giant satellites include.

- "Does a current ocean exist underneath the ice shells of the Ice Giant satellites?" (Leonard et al., 2020)
- "Did a subsurface ocean exist in the past?" (Beddingfield et al., 2020; Leonard et al., 2020)
- "What geologic processes modify the surface and has there been communication between the surface and interior?" (Beddingfield et al., 2020)

The satellites of Uranus, as well as Neptune's Triton, all exhibit signs of "recent" geologic activity (Smith et al., 1989; Papalardo et al., 1997; Prockter et al., 2005;

Beddingfield et al., 2015; Leonard & Pathoff 2019) and an intriguing cratering record. Cratering studies of the Uranian moons suggested a primarily heliocentric cratering component (Strom 1987; McKinnon et al., 1991), but the returned imaging data was incredibly limited and differences in image processing and crater counting methodologies have been a source of debate within the community (McKinnon et al., 1991). In contrast, a re-analysis of the Triton data by Schenk & Zahnle 2007 interpreted the Triton cratering record to be dominated by planetocentric cratering due to impacts onto the other satellites sending debris to Triton and creating craters. A return to the Uranian satellites as well as the Neptunian satellites would enable an up-close look at the cratering record at a scale unresolvable to Voyager 2. This would allow for the completion of detailed crater counts and studies of comparative planetology between the outer planets (and the Pluto-Charon system). This comparison study would further address whether or not Saturn is unique in the Solar System for having a cratering record so dominated by planetocentric impacts.

The Saturnian system is one of the most complicated planetary systems in our Solar System. Active debate and research continues into how the planet, satellites, and its rings could all form and the time scales at which this occurred. Further complicating the issue is the examination of tides and moon-moon resonances on the orbital evolution of these satellites. One of the remaining questions about the Saturnian satellites has been how old are they? Results from my dissertation support the idea that Tethys and Dione are old satellites (>> 1 Gyr) and are not as young as 100 Myr old. Further study is warranted on the dynamics of the planetocentric sources within the system to answer questions about the timing of impacts onto these satellites. Many questions remain unanswered about the

Saturn system, but with future exploration of the Ice Giants and a return to Saturn they can be answered.

REFERENCES

Alvarellos, J.L., Dobrovolskis, A.R., Zahnle, K.J., Hamill, P., Dones, L., Robbins, S., 2017. Fates of satellite ejecta in the Saturn system, II. Icarus 284, 70–89. doi:10.1016/j.icarus.2016.10.028

Alvarellos, J.L., Zahnle, K.J., Dobrovolskis, A.R., Hamill, P., 2005. Fates of satellite ejecta in the Saturn system. Icarus 178, 104–123. doi:10.1016/j.icarus.2005.04.017

Anderson, J., Sides, S.C., 2004. Modernization of the integrated software for imagers and spectrometers. Lunar Planet. … 2039.

Asphaug, E., Reufer, A., 2013. Late origin of the Saturn system. Icarus 223, 544–565. doi:10.1016/j.icarus.2012.12.009

Bailen, M.S., Sucharski, R.M., Akins, S.W., Hare, T., Gaddis, L., 2013. Using the PDS Planetary Image Locator Tool (PILOT) to Identify and Download Spacecraft Data for Research. 44th Lunar Planet. Sci. Conf. abstract #2246.

Beddingfield, C.B., Burr, D.M., Dunne, W.M., 2015. Shallow normal fault slopes on Saturnian icy satellites. J. Geophys. Res. E Planets 120, 2053–2083. doi:10.1002/2015JE004852

Beddingfield, C.B., Burr, D.M., Tran, L.T., 2016. Polygonal impact craters on Dione: Evidence for tectonic structures outside the wispy terrain. Icarus 274, 163–194. doi:10.1016/j.icarus.2016.03.020

Beddingfield, C.B., Cheng, L., Atreya, S., Mark, H., Fortney, J., Showalter, M., Beauchamp, P., Heidi, H., Cohen, I., Rymer, A., Schenk, P., Hedman, M., 2020. Exploration of the Ice Giant Systems, White Papers for the 2023-2033 Planetary Science Decadal Survey.

Bell, S.W., 2020. Relative Crater Scaling Between the Major Moons of Saturn: Implications for Planetocentric Cratering and the Surface Age of Titan. J. Geophys. Res. Planets 125, 1–18. doi:10.1029/2020JE006392

Beuthe, M., Rivoldini, A., Trinh, A., 2016. Enceladus's and Dione's floating ice shells supported by minimum stress isostasy. Geophys. Res. Lett. 43, 10,088-10,096. doi:10.1002/2016GL070650

Bierhaus, E.B., Dones, L., Alvarellos, J.L., Zahnle, K., 2012. The role of ejecta in the small crater populations on the mid-sized saturnian satellites. Icarus 218, 602–621. doi:10.1016/j.icarus.2011.12.011

Bierhaus, E.B., McEwen, A.S., Robbins, S.J., Singer, K.N., Dones, L., Kirchoff, M.R., Williams, J.P., 2018. Secondary craters and ejecta across the solar system:

Populations and effects on impact-crater–based chronologies. Meteorit. Planet. Sci. 53, 638–671. doi:10.1111/maps.13057

Bland, M.T., Singer, K.N., Mckinnon, W.B., Schenk, P.M., 2012. Enceladus' extreme heat flux as revealed by its relaxed craters. Geophys. Res. Lett. 39, 1–5. doi:10.1029/2012GL052736

Bottke, W.F., Love, S.G., Tytell, D., Glotch, T., 2000. Interpreting the elliptical crater populations on mars, venus, and the moon. Icarus 145, 108–121. doi:10.1006/icar.1999.6323

Cameron, A, G, W., Ward, W.R., 1976. The Origin of the Moon. Lunar Planet. Sci. Conf. 7, 120.

Campo Bagatin, A., Benavidez, P.G., 2012. Collisional evolution of trans-Neptunian object populations in a Nice model environment. Mon. Not. R. Astron. Soc. 423, 1254–1266. doi:10.1111/j.1365-2966.2012.20954.x

Canup, R.M., 2010. Origin of Saturns rings and inner moons by mass removal from a lost Titan-sized satellite. Nature 468, 943–946. doi:10.1038/nature09661

Canup, R.M., Ward, W.R., 2006. A common mass scaling for satellite systems of gaseous planets. Nature 441, 834–839. doi:10.1038/nature04860

Cartwright, R., Beddingfield, C., Nordheim, T., Elder, C., Grundy, W., Bramson, A., Sori, M., Pappalardo, R., Ermakov, A., Roser, J., Castillo-Rogez, J., Turtle, Z., Hofstadter, M., n.d. The Science Case for Spacecraft Exploration of the Uranian Satellites, White Papers for the 2023-2033 Planetary Science Decadal Survey. doi:10.3847/25c2cfeb.534f7e8d

Castillo-Rogez, J.C., Hemmingway, D., Rhoden, A.R., Tobie, G., McKinnon, W.B., 2018. Origin and Evolution of Saturn's Mid-Sized Moons, Enceladus and the Icy Moons of Saturn. Univ. of Arizona Press, Tucson AZ. doi:10.2458/azu_uapress_9780816537075-ch014.

Chapman, C.R., McKinnon, W.B., 1986. Cratering of planetary satellites, in Satellites, in: Satellites. pp. 492–580.

Charnoz, S., Crida, A., Castillo-Rogez, J.C., Lainey, V., Dones, L., Karatekin, Ö., Tobie, G., Mathis, S., Le Poncin-Lafitte, C., Salmon, J., 2011. Accretion of Saturn's mid-sized moons during the viscous spreading of young massive rings: Solving the paradox of silicate-poor rings versus silicate-rich moons. Icarus 216, 535–550. doi:10.1016/j.icarus.2011.09.017

Charnoz, S., Salmon, J., Crida, A., 2010. The recent formation of Saturn's moonlets from

viscous spreading of the main rings. Nature 465, 752–754. doi:10.1038/nature09096

Chen, E.M.A., Nimmo, F., 2008. Implications from Ithaca Chasma for thermal and orbital history of Tethys. Geophys. Res. Lett. 35, 1–4. doi:10.1029/2008GL035402

Clark, R.N., Curchin, J.M., Jaumann, R., Cruikshank, D.P., Brown, R.H., Hoefen, T.M., Stephan, K., Moore, J.M., Buratti, B.J., Baines, K.H., Nicholson, P.D., Nelson, R.M., 2008. Compositional mapping of Saturn's satellite Dione with Cassini VIMS and implications of dark material in the Saturn system. Icarus 193, 372–386. doi:10.1016/j.icarus.2007.08.035

Collins, G.C., Mckinnon, W.B., Moore, J.M., Nimmo, F., Pappalardo, R.T., Prockter, L.M., Schenk, P.M., Watters, T.R., Schultz, R.A., 2009. Tectonics of the outer planet satellites. Planet. Tectonics 264–350.

Collins, G.S., Elbeshausen, D., Davison, T.M., Robbins, S.J., Hynek, B.M., 2011. The size-frequency distribution of elliptical impact craters. Earth Planet. Sci. Lett. 310, 1–8. doi:10.1016/j.epsl.2011.07.023

Crater Analysis Techniques Working Group, Arvidson, R., Boyce, J., Chapman, C., Cintala, M., Fulchignoni, M., Moore, H., Schultz, P., Soderblom, L., Strom, R., Woronow, A., Young, R., 1979. Standard techniques for presentation and analysis of crater size-frequency data. Icarus 37, 467–474. doi:10.1016/0019-1035(79)90009-5

Crida, A., Charnoz, S., 2012. Formation of regular satellites from ancient massive rings in the solar system. Science (80-.). 338, 1196–1199. doi:10.1126/science.1226477

Crow-Willard, E.N., Pappalardo, R.T., 2015. Structural mapping of Enceladus and implications for formation of tectonized regions. J. Geophys. Res. Planets 120, 928–950. doi:10.1002/2015JE004818

Ćuk, M., Dones, L., Nesvorný, D., 2016. Dynamical Evidence for a Late Formation of Saturn's Moons. Astrophys. J. 820, 97. doi:10.3847/0004-637X/820/2/97

Dalle Ore, C.M., Cruikshank, D.P., Mastrapa, R.M.E., Lewis, E., White, O.L., 2015. Impact craters: An ice study on Rhea. Icarus 261, 80–90. doi:10.1016/j.icarus.2015.08.008

Daubar, I.J., McEwen, A.S., Byrne, S., Kennedy, M.R., Ivanov, B., 2013. The current martian cratering rate. Icarus 225, 506–516. doi:10.1016/j.icarus.2013.04.009

Di Sisto, R.. . ., Zanardi, M., 2013. The production of craters on the mid-sized Saturnian satellites by Centaur objects. Astron. Astrophys. A79, 1–9.

Di Sisto, R.P., Brunini, A., 2007. The origin and distribution of the Centaur population.

Icarus 190, 224–235. doi:10.1016/j.icarus.2007.02.012

Di Sisto, R.P., Zanardi, M., 2016. Surface ages of mid-size saturnian satellites. Icarus 264, 90–101. doi:10.1016/j.icarus.2015.09.012

Dobrovolskis, A.R., Alvarellos, J.L., Zahnle, K.J., Lissauer, J.J., 2010. Exchange of ejecta between Telesto and Calypso: Tadpoles, horseshoes, and passing orbits. Icarus 210, 436–445. doi:10.1016/j.icarus.2010.06.023

Dones, L., Chapman, C.R., McKinnon, W.B., Melosh, H.J., Kirchoff, M.R., Neukum, G., Zahnle, K.J., 2009. Icy satellites of saturn: Impact cratering and age determination, in: Saturn from Cassini-Huygens. pp. 613–635. doi:10.1007/978-1-4020-9217-6_19

Elbeshausen, D., Wünnemann, K., Collins, G.S., 2013. The transition from circular to elliptical impact craters. J. Geophys. Res. E Planets 118, 2295–2309. doi:10.1002/2013JE004477

Elbeshausen, D., Wünnemann, K., Collins, G.S., 2009. Scaling of oblique impacts in frictional targets: Implications for crater size and formation mechanisms. Icarus 204, 716–731. doi:10.1016/j.icarus.2009.07.018

Fassett, C.I., 2016. Analysis of impact crater populations and the geochronology of planetary surfaces in the inner solar system. J. Geophys. Res. E Planets 121, 1900–1926. doi:10.1002/2016JE005094

Ferguson, S.N., Rhoden, A.R., Bierhaus, E.B., 2018. Interpreting the small crater record of Tethys and the role of secondary craters. 48th Lunar Planet. Sci. Conf. 2018, 3–4.

Ferguson, S.N., Rhoden, A.R., Kirchoff, M.R., 2020. Small Impact Crater Populations on Saturn's Moon Tethys and Implications for Source Impactors in the System. J. Geophys. Res. Planets 125, 1–21. doi:10.1029/2020JE006400

Fuller, J., Luan, J., Quataert, E., 2016. Resonance locking as the source of rapid tidal migration in the Jupiter and Saturn moon systems. Mon. Not. R. Astron. Soc. 458, 3867–3879. doi:10.1093/mnras/stw609

Gault, D.E., Wedekind, J.A., 1978. Experimental Studies of Oblique Impact, in: 9th Lunar and Planetary Science Conference. pp. 3843–3875.

Giese, B., Wagner, R., Neukum, G., Helfenstein, P., Thomas, P.C., 2007. Tethys: Lithospheric thickness and heat flux from flexurally supported topography at Ithaca Chasma. Geophys. Res. Lett. 34, 1–5. doi:10.1029/2007GL031467

Greenstreet, S., Gladman, B., McKinnon, W.B., 2015. Impact and cratering rates onto Pluto. Icarus 258, 267–288. doi:10.1016/j.icarus.2015.05.026

Hammond, N.P., Phillips, C.B., Nimmo, F., Kattenhorn, S.A., 2013. Flexure on Dione: Investigating subsurface structure and thermal history. Icarus 223, 418–422. doi:10.1016/j.icarus.2012.12.021

Hartmann, W.K., 2005. Martian cratering 8: Isochron refinement and the chronology of Mars. Icarus 174, 294–320. doi:10.1016/j.icarus.2004.11.023

Hendrix, A.R., Filacchione, G., Paranicas, C., Schenk, P., Scipioni, F., 2018. Icy Saturnian satellites: Disk-integrated UV-IR characteristics and links to exogenic processes. Icarus 300, 103–114. doi:10.1016/j.icarus.2017.08.037

Hiesinger, H., Marchi, S., Schmedemann, N., Schenk, P., Pasckert, J.H., Neesemann, A., O'Brien, D.P., Kneissl, T., Ermakov, A.I., Fu, R.R., Bland, M.T., Nathues, A., Platz, T., Williams, D.A., Jaumann, R., Castillo-Rogez, J.C., Ruesch, O., Schmidt, B., Park, R.S., Preusker, F., Buczkowski, D.L., Russell, C.T., Raymond, C.A., 2016. Cratering on ceres: Implications for its crust and evolution. Science (80-.). 353. doi:10.1126/science.aaf4759

Hiesinger, H., Van Der Bogert, C.H., Pasckert, J.H., Funcke, L., Giacomini, L., Ostrach, L.R., Robinson, M.S., 2012. How old are young lunar craters? J. Geophys. Res. E Planets 117, 1–15. doi:10.1029/2011JE003935

Hirata, N., 2016. Differential impact cratering of Saturn's satellites by heliocentric impactors. J. Geophys. Res. Planets 121, 111–117. doi:10.1002/2015JE004940

Hofstadter, M., Simon, A., Atreya, S., Banfield, D., Fortney, J., Hayes, A., Hedman, M., Hospodarsky, G., Masters, A., Mandt, K., Showalter, M., Soderlund, K., Turrini, D., Turtle, E., 2017. Ice Giant Pre-Decadal Mission Study, Jpl-D 100520.

Holo, S.J., Kite, E.S., Robbins, S.J., 2018. Mars obliquity history constrained by elliptic crater orientations. Earth Planet. Sci. Lett. 496, 206–214. doi:10.1016/j.epsl.2018.05.046

Holsapple, K.A., 1993. The scaling of impact phenomena. Annu. Rev. Earth Planet. Sci. 21, 333–373. doi:10.1016/0734-743X(87)90051-0

Horedt, G.P., Neukum, G., 1984a. Cratering rate over the surface of a synchronous satellite. Icarus 60, 710–717. doi:10.1016/0019-1035(84)90175-1

Horedt, G.P., Neukum, G., 1984b. Planetocentric Versus Heliocentric Impacts in the Jovian and Saturnian Satellite System. J. Geophys. Res. 89, 10405–10410. doi:10.1029/JB089iB12p10405

Iess, L., Militzer, B., Kaspi, Y., Nicholson, P., Durante, D., Racioppa, P., Anabtawi, A.,

Galanti, E., Hubbard, W., Mariani, M.J., Tortora, P., Wahl, S., Zannoni, M., 2019. Measurement and implications of Saturn's gravity field and ring mass. Science (80-.). 364. doi:10.1126/science.aat2965

Ivanov, B.A., 2001. Mars/Moon cratering rate ratio estimates. Space Sci. Rev. 96, 87–104. doi:10.1023/A:1011941121102

Kattenhorn, S.A., Hurford, T., 2009. Tectonics of Europa, Europa. Univ. of Arizona Press, Tucson AZ. doi:10.2307/j.ctt1xp3wdw.15

Kirchoff, M.R., Bierhaus, E.B., Dones, L., Singer, K.N., Robbins, S.J., Wagner, R.J., Zahnle, K.J., 2018. Cratering Histories in the Saturnian System, in: Schenk, P.M. (Ed.), Enceladus and the Icy Moons of Saturn. Univ. of Arizona Press, Tucson AZ, Tucson, pp. 267–284. doi:0.2458/azu_uapress_9780816537075-ch013

Kirchoff, M.R., Schenk, P., 2015. Dione's resurfacing history as determined from a global impact crater database. Icarus 256, 78–89. doi:10.1016/j.icarus.2015.04.010

Kirchoff, M.R., Schenk, P., 2010. Impact cratering records of the mid-sized, icy saturnian satellites. Icarus 206, 485–497. doi:10.1016/j.icarus.2009.12.007

Lainey, V., Jacobson, R.A., Tajeddine, R., Cooper, N.J., Murray, C., Robert, V., Tobie, G., Guillot, T., Mathis, S., Remus, F., Desmars, J., Arlot, J.E., De Cuyper, J.P., Dehant, V., Pascu, D., Thuillot, W., Poncin-Lafitte, C. Le, Zahn, J.P., 2017. New constraints on Saturn's interior from Cassini astrometric data. Icarus 281, 286–296. doi:10.1016/j.icarus.2016.07.014

Lainey, V., Karatekin, Ö., Desmars, J., Charnoz, S., Arlot, J.E., Emelyanov, N., Le Poncin-Lafitte, C., Mathis, S., Remus, F., Tobie, G., Zahn, J.P., 2012. Strong tidal dissipation in saturn and constraints on Enceladus' thermal state from astrometry. Astrophys. J. 752. doi:10.1088/0004-637X/752/1/14

Landis, M.E., Byrne, S., Combe, J.-P., Marchi, S., Castillo-Rogez, J.C., Sizemore, H.G., Schörghofer, N., Prettyman, T.H., Hayne, P.., Raymond, C.A., Russell, C.T., 2019. Water Vapor Contribution to Ceres' Exosphere From Observed Surface Ice and Postulated Ice-Exposing Impacts. J. Geophys. Res. Planets 124, 61–75.

Leonard, E., Elder, C., Nordheim, T., Cartwright, R., Patthoff, D.A., Beddingfield, C., Tiscareno, M., Strange, N., Balint, T., 98 co-signers/endorsers, 2020. A New Frontiers Class Mission for the Uranian System that Focuses on Moon, Magnetosphere, and Ring Science, White Papers for the 2023-2033 Planetary Science Decadal Survey.

Lissauer, J.J., Squyres, S.W., Hartmann, W.K., 1988. Bombardment history of the Saturn system. J. Geophys. Res. 93, 776–804. doi:10.1029/jb093ib11p13776

López-Oquendo, A.J., Rivera-Valentín, E.G., Ore, C.M.D., Kirchoff, M.R., Nichols-Fleming, F., Long, C.J., Scipioni, F., 2019. Constraints on Crater Formation Ages on Dione From Cassini VIMS and ISS. Lunar Planet. Sci. Conf.

Luedicke, F., Hussmann, H., Lingenauber, K., Kallenbach, R., Enya, K., 2020. Exploring the icy moons of Jupiter : The Ganymede Laser Altimeter (GALA) for ESA' s JUICE Mission, in: European Planetary Science Congress 2020.

Marchi, S., Ermakov, A.I., Raymond, C.A., Fu, R.R., O'Brien, D.P., Bland, M.T., Ammannito, E., Sanctis, M.C. De, Bowling, T., Schenk, P., Scully, J.E.C., Buczkowski, D.L., Williams, D.A., Hiesinger, H., Russell, C.T., 2016. The Missing Large Impact Craters on Ceres. Nat. Commun. 12257. doi:10.1038/ncomms12257

Marchi, S., Mottola, S., Cremonese, G., Massironi, M., Martellato, E., 2009. A new chronology for the Moon and Mercury. Astron. J. 137, 4936–4948. doi:10.1088/0004-6256/137/6/4936

Martin, E.S., Patthoff, D.A., 2018. Mysterious Linear Features Across Saturn's Moon Dione. Geophys. Res. Lett. 978–986. doi:10.1029/2018GL079819

Melosh, H.J., 1989. Impact Cratering a Geologic Process. Oxford University Press.

Minton, D.A., Richardson, J.E., Thomas, P., Kirchoff, M.R., Schwamb, M.E., 2012. Combining Saturnian Craters and Kuiper Belt Observations to build an Outer Solar System Impactor Size-Frequency Distribution. Lunar Planet. Sci. Conf. 2669.

Mitchell, K.L., Prockter, L.M., Frazier, W.E., Smythe, W.D., Sutin, B.M., Bearden, D.A., Team, T., 2019. Implementation of Trident: A Discovery-Class Mission to Triton 19.

Moore, J.M., Schenk, P.M., Bruesch, L.S., Asphaug, E., McKinnon, W.B., 2004. Large impact features on middle-sized icy satellites. Icarus 171, 421–443. doi:10.1016/j.icarus.2004.05.009

National Research Council (U.S.). Space Studies Board., 2011. Vision and voyages for planetary science in the decade 2013-2022. National Academies Press.

Nava, R.A., 2010. Crater Helper Tools - Manual.

Nesvorný, D., Vokrouhlick, D., Bottke, W.F., Noll, K., Levison, H.F., 2011. Observed binary fraction sets limits on the extent of collisional grinding in the Kuiper Belt. Astron. J. 141. doi:10.1088/0004-6256/141/5/159

Neukum, G., Ivanov, B.A., Hartmann, W.K., 2001. Cratering records in the inner solar

system in relation to the lunar reference system. Space Sci. Rev. 96, 55–86. doi:10.1023/A:1011989004263

Neukum, G., Wagner, R., Denk, T., Porco, C.C., Team, and the C.I., 2005. The cratering record of the saturnian satellites Phoebe, Tethys, Dione and Iapetus in comparison: First results from analysis of the Cassini ISS imaging data. Lunar Planet. Sci. Conf.

Neveu, M., Rhoden, A.R., 2019. Evolution of Saturn ' s mid-sized moons. Nat. Astron. 3, 543–552. doi:10.1038/s41550-019-0726-y

Öhman, T., 2009. The structural control of polygonal impact craters. University of Oulu, Finland.

Öhman, T., Aittola, M., Korteniemi, J., Kostama, V.P., Raitala, J., 2010. Polygonal impact craters in the solar system: Observations and implications. Spec. Pap. Geol. Soc. Am. 465, 51–65. doi:10.1130/2010.2465(04)

Öhman, T., Aittola, M., Kostama, V.P., Hyvärinen, M., Raitala, J., 2006. Polygonal impact craters in the Argyre region, Mars: Evidence for influence of target structure on the final crater morphology. Meteorit. Planet. Sci. 41, 1163–1173. doi:10.1111/j.1945-5100.2006.tb00513.x

Öhman, T., Aittola, M., Kostama, V.P., Raitala, J., Korteniemi, J., 2008. Polygonal impact craters in Argyre region, Mars: Implications for geology and cratering mechanics. Meteorit. Planet. Sci. 43, 1605–1628. doi:10.1111/j.1945-5100.2008.tb00632.x

Ostrach, L.R., 2013. Impact-Related Processes on Mercury and the Moon. Arizona State University.

Peale, S.J., 1999. Origin and Evolution of the Natural Satellites. Annu. Rev. Astron. Astrophys. 37, 533–602.

Peale, S.J., Canup, R.M., 2015. The Origin of the Natural Satellites, Treatise on Geophysics: Second Edition. Elsevier B.V. doi:10.1016/B978-0-444-53802-4.00177-9

Phillips, C.B., Hammond, N.P., Robuchon, G., Nimmo, F., Beyer, R., Roberts, J., 2012. Stereo Imaging, Crater Relaxation, and Thermal Histories of Rhea and Dione. 43rd Lunar Planet. Sci. Conf. 2571. doi:10.1029/2005JE002607.

Plescia, J.B., Boyce, J.M., 1985. Impact cratering history of the Saturnian satellites. J. Geophys. Res. 90, 2029. doi:10.1029/jb090ib02p02029

Plescia, J.B., Boyce, J.M., 1982. Crater densities and geological histories of Rhea, Dione,

Mimas and Tethys. Nature 295, 285–290. doi:10.1038/295285a0

Porco, C.C., West, R.A., Squyres, S., Ingersoll, A.P., Johnson, T. V, Neukum, G., Veverka, J., Dones, L., Brahic, A., Burns, J.A., Haemmerle, V., Knowles, B., Dawson, D., Roatsch, T., Beurle, K., Owen, W., 2004. CASSINI IMAGING SCIENCE : INSTRUMENT CHARACTERISTICS AND ANTICIPATED SCIENTIFIC INVESTIGATIONS AT SATURN. Space Sci. Rev. 363–497.

Prockter, L.M., Mitchell, K.L., Howett, C.J.A., Smythe, W.D., Sutin, B.M., Bearden, D.A., Frazier, W.E., Team., T., 2019. Exploring Triton with Trident: A Discovery-Class Mission. Lunar Planet. Sci. Conf. 3188.

Richardson, J.E., 2009. Cratering saturation and equilibrium: A new model looks at an old problem. Icarus 204, 697–715. doi:10.1016/j.icarus.2009.07.029

Rivera-Valentín, E.G., Oquendo, A.J.L., Kirchoff, M.R., Ore, C.M.D., Scipioni, F., 2020. Constraints on the Recent Cratering Rate in the Saturn System from Water Ice Crystallinity Derived Crater Formation Ages on Dione. Lunar Planet. Sci. Conf. 2839.

Roatsch, T., Wählisch, M., Hoffmeister, A., Kersten, E., Matz, K.D., Scholten, F., Wagner, R., Denk, T., Neukum, G., Helfenstein, P., Porco, C., 2009. High-resolution Atlases of Mimas, Tethys, and Iapetus derived from Cassini-ISS images. Planet. Space Sci. 57, 83–92. doi:10.1016/j.pss.2008.10.014

Roatsch, T., Wählisch, M., Hoffmeister, A., Matz, K.D., Scholten, F., Kersten, E., Wagner, R., Denk, T., Neukum, G., Porco, C., 2008. High-resolution Dione atlas derived from Cassini-ISS images. Planet. Space Sci. 56, 1499–1505. doi:10.1016/j.pss.2008.06.008

Robbins, S.J., Antonenko, I., Kirchoff, M.R., Chapman, C.R., Fassett, C.I., Herrick, R.R., Singer, K., Zanetti, M., Lehan, C., Huang, D., Gay, P.L., 2014. The variability of crater identification among expert and community crater analysts. Icarus 234, 109–131. doi:10.1016/j.icarus.2014.02.022

Robbins, S.J., Riggs, J.D., Weaver, B.P., Bierhaus, E.B., Chapman, C.R., Kirchoff, M.R., Singer, K.N., Gaddis, L.R., 2018. Revised recommended methods for analyzing crater size-frequency distributions. Meteorit. Planet. Sci. 53, 891–931. doi:10.1111/maps.12990

Russell, C.T., Raymond, C.A., Ammannito, E., Buczkowski, D.L., De Sanctis, M.C., Hiesinger, H., Jaumann, R., Konopliv, A.S., McSween, H.Y., Nathues, A., Park, R.S., Pieters, C.M., Prettyman, T.H., McCord, T.B., McFadden, L.A., Mottola, S., Zuber, M.T., Joy, S.P., Polanskey, C., Rayman, M.D., Castillo-Rogez, J.C., Chi, P.J., Combe, J.P., Ermakov, A., Fu, R.R., Hoffmann, M., Jia, Y.D., King, S.D., Lawrence, D.J., Li, J.Y., Marchi, S., Preusker, F., Roatsch, T., Ruesch, O., Schenk, P., Villarreal, M.N., Yamashita, N., 2016. Dawn arrives at ceres: Exploration of a

small, volatile-rich world. Science (80-.). 353, 1008–1010. doi:10.1126/science.aaf4219

Salmon, J., Canup, R.M., 2017. Accretion of Saturn's Inner Mid-sized Moons from a Massive Primordial Ice Ring. Astrophys. J. 836, 109. doi:10.3847/1538-4357/836/1/109

Sasaki, T., Stewart, G.R., Ida, S., 2010. Origin of the different architectures of the jovian and saturnian satellite systems. Astrophys. J. 714, 1052–1064. doi:10.1088/0004-637X/714/2/1052

Schenk, P., White, O.L., Byrne, P.K, Moore, J.M., 2018.Saturn's Other Icy Moons: Geologically Complex Worlds in Their Own Right, in: Schenk, P.M. et al., (Ed.), Enceladus and the Icy Moons of Saturn. Univ. of Arizona Press, Tucson AZ, Tucson, pp. 237–265. doi:10.2458/azu_uapress_9780816537075-ch012

Schenk, P., Hamilton, D.P., Johnson, R.E., McKinnon, W.B., Paranicas, C., Schmidt, J., Showalter, M.R., 2011. Plasma, plumes and rings: Saturn system dynamics as recorded in global color patterns on its midsize icy satellites. Icarus 211, 740–757. doi:10.1016/j.icarus.2010.08.016

Schenk, P.M., Moore, J.M., 2009. Eruptive Volcanism on Saturn's Icy Moon Dione. 40th Lunar Planet. Sci. Conf. Abstract 2, 1–2.

Schenk, P.M., Zahnle, K., 2007. On the negligible surface age of Triton. Icarus 192, 135–149. doi:10.1016/j.icarus.2007.07.004

Schlichting, H.E., Fuentes, C.I., Trilling, D.E., 2013. Initial planetesimal sizes and the size distribution of small Kuiper Belt objects. Astron. J. 146. doi:10.1088/0004-6256/146/2/36

Schmedemann, N., Wagner, R.J., Roatsch, T., Hiesinger, H., 2021. Crater Distributions of the Galilean Satellites. Lunar Planet. Sci. Conf. 2250.

Schultz, P., Gault, D.E., 1990. Decapitated impactors in the laboratory and on the planets. Lunar Planet. Sci. Conf.

Shoemaker, E.M., 1963. Impact Mechanics at Meteor Crater, Arizona, in: Middelhurst, B.M., Kuiper, G.. (Eds.), The Moon, Meteorites, and Comets. University of Chicago Press, Chicago, pp. 301–336.

Shoemaker, E.M., Wolfe, R.F., 1981. Evolution of the Saturnian Satellites: The role of impact, in: 12th Lunar and Planetary Science Conference.

Singer, K.N., Mckinnon, W.B., Gladman, B., Greenstreet, S., Bierhaus, E.B., Stern, S.A.,

Parker, A.H., Robbins, S.J., Schenk, P.M., Grundy, W.M., Bray, V.J., Beyer, R.A., Binzel, R.P., Weaver, H.A., Young, L.A., Spencer, J.R., Kavelaars, J.J., Moore, J.M., Zangari, A.M., Olkin, C.B., Lauer, T.R., Lisse, C.M., Ennico, K., Geology, N.H., Science, I., Horizons, N., Composition, S., Ralph, N.H., 2019. Impact craters on Pluto and Charon indicate a deficit of small Kuiper belt objects. Science (80-.). 959, 955–959.

Smith, B.A., Soderblom, L., Batson, R., Bridges, P., Masursky, H., Shoemaker, E., Beebe, R., Boyce, J., Briggs, G., Bunker, A., Collins, S.A., Hansen, C.J., Johnson, T. V, Jim, L., Terrile, R.J., Cook, A.F., Cuzzi, J., Pollack, J.B., Edward, G., Ingersoll, A.P., Davies, M.E., Hunt, G.E., Morrison, D., Sagan, C., 1982. A New Look at the Saturn System: The Voyager 2 Images. Science (80-.). 215, 504–537.

Smith, B.A., Soderblom, L., Beebe, R., Boyce, J., Bunker, A., Collins, S.A., Hansen, C.J., Johnson, T. V, Jim, L., Terrile, R.J., Carr, M., Cook, A.F., Cuzzi, J., Pollack, J.B., Danielson, E., Ingersoll, A., Davies, M.E., Hunt, G.E., Masursky, H., Shoemaker, E., Morrison, D., Owen, T., Sagan, C., Veverka, J., 1981. Encounter with Saturn : Voyager 1 Imaging Science Results. Science (80-.). 212, 163–91.

Spencer, J.R., Pearl, J.C., Segura, M., Flasar, F.M., Mamoutkine, A., Romani, P., Buratti, B.J., Hendrix, A.R., Spilker, L.J., Lopes, R.M.C., 2006. Cassini Encounters Enceladus: Background and the Discovery of a South Polar Hot Spot. Science (80-.). 311, 1401–1405.

Stephan, K., Jaumann, R., Wagner, R., Clark, R.N., Cruikshank, D.P., Hibbitts, C.A., Roatsch, T., Hoffmann, H., Brown, R.H., Filiacchione, G., Buratti, B.J., Hansen, G.B., McCord, T.B., Nicholson, P.D., Baines, K.H., 2010. Dione's spectral and geological properties. Icarus 206, 631–652. doi:10.1016/j.icarus.2009.07.036

Stephan, K., Wagner, R., Jaumann, R., Clark, R.N., Cruikshank, D.P., Brown, R.H., Giese, B., Roatsch, T., Filacchione, G., Matson, D., Ore, C.D., Capaccioni, F., Baines, K.H., Rodriguez, S., Krupp, N., Buratti, B.J., Nicholson, P.D., 2016. Cassini's geological and compositional view of Tethys. Icarus 274, 1–22. doi:10.1016/j.icarus.2016.03.002

Stoffler, D., Ryder, G., 2001. Stratigraphy and Isotope Ages of Lunar Geologic Units. Space Sci. Rev. 96, 9–54.

Strom, R.G., Malhotra, R., Ito, T., Yoshida, F., Kring, D.A., 2005. The Origin of Planetary Impactors in the Inner Solar System. Science (80-.). 309, 1847–1851. doi:10.1126/science.1113544

Strom, R.G., Marchi, S., Malhotra, R., 2018. Ceres and the terrestrial planets impact cratering record. Icarus 302, 104–108. doi:10.1016/j.icarus.2017.11.013

Thomas, P.C., 2010. Sizes, shapes, and derived properties of the saturnian satellites after the Cassini nominal mission. Icarus 208, 395–401. doi:10.1016/j.icarus.2010.01.025

Tiscareno, M.S., Malhotra, R., 2003. The Dynamics of Known Centaurs. Astron. J. 3122–3131.

Volk, K., Malhotra, R., 2008. The scattered disk as the source of the jupiter family comets 714–725.

White, O.L., Schenk, P.M., Bellagamba, A.W., Grimm, A.M., Dombard, A.J., Bray, V.J., 2017. Impact crater relaxation on Dione and Tethys and relation to past heat flow. Icarus 288, 37–52. doi:10.1016/j.icarus.2017.01.025

Zahnle, K., Schenk, P., Levison, H., Dones, L., 2003. Cratering rates in the outer solar system. Icarus 163, 263–289. doi:10.1016/S0019-1035(03)00048-4

Zahnle, K., Schenk, P., Sobieszczyk, S., Dones, L., Levison, H.F., 2001. Differential cratering of synchronously rotating satellites by ecliptic comets. Icarus 153, 111–129. doi:10.1006/icar.2001.6668

Zahnle, K.J., Levison, H., Dones, L., 1998. Cratering Rates on the Galilean Satellites. Lunar Planet. Sci. Conf. 1902.

Zannoni, M., Hemingway, D., Gomez Casajus, L., Tortora, P., 2020. The gravity field and interior structure of Dione. Icarus 345, 113713. doi:10.1016/j.icarus.2020.113713

APPENDIX A

IMAGE PROCESSING FOR CASSINI ISS DATA

Prepared by Sierra Ferguson
ASU School of Earth and Space Exploration

First make sure that all of the raw data that you want to use is downloaded to the computer and is in the same directory as ISIS3 so that the software can reach it. Need to have the .LBL file and .IMG files from the PDS. For the outer planets you can use the Outer Planets Unified Search (https://opus.pds-rings.seti.org/) through the PDS Ring-Moon Systems node, or go straight to the PDS imaging node if you know the file names (Say if you used Pilot to find the desired images). PILOT (https://pilot.wr.usgs.gov) is another site that allows the download of both the LBL and IMG files for Cassini data. If you download the bash script, chmod+x FILENAME on the command line will enable the file to be executable and download the data into the current working directory.

Also useful: list of ISIS3 commands and their various inputs needed to process the data https://isis.astrogeology.usgs.gov/Application/index.html

1. Create a list of all files that will be run through the calibration routines.
   If on mac, make sure that the .LBL files are actually .LBL instead of having a .txt extension
   List just needs to have the name, no .LBL extension needed

   Command Line code: ls *.LBL (Will show the files with this extension) →
   ls *.LBL | sed s/.LBL//>root.lis
   (will output the files to a list that can be read by the calibration files)

2. Converts .LBL to .cub

   ciss2isis –batchlist=root.lis from=\$1.LBL to=\$1.cub

3. Initiate spacecraft pointing information via SPICE kernels

   spiceinit –batchlist=root.lis from=\$1.cub

4. Calibrates the PDS data. Corrects the bitweight, subtracts the bias, subtracts the dark, linearizes, correct the flat field, convert DN to flux, divide by the correction factor (deals with polarization woo)

   cisscal –batchlist=root.lis from=\$1.cub to=\$1_cal.cub

5. Remove all of the lines that are on the Cassini images

   lowpass –batchlist=root.lis from=\$1_cal.cub to=\$1_fill.cub samples=3 lines=3 filter=outside replacement=center

I use 3 here and that has worked for my purposes, other values may work well too.

6. More removal of lines, trims one pixel and assigns the pixel value to null

   trim –batchlist=root.lis from=\$1_fill.cub to=\$1_tr.cub top=1 bottom=1 left=1 right=1

7. Bring in the Camera Stats: This adds in information about resolutions, emission angle, phase angle, and incidence angle. Can be viewed in Qmos and can attach to the label if desired.

   camstats –batchlist=rootmos.lis from=\$1_tr.cub attach=true format=flat to=camstats.csv linc=10 sinc=10

8. Define a map template for the images to be projected into

   maptemplate map=__.map projection=_____ clat=__ clon=__ targopt=user targetname=___ resopt=mpp resolution=___

   map: name your map template
   projection: choose the map projection, ie: SIMPLECYLINDRICAL, POLARSTEREOGRAPHIC, SINUSOIDAL, MERCATOR, ORTHOGRAPHIC, EQUIRECTANGULAR, ROBINSON
   clat: Center latitude to use for that map. Not needed for simple cylindrical
   clon: Center longitude to use for the map
   targetname: Pick a planet any planet/moon! (i.e., TETHYS, ENCELADUS, TITAN, DIONE)
   resolution: Choose a resolution that you are forcing the map to be in

9. **Map project here if not going further and mosaicking**

   cam2map –batchlist=root.lis from=\$1_tr.cub to=\$1_mp.cub map=yourmaptemplatehere pixres=map

10. Create a new list with the now map projected images to be used later

    ls *mp.cub >mp.lis

THE ABOVE COMMANDS SHOULDTO BE APPLIED TO ALL CASSINI DATA BEFORE BRINGING INTO ARCMAP. Minimum to bring into arc is ciss2isis, spiceinit, and cisscal. Map projecting is super useful and needed to take accurate measurements from the images

The following steps are for creating mosaics and ensuring that there are no seams or weird overlaps on the mosaics. So the mapping looks great and that the data collected will be reliable. If a non-controlled mosaic is needed can skip to the last page and follow steps from there starting at the Qmos step.

1. Create a new list to apply the mosaic commands to:

   ls .*_tr.cub → ls *._tr.cub > rootmos.lis

2. Bring in the camera statistics for the images (If not already done above). Brings in lat, long, sample res, line res, resolution, aspect ratio, phase angle, emission angle, incidence angle, local solar time, north azimuth.

   camstats –batchlist=rootmos.lis from=\$1_tr.cub attach=true format=flat to=camstats.csv linc=10 sinc=10

3. Load the footprint information for each image that can later be displayed in qmos. Makes a lat/long grid that enables the display of the image footprint

   footprintinit –batchlist=rootmos.lis from=\$1_tr.cub maxemission=85 maxincidence=85

   maxemission/incidence**:** Choose a value so that you don't get like pure black pixels if the value is 90.

4. Find where each image that you want to mosaic overlap

   findimageoverlaps- Opens the GUI where you can input the rootmos.lis and create a new list where you can call it like imageoverlap.lis

5. Calculate statistics for the image overlaps

   overlapstats –opens the GUI for the input of files
   fromlist: list of input cubes rootmos.lis
   overlaplist: list created by findimageoverlap
   to: desired file output

6. Initiate a control net for the mosaics

   autoseed: Opens a GUI where a definition file **must** be inputted.

Def file must end with .def following this format (via the ISIS3 documentation). Copy this into a new def file and modify to create the best grid for your mosaic. Def file may need to be modified based on the sizes of the image overlaps.

“Group = PolygonSeederAlgorithm

  # Seeds the polygon with Control Points by creating a grid, the centermost grid
  # is placed in the center of the polygon. Then, one Control Point is placed in the
  # center of each grid where there is overlap at that center of that grid square.
  # The following XSpacing/YSpacing parameters denote the dimensions of the grid.
  Name   = Grid

  # The minimum thickness required to seed the polygon with Control Points. A
  # thickness of 1.0 means that the polygon is a square. A thickness of 0.5
  # means that the polygon is a 2:1 rectangle. A thickness of 0.25 means that
  # the polygon is a 4:1 rectangle, and so forth.
  # Any polygon with a thickness less than MinimumThickness will not be seeded.
  MinimumThickness = 0.3

  # The minimum area (in square meters) required to seed the polygon with
  # Control Points. Any polygon with an area less than MinimumArea will not be
  # seeded.
  MinimumArea   = 10

  # The spacing in meters between Control Points in the X direction. One
  # Control Point will be placed every XSpacing meters in the X direction.
  # This combined with the YSpacing, will create a grid of Control Points
  # across the polygon.
  XSpacing   = 1500

  # The spacing in meters between Control Points in the Y direction. One
  # Control Point will be placed every YSpacing meters in the Y direction.
  # This combined with the XSpacing, will create a grid of Control Points
  # across the polygon.
  YSpacing   = 1500

End_Group”

7. Setting up the control net yay!
   qnet- Will open up the GUI where you can load in the control net that was created in the previous step. Can now view all of the images that are included in the mosaic list and match each point to an image. Choose a feature on the left hand image and then ensure that the right hand image aligns in the center of the crosshairs. When that referencing has been done for that point across all of the images select save point. This should be done for as many points that seem necessary to make the control net accurate. When all is said and done, save the new control net to be used on that mosaic.

Check the Control Net to make sure that there aren't any missing gaps. Jigsaw will tell you if it fails, but this command will tell you exactly what happened with the control net.

Cnetcheck, GUI opens up to view cnet errors.

8. Applying the control net to the images!

   Jigsaw: Open the GUI again and input the list of files with the _tr extension, and use the new control net that was just created in qnet.

9. Mosrange: GUI can better create a map file that works with the mosaic

10. Cam2map: Projects data into a map projection that can be read in arc

11. Load images back into qmos, sort them based on resolution and then output a list (using qmos) called mosorder.lis to tell the program to put the highest resolution images on top
    - Check to make sure that all images that you want to mosaic were taken in the same filter, otherwise automos will not mosaic them together and will crash.

12. Now create the mosaic!

    automos fromlist=mosorder.lis mosaic=yourmosaicnamehere.cub minlat=__ maxlat=__ minlon=__ maxlon=___ grange=user